

THE USE OF *IN VIVO* X-RAY FLUORESCENCE  
MEASUREMENTS IN THE ANALYSIS OF CADMIUM  
TOXICOLOGY

THE USE OF *IN VIVO* X-RAY FLUORESCENCE  
MEASUREMENTS IN THE ANALYSIS OF CADMIUM  
TOXICOLOGY

by

Sean Carew, B.Sc.

A thesis submitted to the School of Graduate  
Studies in partial fulfilment of the requirements  
for the degree:

Master of Science

McMaster University

2001

©Copyright by Sean Carew, August, 2001

Master of Science (2001)  
(Physics and Astronomy)

McMaster University  
Hamilton, Ontario

TITLE: The Use Of *In Vivo* X-Ray Fluorescence Measurements In The  
Analysis Of Cadmium Toxicology

AUTHOR: Sean Carew, B.Sc.

SUPERVISOR: Dr. David R. Chettle

NUMBER OF PAGES: xiv, 133

## Abstract

Cadmium (Cd) is a highly toxic metallic element to the human body such that prolonged occupational or environmental exposure produces renal, hepatic, pneumonic, and neurological disorders. Thus, as a consequence it is important to have a way of monitoring cadmium exposure as it has the potential to become an occupational health hazard. The primary uses of this element are in the mining and smelting industry in the manufacture of cadmium alloys and the manufacture of alkaline accumulators.

Since the discovery of X-rays in 1895 by Wilhelm Conrad Roentgen, the science of X-ray analysis has become a cardinal tool in all domains of chemical identification and classification. X-ray fluorescence (XRF) has been shown to be an effectual technique for measuring trace quantities of heavy metals such as lead in various tissues within the body. This thesis study elucidates a means of measuring Cadmium in bone. The study assesses the feasibility and practicality of the polarised XRF and source excited techniques.

In the polarised cadmium concentration measurements, a gain in sensitivity due to improved background characteristics was perceived by increasing the x-ray tube operating voltage of the system. It was found that an operating voltage of 175 kV, and a copper filter resulted in a significant gain in sensitivity for which a minimum detection limit (MDL) of  $3.5 \pm 1.4$  ppm was determined with 3 mm of tissue equivalent overlay. Using the source-based technique, a MDL of  $3.5 \pm 0.2$  ppm was estimated for the corresponding tissue equivalent overlay.

## **Acknowledgements**

I would like to thank my supervisor Dr. David Chettle for his support, his advice, and encouragement throughout the past two years. Thank you for everything! I would also like to thank my supervisory committee members, Dr. F. McNeill, Dr. C. Webber and Dr. W. Prestwich.

A special thanks you goes to Dr. H. Roels for his invaluable help and suggestions throughout the initial stages of my research. I would also like to thank Dr. I. Stronach and S. Bateman for their help in the preliminary stages of this research. I am also very grateful to Dr. M. Arnold for her expertise in this field of research.

I would also like to thank the accelerator crew, especially Mr. J. Cave for his speedy assistance in the manufacturing of the wax overlays, copper filters and source collimators. I am very grateful to J. Falladown for his assistance in the preparation of the XRF measurements. I would also like to thank J. Stark and S. McMaster for their jovial nature and encouragement.

I would like to also thank my fellow colleagues D. Static, L. Nie, R. Studinski, A. Aslam and R. Khan for their encouragement and appreciation.

I would like to also thank my girlfriend Deborah Bayne, my parents Hether and Egbert Carew, my sister Sharon Carew, my niece Sherilynn for their never-ending moral support. I am also grateful for the support and inspiration of my family Uncle Ken, Uncle Sylvan, Uncle Winston and Auntie Cheryl and Cousin Freddie.

## Table of Contents

ABSTRACT	iv
ACKNOWLEDGEMENTS	v
TABLE OF CONTENTS	vi
LIST OF FIGURES	ix
LIST OF TABLES	xiii
<b>CHAPTER 1</b>	
<b>INTRODUCTION</b>	
1.1. ON THE SUBJECT OF CADMIUM	1
1.2. CADMIUM HEALTH CONCERNS	3
1.2.1. Cadmium Toxicokinetics	3
1.2.2. Cadmium Toxicodynamics	3
1.3. OCCUPATIONAL MONITORING PROCEDURES	8
1.4. MEASURING TECHNIQUES	9
1.4.1. Invasive Techniques	9
1.4.2. Non-Invasive Elemental Analysis	9
1.5. RESEARCH INVESTIGATIONS IN XRF	11
<b>CHAPTER 2</b>	
<b>PRINCIPLES OF X-RAY FLUORESCENCE</b>	
2.1. X-RAY FLUORESCENCE	14
2.2. PHOTONS INTERACTIONS WITH MATTER	14
2.3. SOURCES OF PHOTONS	20
2.4. SOURCE-EXCITED X-RAY FLUORESCENCE	22
2.5. POLARISED X-RAY FLUORESCENCE	23
2.6. PHOTON DETECTION SYSTEMS	25

**CHAPTER 3****EXPERIMENTAL METHODS**

3.1. SYSTEM DESCRIPTION OF THE CADMIUM MEASUREMENT SYSTEM	27
3.1.1. Detection Systems	29
3.2. DESIGN PARAMETERS	32
3.2.1. Effects of Geometry	32
3.2.2. Collimation	33
3.2.3. Tube Current and Voltage	35
3.2.4. Polariser Material	35
3.2.5. Filtration	36
3.3. PHANTOMS	38
3.3.1. Design and Preparation	38
3.3.2. Phantom Measurements	41

**CHAPTER 4****ANALYTICAL INTERPRETATION OF THE CADMIUM MEASUREMENT SYSTEM**

4.1. PHANTOM CONCERNS AND RELIABILITY	42
4.2. OPTIMISATION OF THE SYSTEM PARAMETERS	47
4.3. OPTIMISATION OF THE POLARISATION PARAMETERS	54
4.4. LEVENBERG-MARQUARDT ANALYSIS	58
4.5. SPECTRAL ANALYSIS	62

**CHAPTER 5****CALIBRATION CURVES AND MINIMUM DETECTABLE LIMITS**

5.1	INTRODUCTION	
5.1.1.	Determination of Optimal Fitting Parameters	76
5.1.2.	Determination of the MDL for the Cadmium Doped Plaster of Paris phantom	79
5.2	SOURCE BASED ANALYSIS	83
5.2.1.	Determination of the MDL for the Cadmium doped Water phantom	83
5.2.2.	Determination of the MDL for the Cadmium Doped Plaster of Paris Phantom in Wax.	85
5.3	COLLIMATOR CONSIDERATIONS	88
5.4	POLARISED XRF ANALYSIS	90
5.4.1.	MDL Determination of Optimal Filter Thickness	90
5.4.2.	MDL Determination using a 1.2 mm Filter	93
5.5	DOSIMETRY	97
5.6	CLINICAL IMPLICATIONS	102

**CHAPTER 6****CONCLUSIONS AND FUTURE WORK**

6.1	EVIDENCE FOR CADMIUM IN VIVO XRF MEASUREMENT	103
6.2	CALIBRATION OF PHOTON SOURCES	105
6.3	NEW DETECTION SYSTEMS	109
6.4	COMPUTER MODELLING TECHNIQUES	113
6.5	FINAL REMARKS	115

## LIST OF FIGURES

- Figure 2.1** Spectrum detected during a 2000s (live time) measurement of the 170 ppm cadmium-doped plaster of Paris phantom using the  $^{109}\text{Cd}$  source in a backscatter geometry sample to detector distance, 2 cm. Note the coherent peak at 88.035 keV, and the dominating Compton peak, very large and tailing off to the left. Also the Cadmium peaks can be seen clearly as they appear in the valley of the background.
- Figure 2.2** Unpolarised photons from a X-ray tube are polarised before interacting with the sample (O'Meara, 1999).
- Figure 3.1** Germanium detection system
- Figure 3.2** Typical spectra acquired by the use of HPGe detectors using the Canberra S10C software.
- Figure 3.3** Experimental set up of the  $^{109}\text{Cd}$  system for the in vivo measurement of cadmium. Geometry used for simulating the  $180^\circ$  backscatter.
- Figure 3.4** Collimator dimensions used for the source-based collimation, the length of the bore was varied to acquire the variable collimator length.
- Figure 3.5** Experimental set up of the polarised XRF system for the in vivo measurement of cadmium.
- Figure 4.1** The spectra accumulated when the 144 ppm Cd phantom was rotated in  $90^\circ$  intervals in order to test the phantom homogeneity.
- Figure 4.2** Sensitivity as a function of phantom angular position. It is clear that there is not much effect overall, therefore confirming that the cadmium-doped phantom is fairly homogeneous.
- Figure 4.3** Summed spectrum from a Ge detector for a 170 ppm Cd of bone phantom, counted for 2000s live time. The full energy spectrum of the incident photons as detected by the Ge detector is shown in the insertion.
- Figure 4.4** Spectrum of a blank tube phantom (0 ppm) placed at a sample to detector distance 40 mm away. Polarised system was used with the Princeton double-headed gamma detector.

- Figure 4.5** Spectrum of the 40 ppm distilled water phantom placed at a sample to detector distance 20 mm away. Polarised system was used with the Ge Canberra, model GL2020R.
- Figure 4.6** Illustrates the FWHM of the Ge GL2020R detector system when the cadmium series line was analysed using polarised XRF.
- Figure 4.7** Demonstrates the spatial distribution of the observed alpha peak counts with increasing distance between the source and the sample.
- Figure 4.8** Optimisation of X-ray tube operating voltage. The voltage optimisation has been performed on the basis of dead time, FWHM and gross counts for 1.2 mA current.
- Figure 4.9** Detector dead time response for 4 different samples to increasing voltage.
- Figure 4.10** Relationship between tube current and the total number of alpha and beta counts when an X-ray machine was operated at 175 keV.
- Figure 4.11** Initial Marquardt fit to spectral data observed for 50 mg cadmium phantom. The selected region of interest is taken as the region between 375 to 475 channels. This pulse height distribution was obtained by running a Marquardt modelling program created to account for the necessary observed peak.
- Figure 4.12** Shows an alpha peak calibration curve. This is a plot of tail amplitude versus cadmium concentration when an exponential function was used to model the background.
- Figure 4.13** Marquardt 11-parameter fit to spectral data (30 ppm water phantom). There is the occurrence of alpha and beta multiple peaks. However, these resulting multi-peaks in the spectrum could not be resolved visually, as the X-ray energy difference of the peaks *e.g.*  $K_{\alpha 1}$  and  $K_{\alpha 2}$  peaks, were less than the FWHM of the system.
- Figure 4.14** Peak width variation for the plaster of Paris with no tissue overlay and with 5 mm artificial tissue.
- Figure 4.15** Thickness variation. The results showed little dependence on overlaying phantom tissue.
- Figure 4.16** 10-parameter Marquardt fit to spectral data (34 ppm plaster of Paris phantom) using a 1.6 mm external copper filter.
- Figure 4.17** Indium ratio for the plaster of Paris line in 5 mm wax.

- Figure 4.18** Indium ratio for different wax thickness.
- Figure 4.19** 9-parameter Marquardt fit to spectral data (68 ppm plaster of Paris) using the 1.2 mm filter.
- Figure 4.20** Indium beta to alpha ratio for the more concentrated phantoms
- Figure 5.1** Detection level analysis for the cadmium plaster of Paris alpha peak using the exponential background fitting.
- Figure 5.2** Variation in detectability for various target medium using the source-based collimator 8.75 mm for the water, plaster of Paris, plaster of Paris with wax 0 mm phantoms
- Figure 5.3** Variation of the fitted peak amplitudes for the cadmium peaks for the cylindrical set of phantoms placed 2 cm away from source, using the 8.75 mm collimator.
- Figure 5.4** Variation in detectability for the various water phantom concentrations using the 9-parameter fit with the 8.75 mm collimator. In general, the MDL increases, as concentration increases.
- Figure 5.5** MDL versus wax thickness variation for the 8.75 mm collimator.
- Figure 5.6** Alpha and beta calibration curve using 10.75 mm collimator.
- Figure 5.7** MDL versus collimator variation for the 2 mm, 5 mm and 8 mm wax overlay.
- Figure 5.8** Dead time versus filter thickness for the polarised XRF measurement.
- Figure 5.9** MDL filter thickness variation for with a current of 12.5 mA.
- Figure 5.10** Dose normalised MDL versus filter thickness for the polarised XRF measurement.
- Figure 5.11** Cadmium alpha calibration curve for the 1.2 mm filter, tubular set of plaster of Paris phantoms measured using a HPGe detector. Irradiation in a  $90^{\circ}$  geometry, 20 mm sample to detector distance.
- Figure 5.12** Cadmium beta calibration curve for 1.2 mm filter, the tubular set of plaster of Paris phantoms measured using a HPGe detector. Irradiation in a  $90^{\circ}$  geometry, 20 mm sample to detector distance.
- Figure 5.13** MDL wax thickness for the polarised system using a 1.2 mm external copper filter.

- Figure 6.1** Spectrum detected during a 2000s (live time) measurement of the 170 ppm cadmium-doped plaster of Paris phantom (no wax overlay) using the  $^{109}\text{Cd}$  source in a backscatter geometry sample to detector distance, 2 cm. Note the coherent peak at 88.035 keV.
- Figure 6.2** Spectrum detected during a 2000s (live time) measurement of the 170 ppm cadmium-doped plaster of Paris phantom (no wax overlay) using the  $^{241}\text{Am}$  source in a backscatter geometry sample to detector distance, 2 cm. Note the coherent peak at 59.5 keV.
- Figure 6.3** Variation of the fitted peak amplitudes for the americium peaks for the cylindrical set of phantoms placed 2 cm away from source.

## LIST OF TABLES

- Table 2.1** Cadmium K-shell X-ray characteristics (a)
- Table 2.2** A comparison of the characteristics of the possible isotopic sources for cadmium X-ray fluorescence measurements. (b)
- Table 2.3** Comparison of Coherent Cross-sections for 88 keV photons (Mattsson and Scott, 1990)
- Table 4.1** Shows the observed peak energy with the corresponding channel numbers for the experimental gain used. K X-ray energies taken from Lederer & Shirley, 1978.
- Table 4.2** Displays the results as determined for different concentration phantoms by Marquardt analysis program.
- Table 4.3** Determination of Precision for the different fitting programs
- Table 5.1** Determination of alpha and beta MDLs for the linear and exponential background fitting models, using the plaster of Paris phantoms. Results are given in ppm.
- Table 5.2** Summary of the MDL analysis for the water, the plaster of Paris and the plaster of Paris with wax 0 mm phantom for the 7, 9, 10 and 11 parameter fits wherever possible using the source based measuring technique.
- Table 5.3** Summary of regression analysis of 2 calibration lines for the cadmium bone system.
- Table 5.4** Summary of the determined MDL using the 9-parameter fitting model for the plaster of Paris phantoms with increasing wax tissue overlay.
- Table 5.5a** Collimator variation for wax thickness 2 mm
- Table 5.5b** Collimator variation for wax thickness 5 mm
- Table 5.5c** Collimator variation for wax thickness 8 mm
- Table 5.6** MDL versus filter thickness. The analysis was obtained by using the bare plaster of Paris phantom with no wax overlay

- Table 5.7** Summarising the MDL Variation with wax thickness using a 1.2 mm external copper filter
- Table 5.8** Normalised (MDLs) and doses delivered to the cylindrical set of phantoms during a 2000 seconds cadmium measurement. Source based distance (20mm)
- Table 5.9** Normalised (MDLs) and doses delivered to the cylindrical set of phantoms during a 1000 seconds cadmium measurement. Varying filter thicknesses. Bare plaster of Paris phantoms.
- Table 5.10** Normalised (MDLs) and doses delivered to the cylindrical set of phantoms during a 2000 seconds cadmium measurement. Filter thickness (1.2 mm)
- Table 6.1** Relative peak uncertainty and resolution for coherent peak adapted from Fleming and Forbes, 2001.

## Chapter 1

### Introduction

#### 1.1 On the Subject of Cadmium

Cadmium (Cd), (Latin *cadmia*, ancient name for zinc carbonate in which cadmium was first discovered as a by-product of the mining of zinc ore) and its toxicity is becoming an increasingly important concern for us (Lauwerys *et al.*, 1991). This is because the toxic effects of cadmium and its compounds on body tissues are extremely severe and thus cause many complications (signs and symptoms). Actually, cadmium is an important environmental pollutant and represents an increasing health hazard to man (Friberg *et al.*, 1974).

Cadmium is released into the air and water by industries and by combustion of household waste due to recycling. Cadmium is used widely in the mining and smelting industry in the manufacture of cadmium alloys *e.g.* solder, surface coatings and the manufacture of alkaline accumulators *e.g.* nickel-cadmium batteries. In industry, cadmium is released into the air as fumes and if these fumes are inhaled they can produce acute, extremely severe inflammation of the lungs that may be fatal. Cadmium is also released into the air by tobacco smokers  $\sim 1 \mu\text{g}$  /cigarette (Börjesson, 1996).

Alternatively, cases of chronic cadmium poisoning can also occur and have been reported by workers employed in these industries (McLellan *et al.*, 1975).

The industrialised practice of mining potentially mobilises toxic metals like cadmium from region to region inevitably allowing for its spread to the soil, surface waters and plants, and unfortunately human activities tend to concentrate it. Cadmium is also mobilised by other industrial and agricultural practices.

Actually, a number of clinical abnormalities have been observed in workers, hence the exposure of cadmium is thus recognised as a potentially serious health problem (Ellis *et al.*, 1977). Moreover, it is not an essential trace element needed for the survival of mankind. The toxicity of cadmium is cumulative in humans, so that under conditions of chronic occupational or environmental exposure several target organs or systems may be affected, viz. lung, kidney, skeleton, and possibly the nervous system.

Consequently, since cadmium has been established as a very highly toxic metallic element even in relatively small quantities (McLellan *et al.*, 1975), it is important to know its exposure effects and if this exposure could become an occupational health hazard. Therefore, it is of considerable interest in quantifying the presence of traces of cadmium in the body. By monitoring the quantities of this toxic element in subjects with occupational exposure, safer working environments can be realised by the use of improved preventative procedures.

## 1.2 Cadmium Health Concerns

Because of the excessive usage of chemical fertilisers and sewage sludge there exist various amounts of different types of toxic elements in the soil and unfortunately cadmium is one of them. As a consequence it is taken up readily by the crops, thus there is an exposure to cadmium through food and water for the general population.

### 1.2.1 Cadmium Toxicokinetics

The water solubility is a very important factor that affects how cadmium-related toxins are distributed in the body and eliminated from the body. The water-soluble compounds of cadmium can be found (amongst other places) in the red blood cells, while fat-soluble ones concentrate in the central nervous system (CNS). The kidneys are the routes of elimination for water-soluble substances, whereas the lungs are for fat-soluble vapours. Thus resulting in these organs as critical targets.

Conversely, inhalation acts as a main route of absorption. Chronic poisoning from inhalation can result in inflammation of terminal bronchioles and alveoli leading to pneumonitis. Smokers have about 4-5 times higher blood cadmium concentrations (about 1.5  $\mu\text{g/l}$ ), and twice as high kidney cortex cadmium concentrations (about 20-30  $\mu\text{g/g}$  wet weight) as non-smokers. This inhalation may also cause a loss of the sense of smell, difficult breathing, coughing, weight loss, and injury of the liver and kidneys. Treatment for this type of poisoning could include the oral administration of calcium edetate.

Cadmium poisoning may also result from the ingestion of an acid food or drink prepared in a cadmium-lined vessel *e.g.* lemonade juice served from cadmium-plated cans.

Nausea, vomiting, and diarrhoea are only a few ailments which usually occur within 15 minutes after ingestion and may subside depending on the quantity ingested, within 24 hours. The oral intake through food is about 10-25  $\mu\text{g}$  /day (Börjesson, 1996), whereas 5% of the cadmium in the food intake is absorbed, however, this value could be higher for persons suffering from calcium deficiencies (Kjellstrom and Nordberg, 1978).

After the absorption of cadmium by the body, it is then transported to the liver. It is not totally clear how cadmium functions or interferes with the human body metabolism. However it may have an indirect effect on the calcium metabolism via vitamin D<sub>3</sub> absorption in the kidney. Cadmium interferes with the metabolism of vitamin D, calcium (possibly causing hypercalciuria) and collagen. The kidneys are responsible for calcium levels in the blood, so that when cadmium levels rise and the kidney tubules fail, the calcium levels drop. To compensate, the body "borrows" calcium from bones. It has been known to cause bone and joint aches and pains. This syndrome was first described in Japan, where it was termed the itai-itai ("ouch-ouch") disease. It especially affected elderly women, who ate a diet heavy in cadmium-contaminated rice; they suffered from severe bone decalcification. Its accumulation may lead to osteomalacia and osteoporosis due to late manifestations of severe cadmium poisoning (Staessen *et al.*, 1991).

In the liver the cadmium effectively stimulates the synthesis of the low molecular weight protein metallothionein (Czauderna and Rochalska, 1989), which is an important transport and storage protein for cadmium. This protein allows for binding, hence the prevention of tissue damage, such as renal tubular dysfunction (Sartor *et al.*, 1992). This

dysfunction, which is associated with chronic cadmium toxicity, has been recognised since 1948 (Gompertz *et al.*, 1983). Tubular dysfunction is characterised by the excretion of low molecular urinary proteins, (microproteinuria) namely  $\beta_2$ -microglobulin since it is known that cadmium decreases tubular reabsorption (Roels *et al.*, 1989). Cadmium has been known to give rise to increased microproteinuria *i.e.* the abnormal excretion of  $\beta_2$ -microglobulin (Fiscator, 1966), hence the loss of renal filtration reserve capacity, and liver damage. However, non-metallothionein binding cadmium may bind with other compounds *e.g.* cadmium may bind with the sulphhydryl groups which may play a role in the pathogenesis of cadmium related tissue injury (Börjesson, 1996).

### **1.2.2 Cadmium Toxicodynamics**

It is important to realise that cadmium does not cross the placenta-fetal barrier nor the blood-brain barrier as lead and mercury do, so it is not toxic to the fetus, and does not cause the mental and brain symptoms of lead and mercury. Cadmium is virtually absent in new-borns but the long term exposure becomes a serious threat because of its relatively long biological half-life >10 years (Buchet *et al.*, 1990). And a daily excretion of 0.01% of the total cadmium body burden (Börjesson *et al.*, 1995). This results in an increase in the total body burden as age increases.

This continued exposure results in damage to the hepatic and renal system, as it accumulates in the liver and the kidneys, (retained mainly in the kidney cortex). The latter is considered the critical organ after long term exposure (Börjesson, 1996). This results in the kidney having more than half of the body burden of cadmium.

In the kidneys, cadmium affects the cells lining the proximal tubules, the portion of the kidneys associated with water and nitrogenous waste processing. And since the kidneys have a significant reserve capacity early kidney damage is difficult to detect. The detectable cadmium damage that is irreversible results in the increased excretion of proteins (tubular proteinuria). This diseased state may lead to total kidney failure in subjects exposed to prolonged cadmium levels, even at low levels (Webb, 1975).

In addition, the zinc-cadmium ratio is very important, as cadmium toxicity and storage are greatly increased with zinc deficiency, therefore good levels of zinc could protect against cadmium related tissue damage. It is believed that cadmium may actually displace zinc in some of its important enzymatic and organ functions; thus interfering with these functions.

As zinc has an affinity for the testes, cadmium is also stored there in higher concentrations than in other tissues. Hence exposure to cadmium can have a significant effect on the male reproductive system *e.g.* reduced sperm count.

Cadmium toxicity has been implicated in generating prostate enlargement, possibly by interfering with the zinc support. Furthermore, there is some evidence that cadmium exposure may increase the risk of some types of cancer *e.g.* lung and prostate cancer (Börjesson, 1996).

A hopeful preventative solution is to take a high quantity of zinc and calcium as these minerals can help protect against further cadmium absorption, actually adequate body levels of zinc may displace some tissue cadmium. In addition iron, copper and vitamin C

have been shown to increase cadmium elimination as well, as can be measured by urine levels.

Despite the removal of the cadmium exposure there is evidence to suggest that cadmium-induced kidney damage is progressively degenerative and hence causes a continued deterioration in the glomerular filtration of the kidneys. Roels *et al* (1989) found that there was significant increase in creatinine and  $\beta_2$ -microglobulin concentration in serum with time. When the kidneys have been severely impaired protein and sugar may be spilled in the urine.

There is information, although limited, which suggests that cadmium may promote renal cancer caused by other organic compounds, especially with high cadmium doses. Hence cadmium may be a renal carcinogen or promoting co-factor. Also there are some studies, which suggest that cadmium might play a role in the pathogenesis of hypertension and that there may be some correlation between cadmium exposure toxic effect and diabetes (Lauwerys *et al.*, 1991).

Finally, if the average daily intake of cadmium would increase to 30  $\mu\text{g}/\text{day}$ , about 1% of the entire population would have cadmium-induced tubular damage. Recent studies in Belgium (which is a principal cadmium producer in Europe) and Japan have shown that environmental cadmium poisoning led to increased excretion of calcium and a decreased bone mineral density in the general population.

### 1.3 Occupational Monitoring Procedures

Since cadmium is at present known to cause several detrimental health effects, such as proteinuria, which is irreversible, occupational monitoring has become a standard practice within companies over the last two decades in which workers are exposed. Actually blood and urine samples using atomic absorption spectrophotometry (AAS) as well as neutron activation analysis (NAA) have become a typical monitoring procedure in the industrial world.

For routine occupational monitoring, blood-cadmium and urine-cadmium levels over the course of an employee's entire work history could be used as a measure of cumulative exposure to this toxin, but there is no simple relationship that relates blood-cadmium to total cadmium toxicity. Also one individual measurement is merely a reflection of current or recent cadmium exposure as blood is not a storage site for cadmium. Actually, urine-cadmium correlates more with total body burden than the blood-cadmium for subjects with normal kidney function. However, due to kidney malfunction the urine-cadmium measurements become unreliable.

When collecting blood and urine samples to be analysed the accepted normal values are < 13 mg/l (13 ppm) for creatinine and < 2 mg/l (2 ppm) for  $\beta_2$ -microglobulin. However when comparing kidney-Cd and liver-Cd for exposed to unexposed subjects, Swedish studies have suggested range 2:1  $\rightarrow$  5:1 ratio and 3:1 ratio respectively (Börjesson, 1996). Furthermore, as with non-invasive *in vivo* measurements of bone-lead and cadmium in the kidneys, measuring bone-cadmium of occupational workers could

provide valuable information to help researchers and doctors improve the monitoring of this toxic element.

## **1.4 Measuring Techniques**

### **1.4.1 Invasive Techniques**

Prior to these newly established techniques, only invasive (in vitro) techniques were available, either atomic absorption spectrophotometry for urine and blood work analysis but unfortunately it has been shown that the relationship between urine-Cd or blood-Cd concentration to long-term exposure is not simply correlated (Ahlgren *et al.*, 1980)

Alternatively, tissue biopsies were another option, however, there are several disadvantages associated with biopsies. Mainly, there are significant risks to the subject under study, thus there are many reproducibility concerns. And furthermore there is the possibility of the specimen sampled to be non-representative of the whole organ under investigation (Vartsky *et al.*, 1977). The contamination of samples could be a distinct possibility, especially when a large number of specimens are being investigated.

### **1.4.2 Non-Invasive Elemental Analysis**

Although there has been significant recent advances in the medical community there exist several limitations. One such limitation is the ability to diagnose trace elements *in vivo* quantitatively; hence there is a need for non-invasive elemental analysis of toxic elements in the tissues or organs of a patient (O'Meara, 1999). For example, the ability to measure the amount of lead in the tibia or calcaneus quantitatively is being pursued at a few specialised institutions. Other elements that have been successfully measured or are under

active development, using these techniques are mercury, uranium, strontium, manganese and aluminium. These modern techniques use the nuclear and atomic properties of atoms to produce spectral or absorption properties that are inherent only to the element being investigated. Because of these new techniques there is hope for the improved etiology of toxic diseases *e.g.* there is evidence to correlate total body nitrogen measured to the renal state of the patient being considered. Thus with these treatment modality options, the medical profession can utilise these methods to obtain their information. With these findings known, preventative or controlled procedures can be put into place that could avoid or at least alleviate the severe complications that occur with enhanced detrimental effects, which arise from the toxicity of these heavy elements.

The two *in vivo* gold standards are XRF and neutron activation analysis (NAA), despite the fact that XRF is limited in that the measurement sites should be superficial, as the sensitivity of the XRF measurement is extremely dependent on tissue or organ depth. However, it is clearly obvious that the XRF has a dosimetric advantage, but that the neutron method can be expected to obtain information more reliably (Chettle and Fremlin, 1984).

## 1.5 Research Investigations in XRF

From the literature reviews of many published papers dated as far back as the early seventies, XRF measurements were being developed. Initially XRF was introduced for the measurement of iodine in the thyroid. This technique worked adequately because the thyroid gland is relatively superficial and the iodine concentration in the thyroid is fairly high  $\sim 400 \mu\text{g/g}$  (400 ppm) (Mattsson and Scott, 1990). Consequently, many pilot studies have evolved using XRF in trace elemental research, especially for high Z materials *e.g.* uranium (O'Meara, 1999).

Pioneering studies of cadmium have focused primarily on the kidney as the preferred measurement site simply because the kidney is the major long-term storage site of cadmium. In addition, many institutions have opted for the NAA technique, using the  $^{252}\text{Cf}$  or  $^{238}\text{Pu}/\text{Be}$  based systems because NAA is less sensitive to tissue depth and positioning. Actually, the latter  $^{238}\text{Pu}/\text{Be}$  based system is preferred since the system performs as well as or better, without the drawback of the relatively short half-life of  $^{252}\text{Cf}$  (Franklin *et al.*, 1990).

In 1981, Ahlgren and Mattsson, at the Lasarettet Institute, Lund, Sweden used 11 GBq  $^{241}\text{Am}$  source ( $E_{\gamma} = 59.54 \text{ keV}$ ) to generate characteristic  $K_{\alpha}$  X-rays of cadmium. The MDL obtained ranged from 20 ppm to 40 ppm for skin–kidney surface distance of 30 mm to 40 mm. The delivered mean absorbed dose to the kidney for these measurements was 0.6 mGy in 30 minutes. Then by using partly plane-polarised photons from an X-ray generator, the MDL was reduced to 9 ppm (Christoffersson *et al.*, 1983). Further studies

showed that the MDL could be reduced to 6 ppm (Christoffersson *et al.*, 1987) which could further be reduced by factor of 2. This was demonstrated in the case of iodine by Kaufman, (1979), if the Ge detector was replaced with a large Si(Li) detector, then an MDL near 3 ppm could be achieved (Nilsson *et al.*, 1990). Also recent work at the University of Guelph, Ontario, Canada by MacKenzie (1997) suggests that a MDL of 1.5 ppm could be obtained by the use of shadowing to suppress pulses due to near-surface scattering of primaries, hence reducing background. Interestingly, the technique retained the original americium-241 source and germanium detector.

In Belgium, results from various toxicological studies suggest that their population have shown significantly higher blood cadmium levels than is to be accepted. Therefore, in Belgium this toxin has become a public health concern. However, although environmental exposure to toxic metals is constantly being monitored there has been no evidence of bone-cadmium measurements using XRF. This study would be interesting in that the bone *e.g.* tibia is a relatively superficial tissue and hence should stand an excellent chance of being a preferred measurement site for cadmium, although bone is not the major storage organ for cadmium. Thus, this pilot study is being pursued because the tibia as a measurement site, as with lead measurement, would be easier to set up than the kidney, which tends to vary significantly from person to person with differences of overlying body fat. At present, prior to kidney measurements one must go for an ultrasound to have their kidney's position and depth determined. This research would alleviate these measurement concerns.

This thesis is therefore a study that will assess the feasibility of the source-base technique and the polarised technique and then compare them to each other. As a standard, the feasibility of a system is determined by its MDL. The lower the estimated MDL, the more feasible the system. Moreover, the MDL of any system is calculated by obtaining the peak data collected as a spectrum. The characteristic X-rays of the element under investigation produce peaks for consideration. These peaks are produced by alpha or beta X-rays. Thus, the MDL determined using information from the alpha peak is called the alpha MDL, likewise the MDL determined using information from the beta peak is called the beta MDL. The alpha and beta MDL would be determined using the standard analysis of the *in vivo* spectra by the Marquardt method to obtain X-ray intensities. The final MDL would be calculated using the inverse variance weighted mean of the alpha and beta estimates. The dose given would also be determined and the MDL normalised to dose for the different systems.

## Chapter 2

### Principles of X-ray Fluorescence

#### 2.1 X-ray Fluorescence

X-ray Fluorescence (XRF) is the emission of characteristic X-rays from a target element after an incoming photon interacts with an atom. This process involves the excitation of the atom by the incident radiation via the photoelectric effect, which leaves a vacancy in one of the inner shells of the atom. The 'excited' atom can then return to its ground state when there is a transfer of an electron from some outer level to a vacant inner level *i.e.* an electron that is less tightly bound falls to fill the vacated space. This is a competitive de-excitation process between the ejection of Auger electrons and characteristic X-rays. When the fluorescence yield is high, the emission of X-rays is more favourable.

#### 2.2 Photons Interactions with Matter

When photons ( $\gamma$ -rays or X-rays) are produced from the nucleus and atomic shell respectively, there are a large number of possible interaction mechanisms that can occur as they traverse and interact with the adjacent matter. However, two interaction mechanisms play important roles in the phenomena of XRF: Photoelectric absorption and Compton scattering. Both of these processes result in the partial or complete transfer of photon energy to electron energy (Knoll, 2000).

In the Photoelectric Effect, a photon usually undergoes an interaction with one of the most tightly bounded (K shell) electrons in an atom. In this interaction, the photon transfers all of its energy to an electron in that shell. This energetic electron is then ejected causing an excited atom, formed from the creation of an inner shell vacancy. For the atom to de-excite back to its ground state, an outer shell electron must fill the vacancy created. This results in a decrease in potential energy of the atom. Hence an X-ray (characteristic of the element) or an Auger electron with energy corresponding to the difference in shell binding energies is liberated. Actually, the resulting X-ray energy is dependent on the energy level of the ejected electron and on the element concerned.

Importantly, the electrons of any atom orbit the atom in shells *e.g.* K, L, M, etc. with the highest energy X-rays being associated with the K shell electron interactions. When the K-shell vacancies are filled by L-shell electrons  $K_{\alpha}$  photons are produced, whereas when the M-shell or higher electrons fill the K-shell vacancies  $K_{\beta}$  photons are produced. The  $K_{\beta}$  photons are produced with larger energy than the  $K_{\alpha}$  photons, since the energy difference between the K and M shells is larger than the K and L shells. See table 2.1 *e.g.* the  $K_{\alpha 1}$  X-rays have energy of 23.174 keV, with an intensity of 46.1. Similarly, L X-rays are emitted from the ejection of an L-shell electron and so on.

**Table 2.1: Cadmium K-shell X-ray characteristics (a)**

X-ray line	Energy (keV)	Emission (per 100 K-shell vacancies)
$K_{\alpha 1}$	23.174	46.1
$K_{\alpha 2}$	22.984	24.5
$K_{\alpha 3}$	22.693	0.001
$K_{\beta 1}$	26.095	7.69
$K_{\beta 2}$	26.644	1.98
$K_{\beta 3}$	26.060	3.99
$K_{\beta 4}$	26.702	0.008
$K_{\beta 5}$	26.304	0.060

(a) Firestone *et al.*, 1996.

The *in vivo* XRF technique relies heavily on the photoelectric effect. But this photoelectric interaction probability is strongly energy dependent. In addition, the photoelectric effect is approximately proportional to  $Z^n$ , where  $Z$  is the atomic number and where the exponent  $n$  varies between 4 and 5 over the  $\gamma$ -ray energy region of interest (Knoll, 2000). Also, before the photoelectric effect can occur the incident photon must have energy greater than the absorption edge of a particular shell of the element under investigation (The K edge of cadmium is 26.711 keV). Otherwise the ejection of electrons from the shell would be impossible. In general, energies just above, within a few keV of the absorption edge produce the highest K-shell photoelectric cross section, which implies that these photons would have a high probability of undergoing photoelectric events.

This requirement assures that the maximum signal is generated per incident flux *e.g.* one of the most successful XRF system uses  $^{109}\text{Cd}$  to excite the lead  $K_{\alpha}$  electrons *i.e.* photons of energy of 88.035 keV are used to excite the lead  $K_{\alpha}$  electrons (88.005 keV) (Somerville *et al.*, 1985).

**Table 2.2: A comparison of the characteristics of the possible isotopic sources for Cadmium X-ray fluorescence measurements. (b)**

Isotope	Principal $\gamma$ -ray energy (keV)	Photoelectric cross section ( $\text{cm}^2\text{g}^{-1}$ )	Energy of peak in Compton distribution (keV)		
			90° geometry	180° geometry	
<sup>125</sup> Te	$\alpha$	27.4	48.8	25.8	24.6
	$\beta$	31.1	34.9	29.3	27.7
<sup>125</sup> I		35.5	30	33.2	31.2
<sup>241</sup> Am		26.3	–	25.0	23.8
<sup>109</sup> Cd		59.5	5.6	53.3	48.3
		88.035	1.8	75.1	65.5

Note that the Te X-rays are produced from the electron capture decay of the <sup>125</sup>I source and the internal conversion of the 35.5 keV  $\gamma$ -rays. (b) Lederer & Shirley, 1978.

In general, the lower the magnitude of the background in the characteristic X-ray energy ‘Region of Interest’ of the detected spectrum, the better the detection limit. As the principal background arises mainly from the inelastic scattering of the source photons, the source geometry can be varied to minimise this background. The background is minimised by maximising the difference in the energy of this peak value and the energies of the characteristic X-rays.

By definition Compton Scattering, or incoherent scattering, is the inelastic scattering of a photon from an atom. In this interaction between the photons and matter we assume that the photon is incident on a stationary free electron. (Clearly, this is not the case).

Interestingly, the final energy of the scattered photon  $E'$ , hence the energy of the Compton peak, is given by the following equation:

$$E' = \frac{E}{1 + \frac{E}{m_0 c^2} \cdot (1 - \cos \theta)} \quad (2.1)$$

Where  $E$  is the incident photon energy,  $m_0 c^2$  is the rest mass energy of the electron,  $\theta$  is the angle of scatter (the source-detector geometry)

The above equation is used to shift the dominant Compton peak so that the background is minimised, as this peak offers little information for the *in vivo* XRF analysis of tissues. Note that the detector records the photon energy as a distribution of scattered photon energies because of Doppler broadening (momentum broadening). Another type of scattering of concern in the analysis of *in vivo* XRF is coherent scattering. This is the elastic scattering of a photon from an atom, and results in the emission of a photon with unchanged energy. In Coherent scattering the photon interacts with a much larger object than Compton scatter where the entire atom is involved as compared with one electron. Therefore the kinetics associated with the scattering process is different due to the difference in the mass of the scattering object. The photon can be scattered through an angle  $\theta$ , basically without any energy loss, hence only the direction of the photon needs to be considered after the scattering event, as the energy is assumed to be constant.

Mathematically, the differential cross section for coherent scattering can be represented by the following equation:

$$\frac{d\sigma}{d\Omega} = \frac{r_o^2}{2} \cdot (1 + \cos^2 \theta) |F(v^2)|^2 \quad (2.2)$$

Where  $r_o$  is the classical electron radius,  $\theta$  is the angle of scatter and  $F$  is the atomic form factor as a function of  $v^2$ , which itself is dependent on both the photon energy and  $\theta$ .

At large scattering angles, the cross section varies by  $Z^5$  or  $Z^6$ , therefore high  $Z$  elements tend to dominate the coherent scattered photons at these angles. It must be noted that this coherent peak is usually used for normalisation in bone measurements because it generally gives a large cortical bone cross section. Also, this peak and the X-ray intensities depend only on the uncollided gamma ray flux. In addition, the attenuation differences between the elastically scattered gamma rays and the X-rays are fairly negligible over the effective thickness (Mattsson and Scott, 1990).

**Table 2.3: Comparison of Coherent Cross-sections for 88 keV photons (Mattsson and Scott, 1990)**

Medium	Cross section ( $\text{cm}^2 \text{g}^{-1} \text{steradian}^{-1}$ ) $153^0$
Soft tissue	$1.5 \times 10^{-6}$
Cortical bone <i>e.g.</i> tibia	$41.8 \times 10^{-6}$
Plaster of Paris ( $\text{CaSO}_4 \cdot 2\text{H}_2\text{O}$ )	$50.8 \times 10^{-6}$
Paraffin wax ( $\text{CH}_2$ ) <sub>n</sub>	$0.2 \times 10^{-6}$

### 2.3 Sources of Photons

Many elements have several unstable isotopes that are known to emit  $\gamma$ -ray radiation. Isotopes, which emit a particular radiation, are commonly referred to as radioactive sources. Reference sources are fundamentally necessary in any measurement associated with photon radiation. These reference sources are chosen so that they have excellent energy calibration properties. Thus their nuclear states should have definite energy levels, so that their decay transitions are very specific. Generally, there are encapsulated radioisotopic samples of a few micro-curies. The encapsulation acts as a shield to prevent the associated radiations other than  $\gamma$ -rays from escaping. For efficiency calibrations, sources with thinner encapsulation are required, as the shielding from the capsule causes significant attenuation and excessive scattering, which tends to interfere with this application.

Alternatively, X-rays can be used as a source and thus can be produced by conventional X-ray tubes or by external electron beams. In these external electron beams, fast electrons are created by the use of a large supply voltage placed across the tube. As these electrons interact with matter, part of their energy is converted into electromagnetic radiation. The amount of electron energy converted increases with operating voltage. However, this method of photon production results in a continuum of different photon energies (Bremsstrahlung spectrum). This continuum of photons represents the unwanted background.

Theoretically, characteristic X-rays are created when the fast moving electrons impinge upon a target. These X-rays that are detected are seen as superimposed peaks on top of an

underlying background. Fortunately, the spectrum can be modified by the use of filters. Filters predominantly remove the lower energy photons. Filtration minimises the background by the removal of photons that have less energy than is necessary for the production of X-rays.

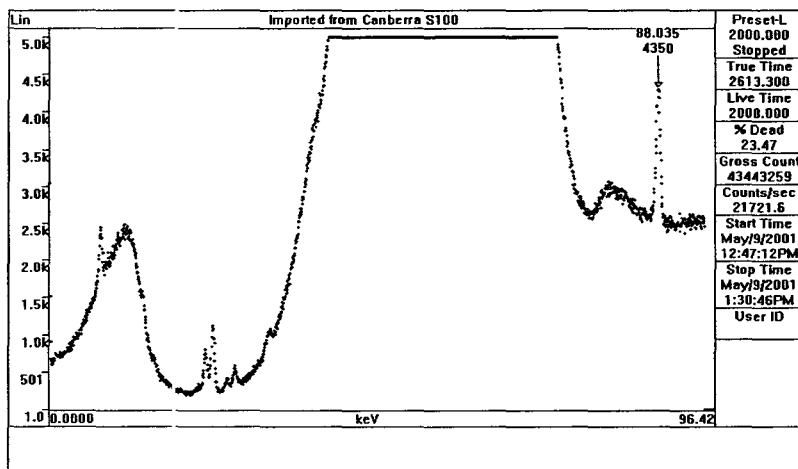


**Figure 2.1: Spectrum detected during a 2000s (live time) measurement of the 170 ppm cadmium-doped plaster of Paris phantom using the  $^{109}\text{Cd}$  source in a backscatter geometry sample to detector distance, 2 cm. Note the coherent peak at 88.035 keV, and the dominating Compton peak, very large and tailing off to the left. Also the Cadmium peaks can be seen clearly as they appear in the valley of the background.**

## 2.4 Source-Excited X-ray Fluorescence

Source-excited X-ray fluorescence is one of the two techniques that are used in XRF. When this method is employed, the designing of the optimal source orientation *i.e.* angular geometry and positioning; and photon energies are the main considerations to ensure maximum signal to background ratio. Therefore, the source-sample-detector geometry must be optimised for the given source being used. When  $^{109}\text{Cd}$  is used to excite the photons in the bone-Cd doped phantoms, the signal appears to be maximised when the Compton peak is shifted in such a way (to the right) that the background from the scatter is minimal. This is seen in figure 2.1.

However, due to the limitations of the system, some radioactive  $\gamma$ -sources cannot find an orientation that would reduce the background sufficiently to be considered acceptable. This problem is noticed because there are limited sources that give a large enough photoelectric cross-section for interaction and also very often there is only a fixed range of possible angles of scattering for these sources. In these cases, other means of minimising the background in the X-ray energy region of interest must be investigated in order to acquire a reasonable sensitivity for measuring concentrations of trace elements. One such technique that achieves background reduction is the use of plane-polarised photons. These plane-polarised photons are used as the source of excitation of the characteristic X-rays.

## 2.5 Polarised X-ray Fluorescence

The phenomenon of polarisation through scattering has been studied experimentally since the beginning of this century (Barkla, 1906). From these studies, the Klein-Nishina formula was developed to determine the probability for incoherent scattering (if dominant) of polarised photons. Mathematically, the differential Compton (or incoherent) scattering cross-section for polarised radiation, hence the probability of scattering can be determined by the below formula:

$$\left. \frac{d\sigma}{d\Omega} \right|_{incoherent} = \frac{r_o^2}{2} \cdot \left( \frac{\nu'}{\nu} \right)^2 \cdot \left( \frac{\nu}{\nu'} + \frac{\nu'}{\nu} - 2 \sin^2 \theta \cos^2 \psi \right) \quad (2.3)$$

Where  $r_o$  is the classical electron radius,  $\nu$  is the frequency of the incident photon,  $\nu'$  is the frequency of the scattered photon energy,  $\theta$  is the angle of scatter, and  $\psi$  is the angle between the plane of incident polarisation and the scatter plane.

From this equation, it is obvious that the probability of scattering is dependent on both the photon energy and the scattering angle.

For example, the differential scattering cross section is minimised when  $\psi$  is  $0^\circ$  and  $\theta$  is  $90^\circ$ , implying that there exists a direction in which the intensity of Compton scattered photons being detected is a minimum. This direction corresponds to the direction of initial polarisation. In practice, the radiation will never be totally polarised due to multiple scattering (in the polariser and the sample) and the non-zero solid angle effect

(collimating ability of the system). Therefore, by carefully positioning the detector, a minimum background can be obtained.

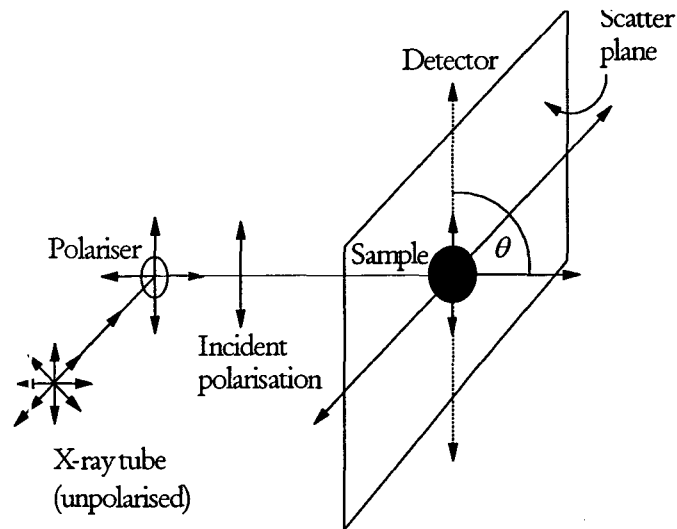


**Figure 2.2: Unpolarised photons from a X-ray tube are polarised before interacting with the sample (O'Meara, 1999).**

This technique was the solution for many trace elemental measurements in which background produced from Compton scattering was a problem. Several researchers, *e.g.* Kaufman and Camp, 1974, who obtained a four-fold reduction in the Compton scatter peak detected for the iodine measurement, have used this technique successfully. By using plane polarised XRF, Borjesson *et al.*, 1995, were able to measure mercury levels in the kidney.

## 2.6 Photon Detection Systems

In the XRF technique many photons of differing energies are emitted and thus some means of detection is necessary. First, in order for the detector to serve as a photon spectrometer, it must act as a conversion medium for the primary photons, since these can go unnoticed because they have no charge or mass; so the detector must create a high probability of interaction for the photon. In practice, solid detection media are preferred since the mean free path of photons is considerably long compared to charged particles that the detector size would have to be very large if other media were used. Solid detector media have larger densities than gaseous and liquid detector media; therefore these media could be made smaller in size.

It should be noted that the detector size affects the efficiency of the system, but detector response is a fundamental property necessary for good XRF spectroscopy. Therefore when making detector type considerations, there is typically a trade-off between counting efficiency and resolution for which the detection of the system is optimal; as detector response is indicative of the detector's own limiting resolution. Actually, the energy resolution, the dead time and the efficiency of a spectroscopy system are all affected by the energy of the emitted photons. So the choice of detector to be used is governed by the type of spectrum desired and the energy of the photons being recorded.

In the detection of photons produced from XRF there are two major detector categories: inorganic scintillators, of which NaI(Tl) is the most popular and solid-state detectors *e.g.* hyper-pure germanium (HPGe) and lithium-drifted silicon (SiLi) detectors.

The advantage of the NaI(Tl) detector is its high efficiency for stopping incident photons due to its high density and large size availability. Also, complete energy absorption can occur because of the presence of iodine (relatively high  $Z = 53$ ), therefore the detected photons are usually recorded in the correct energy channel.

Preferentially, solid-state detectors are used because of their excellent resolution; they are superior to the scintillators. Good resolution ensures the closely spaced characteristic X-ray peaks are separated and ensures that the peaks be narrow, but tall, making them more pronounced and clearly visible above the statistical noise of the continuum. Usually, this improved energy resolution comes at a price, the detection efficiencies of germanium crystals can be an order of magnitude lower than NaI(Tl) since germanium detectors are generally smaller in size and have lower atomic number than NaI(Tl) (Knoll, 2000). However, when the energy is low, of the order 100 keV, the efficiency of germanium crystals is still quite good (~90 %). Moreover, in the cadmium measurement system, the K-shell X-rays being measured had energies, which were even lower, actually of the order of 25 keV (see table 2.1), hence the use of a lithium-drifted silicon detector may be preferred over the hyper-pure germanium.

The *in vivo* analysis research group at McMaster University uses hyperpure germanium detectors for high atomic number spectroscopy measurements and lithium drifted silicon detectors for lower atomic number spectroscopy measurements. The details of the XRF system used for the measurement of cadmium would be discussed more extensively in chapter 3.

## Chapter 3

### Experimental methods

#### 3.1 System Description of the Cadmium Measurement System

The preparatory step in the development of a successful bone-Cd X-ray fluorescence measurement system is primarily governed by the detection system that is employed. Since X-ray fluorescence is based on the excitation of characteristic X-rays from an elemental target, a source of photons is required to cause the emission of characteristic X-rays from the cadmium phantom target. A detector, preferably solid state, is needed to collect and record the newly produced X-rays, which unfortunately, are rapidly attenuated as they are emitted from the target. In addition to the above mentioned, a means of calibration is also paramount. This is achieved by the use of a series of cadmium phantoms to which varying amounts of cadmium have been added. Therefore, in the contriving of such a system, these requirements become the crucial factors responsible for the ultimate success of the X-ray fluorescence system.

In this pioneering study, there was careful selection of a photon source for the excitation of the characteristic X-rays for the optimisation of the cadmium system using the XRF technique. Two types of photon sources were considered; the photon source was either a mono-energetic radionuclide  $\gamma$ -ray source or the partly plane polarised output of an X-ray

tube. Referred to throughout this thesis as source-excited X-ray fluorescence, or polarised X-ray fluorescence respectively. For both XRF systems, a number of design parameters were considered in the optimisation of the excitation source.

To reiterate, from chapter 2, solid-state detectors either hyper-pure germanium or lithium-drifted silicon detectors were preferred. Theoretically, hyper-pure germanium detectors and ultra-fast electronics are almost invariably the superior choice for X-ray energies greater than 30 or 40 keV. Whereas lithium-drifted silicon detectors are preferred for L X-ray fluorescence or for K X-rays from elements of atomic number less than 40 or 50, as these elements have X-rays that are of lower energy.

The aim of this thesis is to assess the feasibility of a bone-Cd XRF measurement system and in addition determine which system would be better for such measurements. System calibration is achieved by the use of a series of phantoms which were created using plaster of Paris doped with different trace quantities of cadmium to mimic the cadmium accumulated bone. From these varying cadmium concentration phantoms, the characteristic X-rays are emitted and then collected by some appropriate detection system. Figure 3.1 shows a germanium detection system.

### 3.1.1 Detection Systems

The  $^{109}\text{Cd}$  source-based system was used to excite the target, where cadmium doped phantoms represented the target. With this system, a series of preliminary results were investigated. These initial results were required to establish system optimisation. The signals from the detector were then analysed.

For the polarised XRF, the system was shielded with a layer of tin, then aluminium and lead on the photon emitting side. This layer of shielding prevented the release of the undesired internally scattered unpolarised photons.

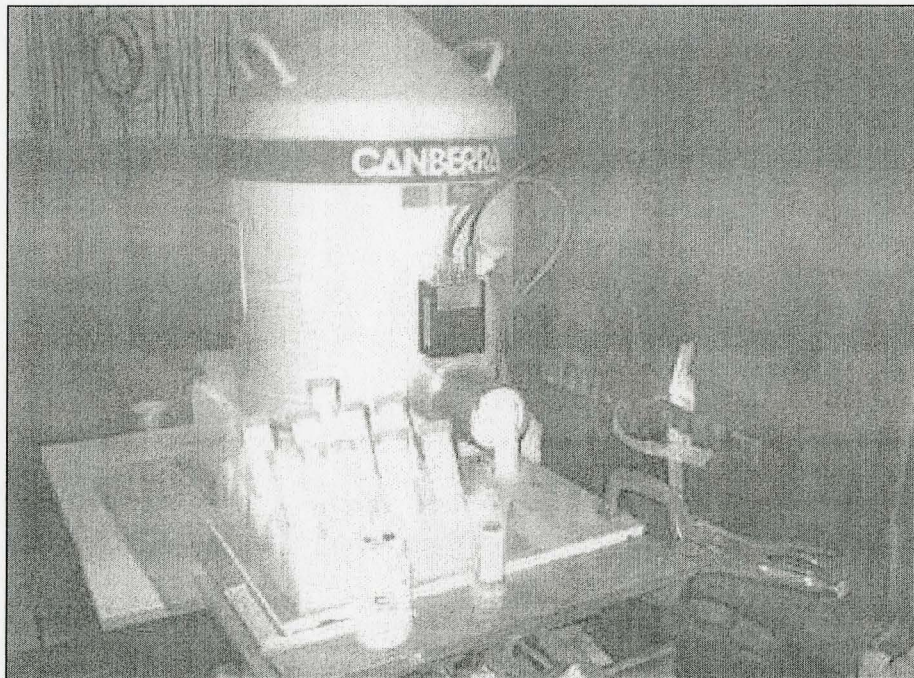


**Figure 3.1: Germanium detection system**

Some preliminary experiments were done using the hyper-pure germanium detectors. In this work the two detectors types (Ge Canberra, model GL2020R serial number 9912755 and Ge Princeton Gamma Tech. NIGP 2020, model RG158/C, serial number 2796) have been investigated to find the more suitable one. The Ge detector serial number 9912755 was used first operating with varying shaping times ranging from 0.5  $\mu\text{s}$  to 10  $\mu\text{s}$  and varying gains ranging from 10 eV/Ch to 500 eV/Ch. It was found that this detector worked best with shaping times of 1-2  $\mu\text{s}$ . This detector, Canberra HPGe (model GL 2020R) had an active face of 2000 mm<sup>2</sup>, thickness 20 mm and a beryllium entrance window with cross sectional area of 20.4 cm<sup>2</sup> (Canberra, 1991). The detector resolution was found to be 650 eV when operated at -2500 V for the given cadmium energies.

Before the measurement of each series of spectra, the gain on the detectors was adjusted. Initially, a gain of 70 eV/Ch was used for the double-headed detector (model RG158/C), but then a gain of  $\sim 50$  eV/Ch was used for the Ge detector (model GL2020R). To keep the gains (at 70 and 50 eV/Ch) similar from experiment to experiment, the 22.98 keV peak was set at a standard position of 327 and 476 channels respectively. If a gain shift was observed throughout one set of experiments, then that was adjusted by recalibration of the computer analysis software of the acquired spectra.

Having obtained an optimal shaping time of 1-2  $\mu\text{s}$  with the above mentioned detector, a second detector was used. This was a double-headed HPGe detector that was operated at -2500 V and a 1  $\mu\text{s}$  shaping time. Although this detector had two entrance windows, only one of them was used. As its heads were covered by aluminium, the photon fluence was

reduced slightly. The signals from all detectors were acquired by using conventional electronics systems, and the data were further analysed.

The analysis of data was accomplished by connecting the detectors independently to a Canberra charge sensitive preamplifier (2001 CP, model 1405), then to a fast spectroscopy amplifier (Ortec, model 572). From this amplifier, an analogue-to-digital converter converted the intensity of the amplified signal from the detector to a digital address. This information was then sent to a personal computer, where spectra were acquired and saved using the commercial software, Canberra S100.

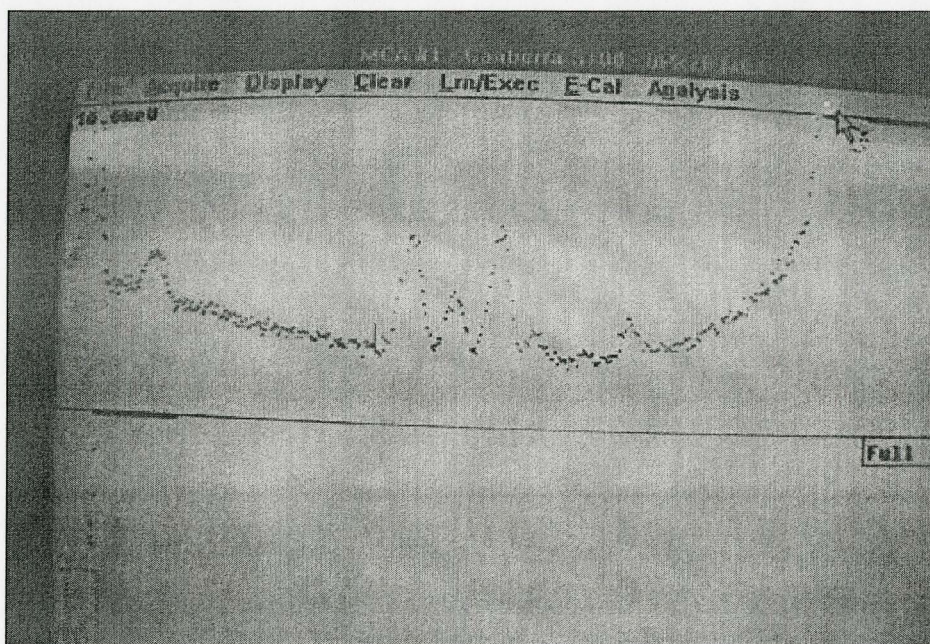


**Figure 3.2:** Typical spectra acquired by the use of HPGe detectors using the Canberra S100 software.

## 3.2 Design Parameters

### 3.2.1 Effects of Geometry

When the source-based system is arranged in a  $180^\circ$  back scattering geometry (see figure 3.3), the distance between the source and the phantom greatly affects both the photon fluence incident on the phantom and the emitted characteristic X-rays detected by the detector. Thus, the necessity of an optimal measurement distance. This optimal distance was mainly determined by the detector response as a distance too close would result in an increase in throughput, hence the dead time, therefore a loss in resolution. Conversely, as the source to sample distance is increased, the throughput is reduced since the characteristic X-rays are emitted isotropically.

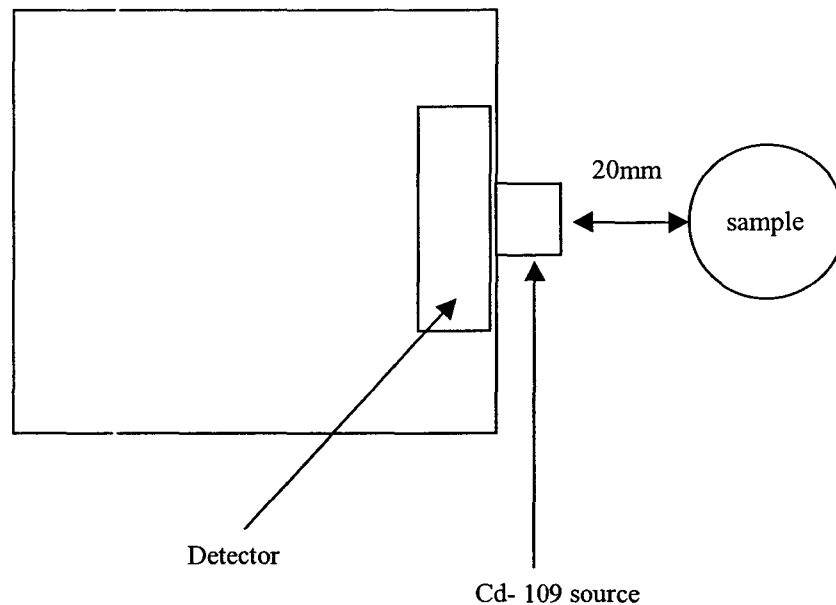


**Figure 3.3: Experimental set up of the  $^{109}\text{Cd}$  system for the *in vivo* measurement of cadmium. Geometry used for simulating the  $180^\circ$  backscatter.**

When  $90^\circ$  geometries are used, as in the polarised technique, the positioning becomes more critical and more over, there are two distances to be considered: the source to sample distance and the sample to detector distance. The  $90^\circ$  geometry can also be applied to the source-based method. However, in the designed cadmium measurement system, this geometry was not employed, as it would have resulted in a smaller shift in the Compton peak. Therefore, producing a larger background in the region of the characteristic X-ray spectrum, as the cadmium X-rays lay in the valley of the background spectrum when a  $180^\circ$  backscattered geometry was used. This occurrence presented a potential advantage of using the 88 keV  $\gamma$ -ray from  $^{109}\text{Cd}$ . For the polarised system in the  $90^\circ$  geometry, shown in figure 2.2 and figure 3.5, the detector was positioned on-axis with the centre of the bone cylinder. This positioning was applied, regardless of its position within the soft tissue cylinder, and this position corresponded to the height at which the polarised beam was emitted from the X-ray tube. This was essential to ensure optimal detection of the irradiated phantom. For the preliminary polarised experiments, the sample to detector distance was varied from  $(12.0 \pm 0.5)$  mm to  $(42.5 \pm 0.5)$  mm.

### 3.2.2 Collimation

When using source based XRF, the difference in collimator length was investigated. As collimation of the source should affect the incident photons on the detector as well as reduce the overall scattered dose.

Initially, the source used for the irradiation of the phantoms was encapsulated inside a tungsten collimator 8.75 mm in length, 0.6 mm diameter, which was later varied to test its effect on the system's normalised MDL.

The collimator comprised of 2 cylindrical bores as shown in figure 3.4. Inside the collimator, the source was placed in the lower portion of the collimator, whereas a copper filter was fitted externally on the upper part of the collimator. Note that only the bore of the collimator varied when the length of the collimator was varied.

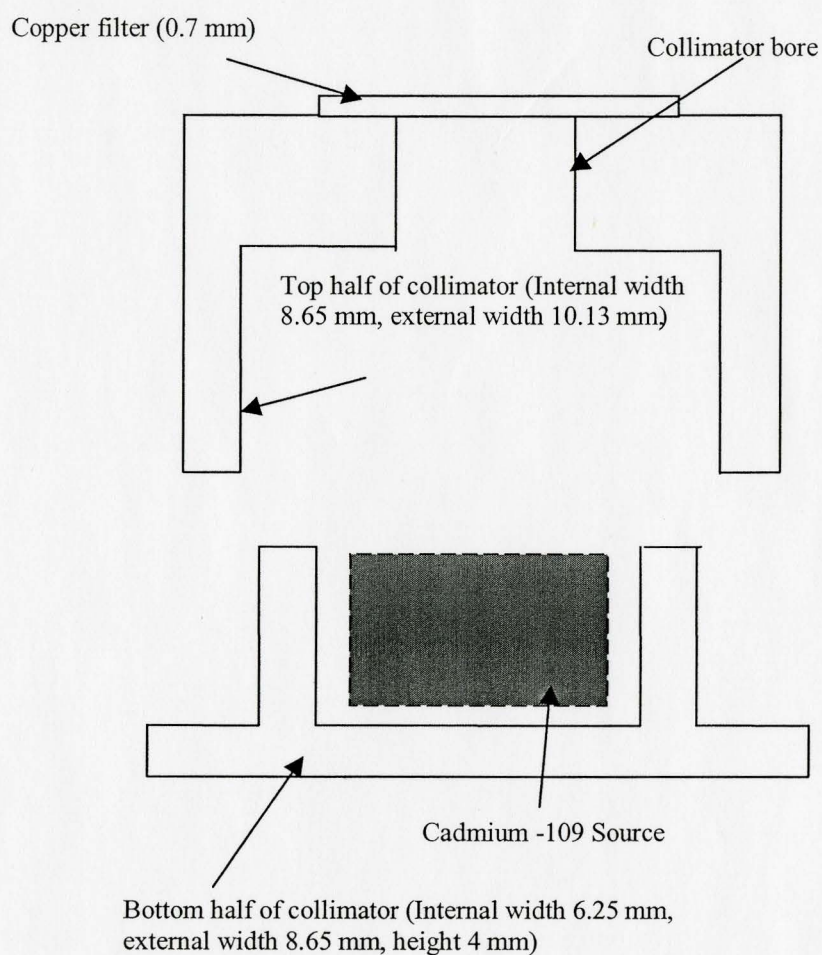


**Figure 3. 4: Collimator dimensions used for the source-based collimation, the length of the bore was varied to acquire the variable collimator length.**

### 3.2.3 Tube Current and Voltage

Previous studies with other toxic elements suggest that a larger tube voltage as well as a larger tube current may give rise to a more sensitive system. So based on this knowledge, the voltage and current effects on sensitivity were investigated to verify these findings. The machine used in this research for the generation of X-rays was the Phillips RT 250 (III) Depth Therapy Generator, which had only four possible operating voltages, namely 75, 125, 175 and 250 kV.

The tube parameters for measuring bone cadmium with polarised XRF were studied. Initially, the voltage was varied with the current being set constant at 12 mA and then the voltage was held constant at 175 kV (optimal determined voltage for this system) as the tube current was varied from 9-16 mA (the current range of the Phillips RT 250 (III)).

### 3.2.4 Polariser Material

As seen by previous studies, the degree of polarisation of a system affects the throughput, because as the polariser's thickness is increased, the incident fluence is increased, therefore the detected signal is increased. However, as the thickness of the polariser is increased, there is an increase in the probability of multiple scatter events and this results in a decrease in the polarisation, which is realised by an increasing background under the characteristic X-rays in the detected spectrum. Thus the sensitivity is affected, as it is inversely proportional to the square root of the background and directly proportional to the signal.

From theory, aluminium results in a higher yield per incident fluence than copper so it was preferred, although copper could be used as it gives a higher mean photon energy distribution. Other materials were not chosen, as they were either not readily available or definitely not economically viable. Whereas other metals, like tin were not considered as their photoelectric cross section resulted in characteristic X-rays, which were a substantial component of the spectrum, thereby reducing both the polarisation and the mean photon energy incident on the sample. This ensured that the greatest fluence is incident on the sample. Fortunately, filtration can be used to tailor the photon energy distribution, if the arrangement resulted in an excessively high-count rate in the detector electronics or unacceptable subject dose. Therefore, a 1 cm aluminium polariser, as used in previous polarised systems at McMaster University, was deemed adequate for the cadmium measurements.

### **3.2.5 Filtration**

As discussed previously, filtration can be considered as a means of reducing the subject dose associated with a measurement, as the fluence of the irradiating beam is reduced. This reduction of the incident photon fluence has the advantage in that it enables the detector and the associated electronics to handle the counting rates effectively.

Theoretically, as the incident fluence increases, the throughput rate increases and when this continues to increase, it eventually causes the saturation of the electronics. This increase in the throughput rate increases the dead time in the system. And when this occurs, the detector resolution rapidly deteriorates especially if a dead time of 40 % is exceeded. Therefore, it is better to operate the system at a throughput rate, which is less

than the saturation level of the electronics, as this would prevent the detector resolution from being compromised. This requirement may result in a longer acquisition time. Thus, there exists a trade-off between throughput and resolution. So this trade-off was studied to establish an optimal filter thickness for filtration. Figure 3.5 shows the polarised XRF system using an external copper filter. The thickness of these filters was varied from 0.2 mm to 1.7 mm. Note that an internal diagram of the polarisation was shown previously in Figure 2.2.

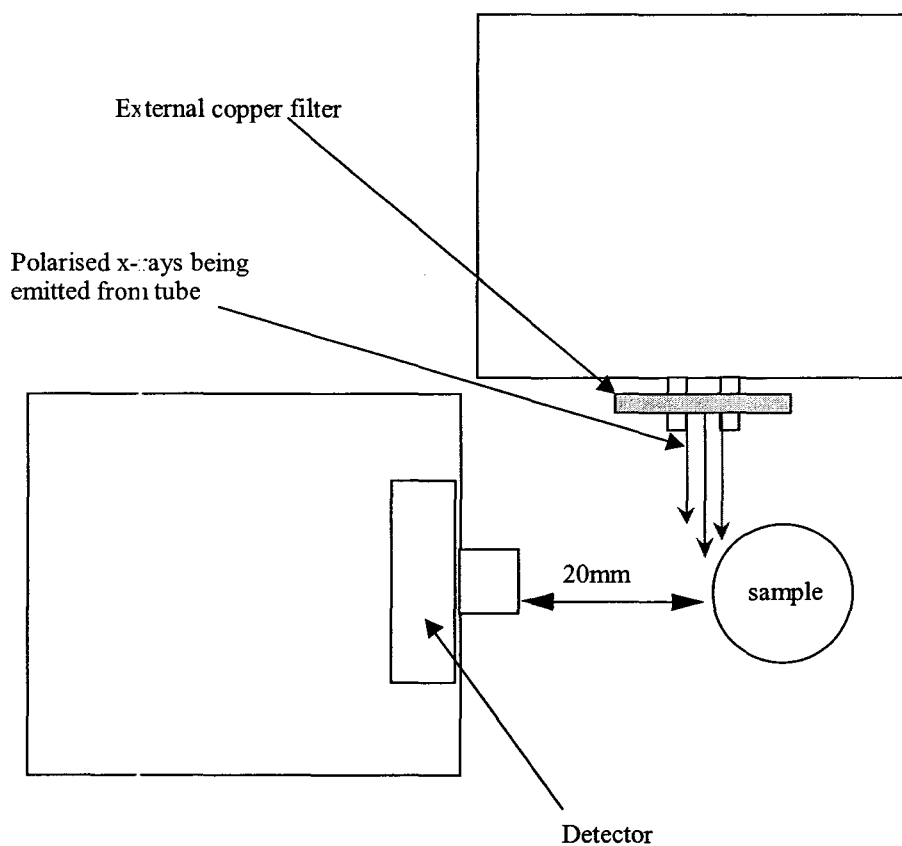


**Figure 3.5: Experimental set up of the polarised XRF system for the *in vivo* measurement of cadmium.**

### 3.3 Phantoms

#### 3.3.1 Design and preparation

After optimising the system parameters, precision measurements were conducted to assess the newly designed system. However, for the bone precision investigations, a calibration was required. This calibration was performed, by using materials analogous to bone for which the system was designed. This analogous subject medium was referred to as a phantom, where the materials for which the phantoms were prepared, were carefully chosen.

Since the phantoms were mimicking the subject's bone, a material was selected so that the phantom would exhibit a similar photon interaction cross section to the bone. In addition, there was need to consider the relative coherent cross sections in the selection of a phantom material for bone measurement systems to verify if the coherent scatter peak could be used for normalisation.

Actually, plaster of Paris ( $\text{CaSO}_4 \cdot 2\text{H}_2\text{O}$ ) was used, as this material has a similar mass attenuation coefficient as bone at 20 keV. Hence, plaster of Paris will have similar attenuation properties to bone. Mainly, the incident fluence of the characteristic X-rays would be similar in this energy range. However, there is a difference between the coherent scatter cross sections of these materials,  $5.831 \text{ cm}^2\text{g}^{-1}$  for plaster of Paris, and  $4.001 \text{ cm}^2\text{g}^{-1}$  for bone (Berger, 1987) at 20 keV. This is non-ideal, as many of the trace elemental bone measurements use the coherent scatter signal as a normalisation factor. Generally, in lead and uranium studies, before calculating the metallic concentration through calibration ratios from plaster of Paris phantoms, a correction for the detected X-

ray to coherent ratio is required. This is to account for the difference in the total scattering cross section, since plaster of Paris and bone exhibit similar, but not the same, coherent scatter angular distributions.

For calibration purposes, a set of plaster of Paris phantoms was made with a range of cadmium concentrations with dimensions that reflected the bone at the site of measurement. Actually, circular cylindrical geometry was used to simulate the bone since bone shafts and limbs are usually elliptical in cross section. This geometry was believed to be more representative than the systems of rectangles and squares, as used by Todd *et al.*, (1991) and Wallace, (1994). The phantom geometry can be seen in figure 3.1.

However, before sets of plaster of Paris phantoms were created, water phantoms were made and investigated to test the initial feasibility of a cadmium measurement system. Two different phantom containers held the water phantoms. Nalgene containers (125 ml, 4.8 cm diameter, 9.5 cm high polyethylene bottle) and Falcon tubes (50 ml, 3.0 cm diameter, 11.5 cm high polyethylene tube). The phantom containers were filled with varying cadmium solution concentrations and the two different holders investigated.

These bottles were placed at various distances and then subjected to irradiation. By measuring the flux of photons produced in each of the containers it was decided that the falcon tubes provided less attenuation than the Nalgene containers and were therefore used for optimal phantom holder configuration.

For the water phantom preparation, first several stock solutions of 0.15 M nitric acid were made by diluting 2.5 ml  $\text{HNO}_3$  (15M) in 247.5 ml distilled water in 250 ml volumetric

flasks. Then a cadmium standard solution (1 mg/ml) was made. From these solutions, phantoms of varying cadmium concentrations were made *e.g.* For the 40 ppm phantom, 4 mg (4 ml) of the cadmium stock solution (1 mg/ml) was pipetted into a sterile measuring cylinder, which was then topped up to 100 ml using the nitric acid stock solution.

For the solid bone phantoms, plaster of Paris was used as a substrate to which fixed amounts of cadmium nitrate was introduced. It was a good material to be used as a substrate because known amounts of cadmium chloride dissolved in nitric acid (0.15 M HNO<sub>3</sub>) could easily be made.

Actually, plaster of Paris is usually formed from the hydration of anhydrous calcium sulphate.



To achieve homogeneity of the cadmium throughout the phantom, the mixture was then stirred with a glass rod. The time allowed for mixing was restricted to approximately 40 seconds, as the mixture would begin to solidify very quickly after this time interval. The phantom became warm, as this chemical reaction was exothermic. Afterwards the plaster of Paris phantoms were left to cool, over a period of a night before subjecting them to irradiation.

### 3.3.2 Phantom measurements

However, it was necessary to include a soft tissue phantom material overlying the plaster of Paris. Hence wax was used as the soft tissue phantom material in simulating overlying tissue in measuring cadmium in the bone. The positioning of phantoms was done manually placing them in the centre of the irradiation. An initial set of experiments using the source-based technique was performed to find the optimal distance by changing the sample to detector distance from 0.5 mm to 100 mm. This resulted in a distance of  $(20.0 \pm 0.5)$  mm being chosen. For all the XRF measurements, the phantoms were placed on a semi-adjustable platform that allowed for the phantom to be moved in the 3 main directions of a Cartesian co-ordinate system, vertically (z-axis), horizontally (x-axis) and laterally (y-axis). To ensure that the phantom and detector were aligned with centre of the beam, before each set of irradiation, the height of the phantom and detector were checked.

For the basic preliminary results there was no set counting time as the counting time varied largely from 10 minutes to 24 hours. Large counting times were permitted because of the relatively long half-life of  $^{109}\text{Cd}$  (462 days). Generally, the larger counting times were used for background determination. However, when the more definitive results were required then a more definite counting interval was adopted. The counting time for each phantom measurement was either 1000s or 2000s live time. This counting time interval is comparable with other research work in the field of elemental toxicology, which is generally 30 minutes.

## Chapter 4

### Analytical Interpretation of the Cadmium Measurement System

#### 4.1 Phantom concerns and reliability

Recall, cadmium *in vivo* accumulates in the kidney, thus the kidney would be the preferred site for an initial *in vivo* measurement of cadmium. But cadmium interferes with the calcium metabolism, hence the cortical or trabecular bone was considered, since these bones represented sites that are superficial and therefore should be easier to measure.

As stated in the previous chapter, simulated bone measurements using phantoms have been analysed. For each of these phantoms, the spectra were collected over 2048 channels, which resulted in full width half maximum (FWHM) that ranged from 8-30 channels depending on the detector system and the geometry used.

The phantoms were tested for any evidence of cadmium and thereby determined to have negligible cadmium contamination. However, there was evidence of barium, most likely, from the calcium sulphate used for the production of the phantoms. Fortunately, this contamination had little effect on the detection limit as the barium  $K_{\alpha}$  X-ray peak (32.1 keV) is well separated from the cadmium  $K_{\alpha}$  X-ray peaks. This barium peak, located at channel 679, can be seen in figure 4.3.

Generally, for the source-based analysis of heavier elements *e.g.* lead and mercury investigations, the coherent normalisation procedure is commonly used (O'Meara *et al.*, 1997, 1998). As any differences in the irradiation parameters and the geometry are eliminated by normalisation to the coherently scattered peak. This normalisation procedure has been reported to render the measurement accuracy independent of tissue overlay thickness, bone shape, size, mass and subject motion (Laird, 1983, Somervaille *et al.*, 1985, Chettle *et al.*, 1991, McNeill *et al.*, 1999).

Ultimately, this normalisation procedure improves the transportability of the complete measurement system. Since normalisation is effectively a ratio of peaks, if the positioning of the phantom is changed, then both peaks would be affected primarily by the same factor, however the ratio of the peaks should remain the same, thus negating the problem associated with the positioning, subjectivity and transportability. Hence, this technique could lead to an improvement of the cadmium *in vivo* source-based measurement XRF system. However, the use of the coherent normalisation procedure may be questionable for this lower atomic number element, since the cadmium peaks lay on the other side of the Compton peak and may therefore be subjected to other additional design factors.

Alternatively, the indium to cadmium peak was considered, because it constitutes a ratio of distinct elemental peaks, which could be used for normalisation. Unfortunately, there was no apparent consistent ratio, hence this ratio proved futile. The silver to cadmium peak ratio was also considered with similar findings.

Differences in the peak ratios *e.g.* indium to cadmium could arise from the inhomogeneity of the phantom; that is, if the cadmium inside of the phantom was not distributed evenly, then variations in the geometry of the phantom measurement would result in peak ratio differences. Therefore, the phantoms were tested for homogeneity by the clockwise rotation of the 144 ppm Cd phantom in 90° intervals, these measurements were observed as shown in figure 4.1.

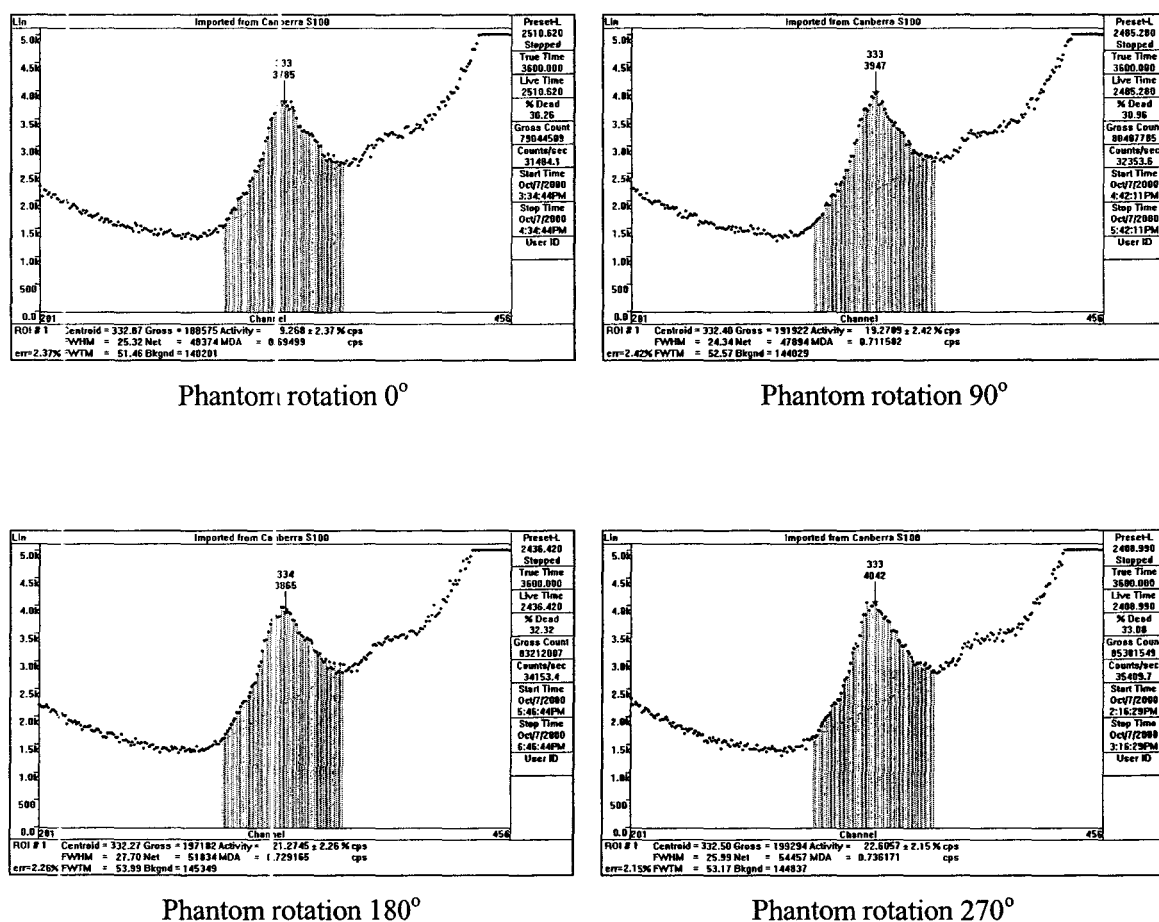
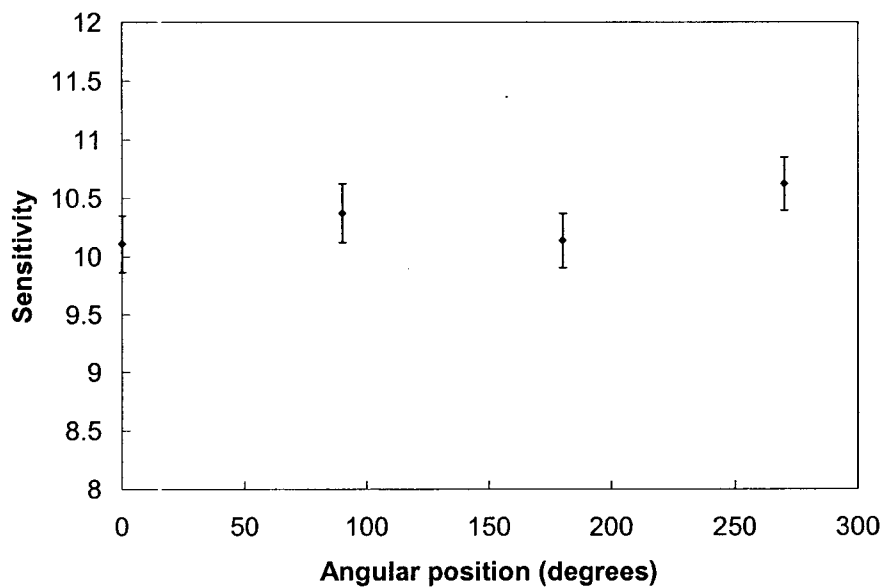


Figure 4.1: The spectra accumulated when the 144 ppm Cd phantom was rotated in 90° intervals in order to test the phantom homogeneity.

By considering the pulse height distributions, for the different rotational geometries, figure 4.1 showed no substantial evidence of any significant fluctuations. Furthermore, when the system sensitivity was investigated, the signal to noise ratio varied by  $\sim 5\%$  as the phantom was rotated through  $0^\circ - 270^\circ$ .



**Figure 4.2: Sensitivity as a function of phantom angular position. It is clear that there is not much effect overall, therefore confirming that the cadmium-doped phantom is fairly homogeneous.**

Figure 4.2 illustrates the effect of phantom rotation on the system sensitivity. The system sensitivity was determined by using the relationship:

$$Sensitivity = \frac{Signal}{\sqrt{Bkgd}} \quad (4.1)$$

From this figure, it is evident that there is little change in the sensitivity; hence, it is not likely that the cadmium in the phantoms was unevenly distributed. However, where the cadmium concentration levels were made with less than 1 ml of stock solution, as was the case with the smaller doped phantoms, it is possible that the cadmium inside of the phantom may be poorly distributed. Thus, changes in the positioning could produce significant fluctuations in the peak heights. Any minor discrepancies in the observed measured spectra could be accounted for, by realising that the spectra ultimately arose from X-rays, which were random by nature, as they entered the detector. This means that there existed a statistical factor that could have affected the experiment reproducibility. In addition, the repeatability of positioning the phantom to exactly the same original site was somewhat questionable.

## 4.2 Optimisation of the system parameters

A typical spectrum obtained from a germanium (Ge) detector is shown in figure 4.3. The cadmium and indium alpha peaks can be seen at channel numbers 477 and 500, corresponding to energies 23.11 keV and 24.14 keV respectively. The beta peaks are also visible at channels 540 and 564. The most prominent cadmium peak located at 23.11 keV is a doublet, comprising the cadmium  $K_{\alpha 1}$  and cadmium  $K_{\alpha 2}$  peaks. However, the most distinct spectral peak of the plaster of Paris sample was produced because of the presence of indium, as this element is inherent to the germanium detector used, and becomes more pronounced with increasing sample density.

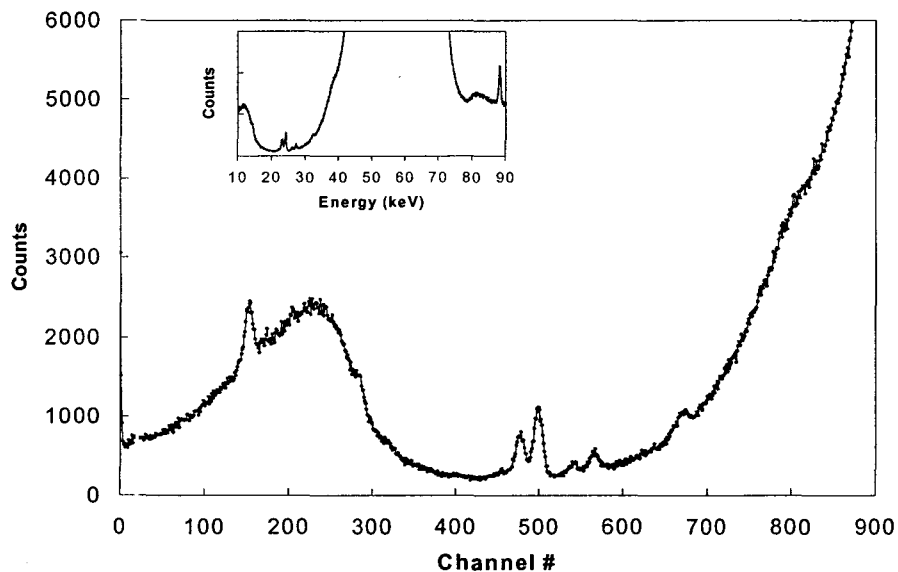


**Figure 4.3: Summed spectrum from a Ge detector for a 170 ppm Cd of bone phantom, counted for 2000s live time. The full energy spectrum of the incident photons as detected by the Ge detector is shown in the insertion.**

In figure 4.3, the peaks of interest are clearly noticeable, as they occur in the minimum background region. Note the behaviour of the background is governed by the response of the HPGe detector in the monitored energy range. This detected spectrum was associated with the  $^{109}\text{Cd}$ -bone measurement system using a  $180^\circ$  geometry. When the region of interest is expanded, the coherent scattered peak becomes visible and occurs at 88.035 keV. It is also evident from the figure that there is some escape of photon energy from the germanium crystal, but this occurs at lower energies and represents a small fraction of the total spectrum. In this spectrum, there also exists a copper peak, which is prevalent at channel 140 corresponding to an energy between 8.028 and 8.048 keV. The peak occurs because the  $^{109}\text{Cd}$  source is encapsulated in a collimator, which has a copper filter to prevent backscatter. An increase in backscatter would increase the background signal that is definitely not warranted. There is also a barium peak that is seen on the rising edge of the asymmetric Compton peak. This peak does not affect the system sensitivity, as it has too high an energy. In the germanium detector spectrum, the cadmium K X-ray peaks are observed within the 22.5 keV to 27.0 keV range. Table 2.1 showed the energy of these cadmium peaks. Many X-rays are emitted from each heavy metal, but only five of them are of great concern (mainly the  $K_{\alpha 1}$ ,  $K_{\alpha 2}$ ,  $K_{\beta 1}$ ,  $K_{\beta 2}$  and the  $K_{\beta 3}$  X-rays), as the other X-rays have intensities that are too small to be considered. The table 4.1 shows the energies for the above mentioned spectral peaks.

**Table 4.1: Shows the observed peak energy with the corresponding channel numbers for the experimental gain used. K X-ray energies taken from Lederer & Shirley, 1978.**

Element	K <sub>α1</sub> peak energy (keV)	K <sub>α2</sub> peak energy (keV)	Visible <peak> Ch #	K <sub>β1</sub> peak energy (keV)	K <sub>β2</sub> peak energy (keV)	K <sub>β3</sub> peak energy (keV)	Visible <peak> Ch #
Silver	22.16	21.99	464	24.93	25.46	24.91	—
Cadmium	23.17	22.98	477	26.09	26.64	26.06	549
Indium	24.21	24.00	500	27.27	27.86	27.24	564
Barium	32.19	31.82	679	36.38	37.26	36.30	—

— There was no definite observable peak.

From this table, it is possible for the gain of the system to be estimated. Based on the above figures in the table, the actual gain used was 48.3 eV/Ch. This estimate of gain was quite consistent with the actual gain used. The gain setting employed, as stated on the Ortec (model 572), for the 170 ppm cadmium spectrum was 50 eV/Ch.

When different detector systems are to be compared many factors must be considered *e.g.* the sensitivity, the gain, the efficiency and the resolution, as these fundamental parameters can significantly affect the feasibility of a system. So the spectra for the different detectors were collected for analysis. The resolution of the Princeton Gamma Tech. NIGP 2020, model RG 158/C detector operating with gain of 70 eV/Ch, for 900 seconds was poor. The full widths varied from  $10.3 \pm 1.2$  channels to  $36.5 \pm 4.3$  channels ( $0.715 \pm 0.086$  keV to  $2.55 \text{ keV} \pm 0.31$  keV) for the FWHM and the FWTM respectively. Whereas the GL2020R detector operating with gain of 48.3 eV/Ch, for 2000 seconds was considerably better with full widths that varied from  $9.8 \pm 0.6$  channels to  $17.9 \pm 1.2$  channels. The pulse height distributions of both systems are shown in figure 4.4 and figure 4.5.

It is clearly seen that using the Ge Canberra system improved the system resolution. This superior resolution of the GL2020R resulted in fairly defined and separated peaks. In addition, since the system was operated with a gain 48.3 eV/Ch, it placed the X-rays in higher energy bins causing the spectral peak heights to appear at higher channels.

Alternatively, assessing the effect of the additional peaks in the spectra can compare detector systems. This can be achieved by converting all the signals in each spectrum to an effective  $K_{\alpha 1}$  signal, through the ratios of peak areas, and then taking the inverse variance weighted mean  $K_{\alpha 1}$  peak area for each detector.

From theory, for the optimal recording of results the system requires good throughput *i.e.* high number of counts in peaks and a small FWHM. Also, a smaller system shaping time is desired, as this results in smaller dead time, hence an increase the number of counts for a given true time. The gain of the amplifier is also an important parameter, which should have a reasonable value. By the careful selection of gain the spectrum produced can effectively extend to the full range of available channels. The bad choice of gain can result in spectra that are too small, using very little of the available channels, so that the peaks do not get separated sufficiently. Conversely, too high a gain can result in spectral shifts, which cannot be collected within the given channel range of the proprietary software.

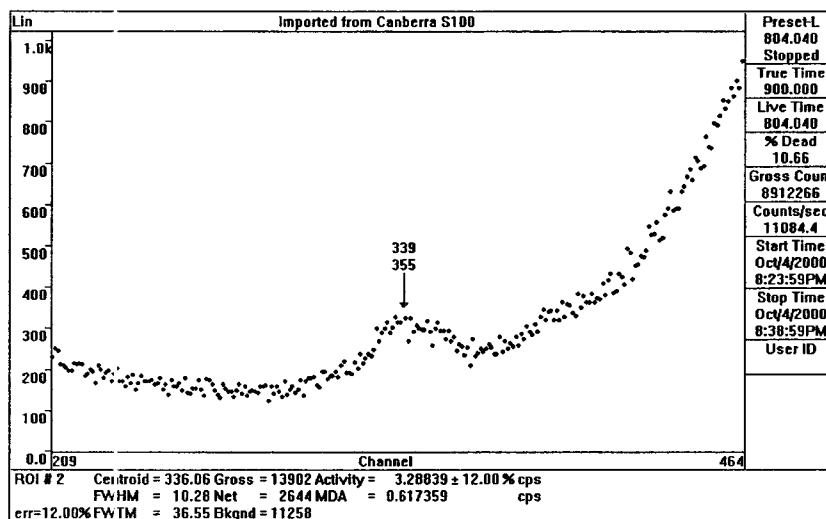


Figure 4.4: Spectrum of a blank tube phantom (0 ppm) placed at a sample to detector distance 40 mm away. Polarised system was used with the Princeton double-headed gamma detector.

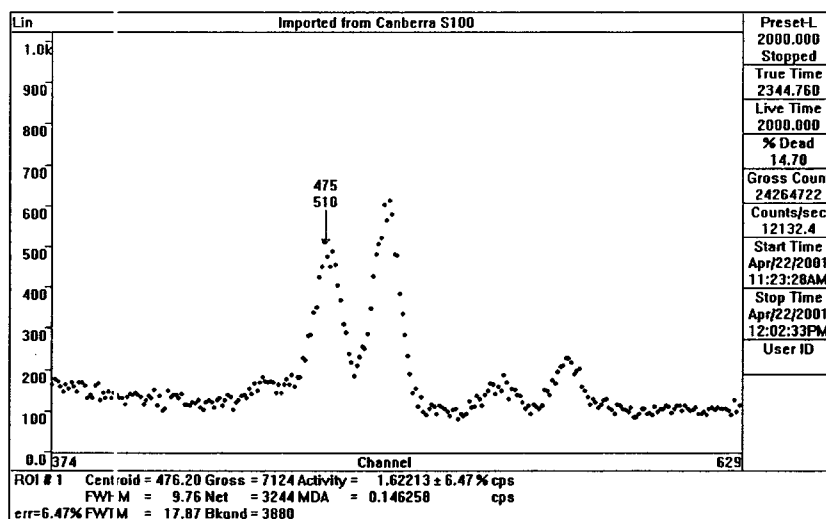


Figure 4.5: Spectrum of the 40 ppm distilled water phantom placed at a sample to detector distance 20 mm away. Polarised system was used with the Ge Canberra, model GL2020R.

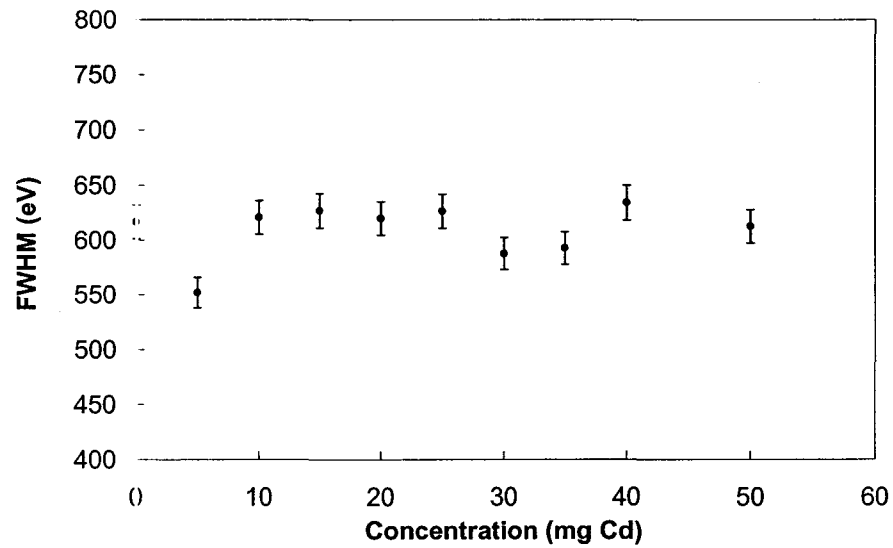


Figure 4.6: Illustrates the FWHM of the Ge GL2020R detector system when the cadmium series line was analysed using polarised XRF.

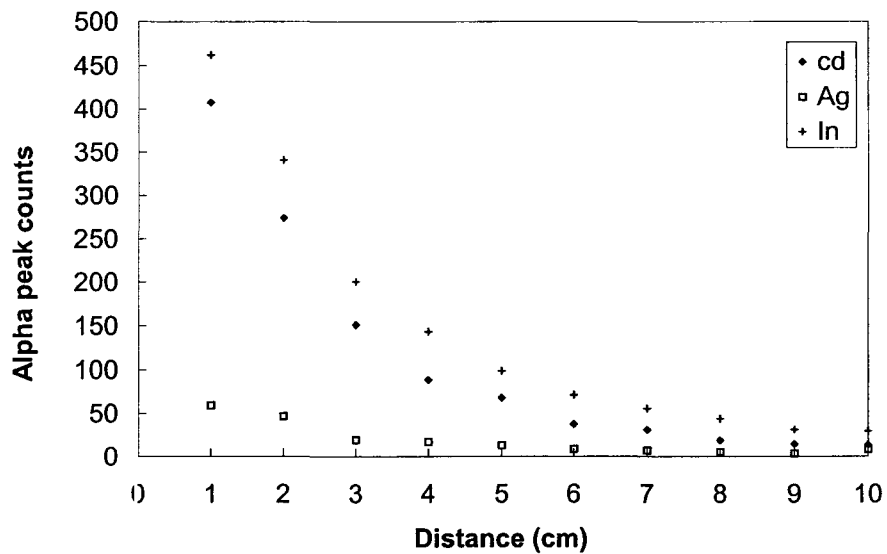


Figure 4.7: Demonstrates the spatial distribution of the observed alpha peak counts with increasing distance between the source and the sample.

Actually, peak separation is resolution dependent that is fundamentally related to the FWHM by the following equation:

$$R = \frac{FWHM}{H} \quad (4.2)$$

where  $R$  is the detector energy resolution,  $H$  is a function of the number of charge carriers  $f(N)$  generated by the detector system (which should be constant for a given fixed photon energy).

Therefore, for a given number of charge carriers, the resolution of the system is proportional to FWHM. In figure 4.6, it can be clearly seen that the FWHM remained constant as the cadmium concentration of the phantom increased. So it can be inferred that the detector energy resolution is not affected by the phantom sample concentration.

In reducing the dead time of the system, the throughput is commonly compromised; hence some trade off between the two parameters must be established for system optimisation. Thus, by the variation of the source to sample distance, this optimal requirement can be achieved. Theoretically, the incident photon fluence on the phantom and the characteristic X-rays entering the detector depends on the distance between the source and sample. Thus, the effect of this positioning was investigated.

Actually, as the distance from the source to the bone phantom ( $r$ ) is increased, the signal reaching the bone is reduced by a factor of  $1/r^2$ . Thus, the results obtained in figure 4.7 supports the hypothesis that as the distance is increased, the detected X-rays decrease by

the inverse squared distance relation. This relationship was seen for all three elemental peaks.

### **4.3 Optimisation of the polarisation parameters**

For the polarised XRF system, the irradiation beam is primarily dependent on the tube potential and tube current, so these parameters were investigated. Importantly, the choice of voltage for the X-ray tube for heavier metals is usually dependent on the absorption edge of the element being excited, *e.g.* for mercury measurements which has a k-edge of 83.103 keV, compels the polarised X-ray to have an energy greater than 83 keV after polarisation. This implies primary photon energy of more than 99 keV. For example, Börjesson (1996) suggested that the tube voltage had to be more than 160 keV. However, since the K-edge of cadmium is only 26.711 keV, this was not a concern. Thus, the voltage variation was tested for each available voltage.

As the voltage was increased, it could be seen that the throughput, as well the dead time increased. By considering the pulse height distributions in figure 4.8, clearly a voltage of 75 keV was definitely too low, as the gross count throughput was 3099.95 cps with a corresponding alpha peak count of 26.12 cps. However, when the voltage was increased to 125 keV, there was a seven-fold increase in throughput. More importantly, the alpha peak count increased to 123 cps. As with the throughput and the alpha peak counts, the dead time and the FWHM of the spectra also increased. From these pulse height distributions, the dead time was studied, as this factor was a major constraint.

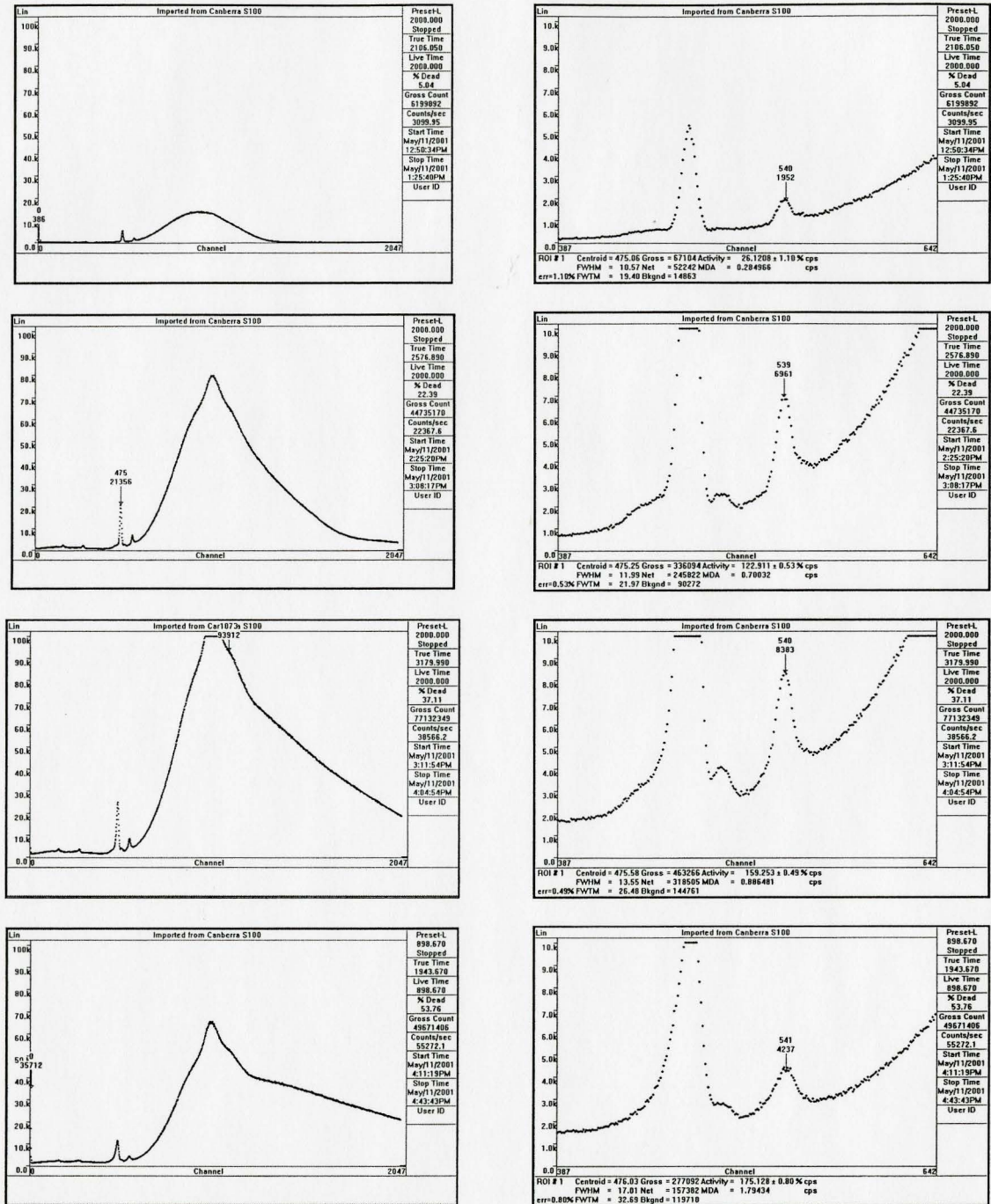


Figure 4.8: Optimisation of X-ray tube operating voltage. The voltage optimisation has been performed on the basis of dead time, FWHM and gross counts for 12 mA current.

For any set of measurements, there exists a maximum limit for dead time. Practically, the proprietary software can handle up to 40% dead time, thereafter the repeatability of the system becomes questionable. It would also create concerns regarding patient irritability and motion due to longer counting times. Figure 4.9 shows the dead time as a function of operation voltage. It can be seen that the dead time increases, as there is an increase in voltage. This monotonic increase is realised with all the orthovoltages used. Thus, the interpretation based on figure 4.9 is that 175 kV would be an optimal operating voltage.

Having selected the operating voltage for optimal performance of the XRF measurement system, the current variation was considered. Measurements were collected and displayed. Figure 4.10 shows the effect of increasing the current in the system. An increase in current means there is a greater number of photons incident on the detector face, which implies an increase in the alpha and beta peaks. So having studied these parameters, it appeared feasible to operate the Philips RT polarising X-ray machine with 12.5 mA at 175 keV.

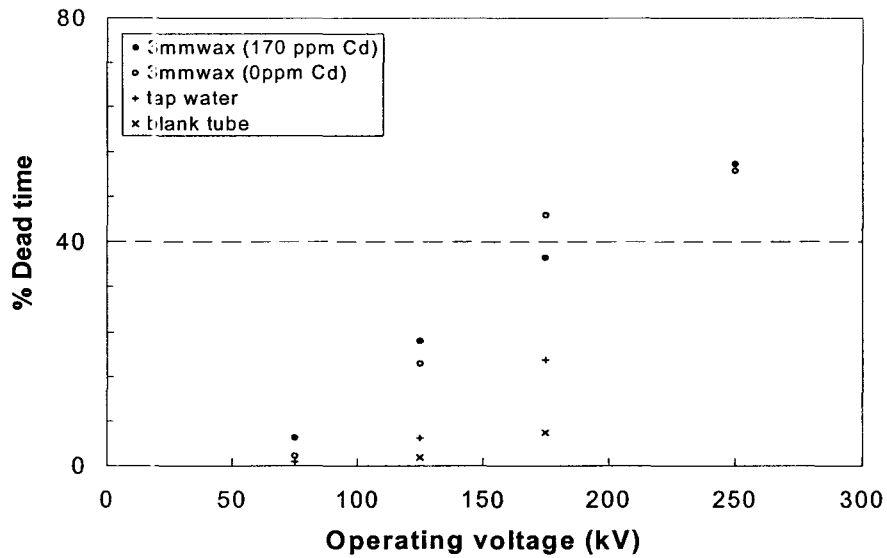


Figure 4.9: Detector dead time response for 4 different samples to increasing voltage.

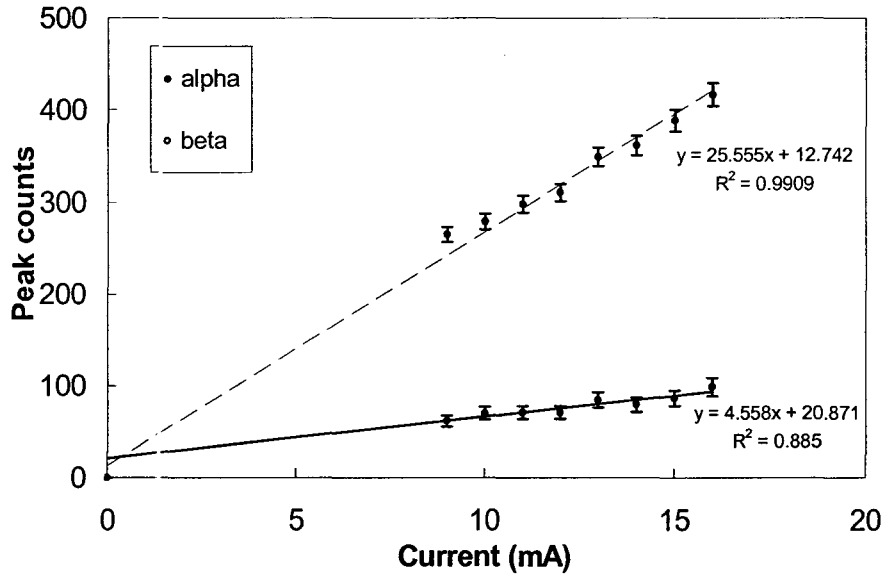


Figure 4.10: Relationship between tube current and the total number of alpha and beta counts when an X-ray machine was operated at 175 keV.

#### 4.4 Levenberg-Marquardt Analysis

Having acquired the spectral data using the commercially available analysis software (Canberra S100), the areas under the gamma ray energy spectrum associated with the concerned photopeak were assessed. From this the concentration in parts per million (ppm) or milligram (mg) cadmium was inferred. The analysis of data was achieved by the use of some robust algorithm. The data were analysed using an analysis code called Marquardt (Bevington, 1992), developed by Birmingham and McMaster Universities. This code is a mathematical model, that is use to fit spectral data by searching the reduced  $\chi^2$  space to find the minimum deviated fit. It uses the method of non-linear least squares to obtain a good fit. Mathematically, the goodness of fit,  $\chi^2$ , can be determined by the use of the following equation (Bevington, 1992):

$$\chi^2 \equiv \sum \left\{ \frac{1}{\sigma_i^2} [y_i - y(x_i)]^2 \right\} \quad (4.3)$$

where the  $\sigma_i$  are the uncertainties in the data points  $y_i$ .

In the Marquardt method of analysis, the mathematics of the fitting program is amended to suit the peaks being modelled. This facilitates the fitting of the different spectral peaks.

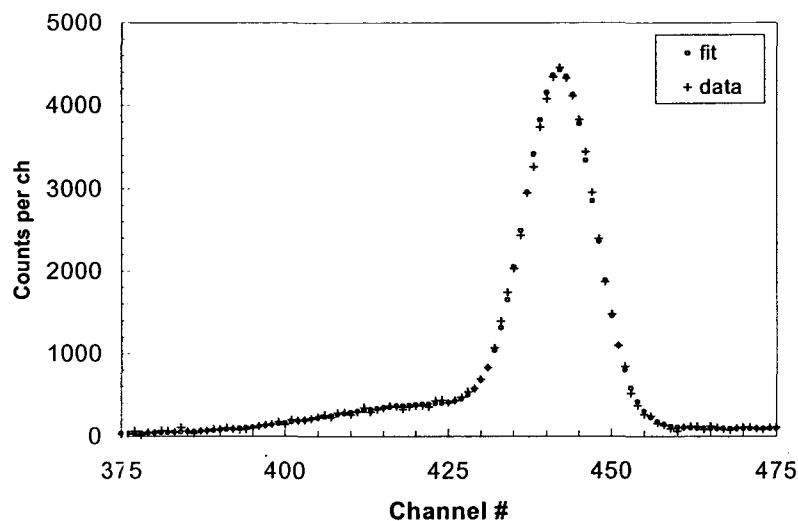


**Figure 4.11: Initial Marquardt fit to spectral data observed for 50 mg cadmium phantom. The selected region of interest is taken as the region between 375 to 475 channels. This pulse height distribution was obtained by running a Marquardt modeling program created to account for the necessary observed peak.**

Unfortunately, negative peak amplitudes, which are very misleading, can often be determined for the low concentration phantom. This can be somewhat confusing since it obviously, cannot be the case. These negative results can occur because of the inherent statistical processes associated with radiation detection and measurement. The magnitude of the spectral background under a X-ray peak is usually predicted from regions on both sides of the peak. Because of the statistical uncertainty in each spectrum channel, at low concentrations, the integrated signal in the region of the peak can be less than the predicted background size creating the occurrence of negative X-ray intensities (McNeill, 1998). Conversely, contamination in the calibration standards could create a positive intercept on calibration lines.

**Table 4.2: Displays the results as determined for different concentration phantoms by Marquardt analysis program.**

Conc <sup>n</sup>	5	10	15	20	25	30	35	40	50
Tail amp	34.75	96.63	150.48	137.57	200.49	199.25	244.54	297.59	327.66
Tail pos	425.36	426.30	425.08	421.26	422.81	421.93	422.60	425.68	422.41
Tail width	19.98	21.93	24.65	19.04	21.98	21.86	21.43	24.61	21.42
Cd amp	374.35	670.85	983.48	1278.00	1666.60	1818.80	2091.60	2402.70	2923.20
Cd pos	443.27	443.30	443.36	443.18	443.22	443.22	443.25	443.27	443.24
Cd width	6.97	7.00	6.95	7.06	7.04	6.96	6.95	6.92	7.01
Area ratio	0.27	0.45	0.54	0.29	0.38	0.34	0.36	0.44	0.34

Note that the zero concentration phantom was omitted from this table because its results were mitigated because of the tail feature of the spectrum.

For a given detector system the full width half maximum is a constant for any given peak. Therefore, the height of the peak could be used as a measure of the total peak area. Thus, amplitudes and uncertainties derived from the Marquardt fit were used to construct a calibration curve of peak amplitude verses cadmium concentration.

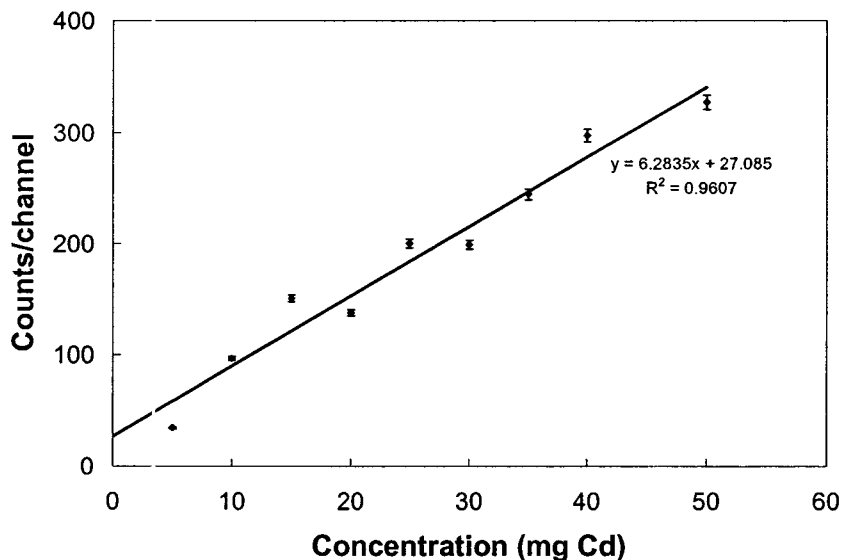


**Figure 4.12: Shows an alpha peak calibration curve. This is a plot of tail amplitude versus cadmium concentration when an exponential function was used to model the background.**

Both figure 4.12 and table 4.2 show that the tail was affected by cadmium content, as its amplitude increased with increased cadmium concentration. Further investigations showed that the tailing of the peak was associated with the initial electronic set up, hence by observing the signal sent to the oscilloscope screen, the electronics of the system was studied. It was found that the pole zero was not aligned. The inaccurate pole zero positioning resulted in dubious analysis, as this parameter affected the peaks. Spectral distortion was distinct as tailing was pronounced. Thus, in the vicinity of the main peak being measured, the nearby smaller peaks were obscured. Hence by adjusting this parameter the tailing factor was alleviated.

Actually, detector system installation plays a critical role in the implementation of a reasonably good design. For a successful and ultimately, very promising system, the initialisation of the electronic components must be adjusted to optimise their performance. The wiring of the system must be flawless to ensure no loss of signal caused by the leaking of current or increased wire resistance, as this would cause an increase in noise. These problems could lead to a decrease in the signal to noise ratio and thus result in poorly defined peaks, as the background would be greater.

In retrospect, when further analysis was done with the Princeton HPGe detector, it was realised that the cadmium peak height was insignificant over the background, so it was replaced with the GL2020R detector, which resulted in improved sensitivity. The GL2020R HPGe detector had better resolution, which led to well-separated cadmium, silver and indium peaks, and therefore, a well-defined fitting technique. It should be noted that despite the achievement of superior HPGe resolution, an improvement in the

minimum detectable limit would only occur, if the fitting of the clearly defined cadmium peak with the Marquardt method, improved the uncertainty on the peak height. The following section would serve as a brief explanation, though definitely not exhaustive, of how peaks are modelled using this program.

#### **4.5 Spectral Analysis**

Primarily, background spectral shapes were modelled by the use of single or double exponential functions. Gaussian functions to model characteristic peaks have been widely used for justifiable fits to this type of spectral data (Pejović-Milić, 1998; Arnold, 2001). To understand the principle pertaining to this algorithm consider figure 4.13. The resulting spectrum was analysed using a multi-peak model to determine the various elemental intensities. These peaks were modelled by Gaussians of variable amplitude on a double exponential background, from 21.5 keV to 27.5 keV (corresponding to channels from 440 to 580).

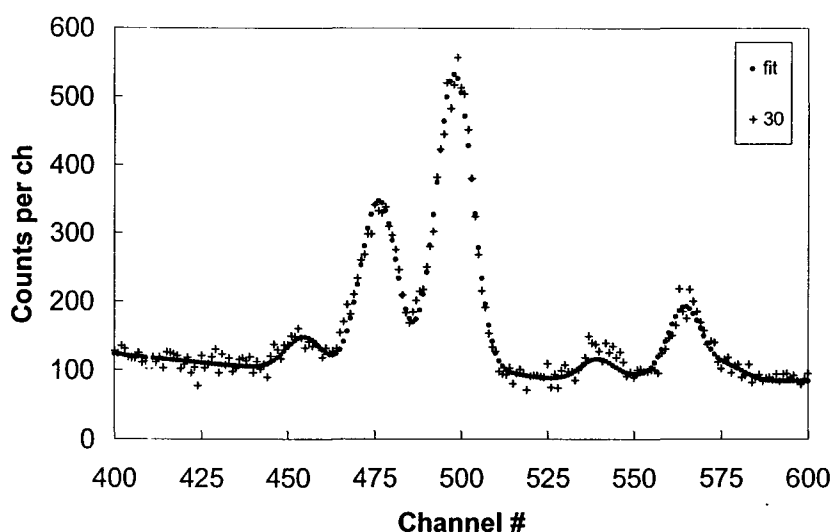


**Figure 4.13: Marquardt 11-parameter fit to spectral data (30 ppm water phantom). There is the occurrence of alpha and beta multiple peaks. However, these resulting multiplets in the spectrum could not be resolved visually, as the X-ray energy difference of the peaks *e.g.*  $K_{\alpha 1}$  and  $K_{\alpha 2}$  peaks, were less than the FWHM of the system.**

For the spectral analysis separate fits were applied to the silver, cadmium and indium characteristic peaks. The summed spectrum was analysed over 200 channels. Likewise, the other acquired spectra were also summed over 200 channels. Initially, a Gaussian was used to model each peak present. The peaks for consideration were the silver  $K_{\alpha}$  and  $K_{\beta}$  peaks, cadmium  $K_{\alpha}$  and  $K_{\beta}$  peaks and the indium  $K_{\alpha}$  and  $K_{\beta}$  peaks. This fit resulted in a 12-parameter model. However, if there was any evidence of a rising tail, then more parameters were needed to model the tail adequately. These additional parameters resulted in a 15-parameter model. The mathematical function was too complex, and thus is not quoted here.

However, since the silver beta peaks were so small, these beta peaks were tied to the silver alpha peaks, thus reducing the parameters to eleven. With this 11-parameter model different background fits were formulated and studied *e.g.* constant, linear, linear-quadratic, parabolic, single exponential and double exponential. Based on different analytical interpretations of the mentioned fits, the exponential fits continued to surpass the other fitting background models, by producing more consistent and reliable information. And so these were chosen over the other fitting background models. Comparisons of the area ratios, precision improvement, value of the chi square, statistical deviations of the determined peak amplitude and the ability of the modelling program to run adequately without error were the main criteria for the selection of the fitting background.

Ultimately, it was determined that a single exponential fit for background was only good when analysing the water type phantoms, therefore in all spectra, a double exponential fit was used. Therefore the following 11-parameter, double exponential fit was used in analysing the cadmium peak area for most of the initially acquired spectra.

$$\begin{aligned}
y(x) = & A_1 e^{-\frac{(x-A_0)^2}{A_1}} + k_1 A_1 e^{-\frac{(x-A_0-k_2)^2}{A_1}} + A_2 e^{-\frac{(x-A_0-k_3)^2}{A_1}} + k_4 A_2 e^{-\frac{(x-A_0-k_5)^2}{A_1}} + A_3 e^{-\frac{(x-A_0+k_6)^2}{A_1}} + \\
& k_7 A_3 e^{-\frac{(x-A_0+k_8)^2}{A_1}} + k_9 A_2 e^{-\frac{(x-A_0+k_{10})^2}{A_1}} + k_{11} k_9 A_2 e^{-\frac{(x-A_0+k_{12})^2}{A_1}} + A_4 e^{-\frac{(x-A_0+k_{13})^2}{A_1}} + \\
& k_{14} A_4 e^{-\frac{(x-A_0-k_{15})^2}{A_1}} + k_{16} A_4 e^{-\frac{(x-A_0-k_{17})^2}{A_1}} + A_5 e^{-\frac{(x-A_0-k_{18})^2}{A_1}} + k_{19} A_5 e^{-\frac{(x-A_0+k_{20})^2}{A_1}} + \\
& A_6 e^{A_7 x} + A_8 e^{A_9 x}
\end{aligned} \tag{4.4}$$

where the  $k$ 's are constant parameters provided to the program.

$$k_1 = 0.532, k_2 = 4.03191, k_3 = 21.5038, k_4 = 0.53, k_5 = 25.1766, k_6 = 22.04468,$$

$$k_7 = 0.533, k_8 = 7.62553, k_9 = 0.211111, k_{10} = 37.37021, k_{11} = 0.1831502, k_{12} = 48.64681,$$

$$k_{13} = 62.15745, k_{14} = 0.51865, k_{15} = 61.41277, k_{16} = 0.2575, k_{17} = 73.8383,$$

$$k_{18} = 87.15745, k_{19} = 0.1942446, k_{20} = 99.71064$$

These constant parameters are based on the peak position and peak intensity of the associated elemental peak, since the positions and amplitudes of the X-rays in each section were linked according to their tabulated energies and relative intensities.

while  $A_1$  is the amplitude of the cadmium alpha peak,

$A_2$  is the amplitude of the silver alpha peak,

$A_3$  is the amplitude of the indium alpha peak,

$A_4$  is the amplitude of the cadmium beta peak,

$A_5$  is the amplitude of the indium beta peak,

$A_6$  and  $A_7$  are constants for the first exponential background,

$A_8$  and  $A_9$  are constants for the second exponential background,

$A_{10}$  is the cadmium alpha peak position,

$A_{11}$  is the alpha peak width.

The independent variable,  $x$ , and dependent variable,  $y$ , have been used in the same manner throughout this section. Where  $x$  represents the channel number in the spectrum, while  $y$  is the number of counts in the corresponding channel.

Usually, to get a better fit and to increase the degrees of freedom of the model, it is necessary to fit over the maximum possible number of channels. However, other spectral features appear at higher and lower energies. Thus, these would also require modelling, thereby potentially increasing the number of fitting parameters. Therefore, only 200 channels were fitted, as was appropriate, around the characteristic peak, so that no other spectral features were included.

Parameter reduction was considered since less parameters in the Marquardt model is much more preferred as this leads to better accuracy of the low X-ray intensities, because of an increase in the degrees of freedom. Thus, in an attempt to reduce the number of parameters, the question of tying 'the silver or the indium' alpha peak amplitudes to the cadmium was addressed. But this was ruled out for two reasons. First, if a method of normalisation were required, then the tying of such a parameter could render normalisation futile. Secondly, when the peak amplitudes were compared, no relevant correlation existed between the cadmium to indium and the cadmium to silver peak ratios.

The indium peak in the spectrum arises because there is indium inherent in the detector, which therefore becomes subjected to the gamma ray excitation. However, the silver peaks may arise from the coherent scatter of the sample phantom or from the source

shield, as photons that hit this shield are reflected off of it and into the detector face and hence crystal. These processes result in characteristic X-rays that are in close proximity to the cadmium peak energy.

For parameter reduction, it was decided to assess the width of Gaussian peaks. Figure 4.14 illustrates the variation in the peak width. From this figure, it is clearly seen that there exists little variation in the peak width when the concentration is increased, thus this supports the idea for fixing the peak width. However, from this figure it appears that the increase in the tissue overlay may have significant effect. Hence this was also investigated.

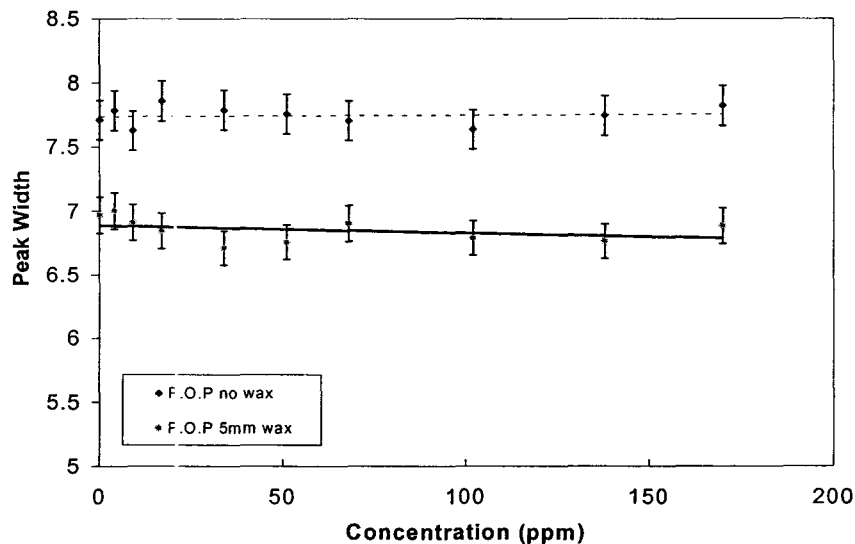


**Figure 4.14: Peak width variation for the plaster of Paris with no tissue overlay and with 5 mm artificial tissue.**

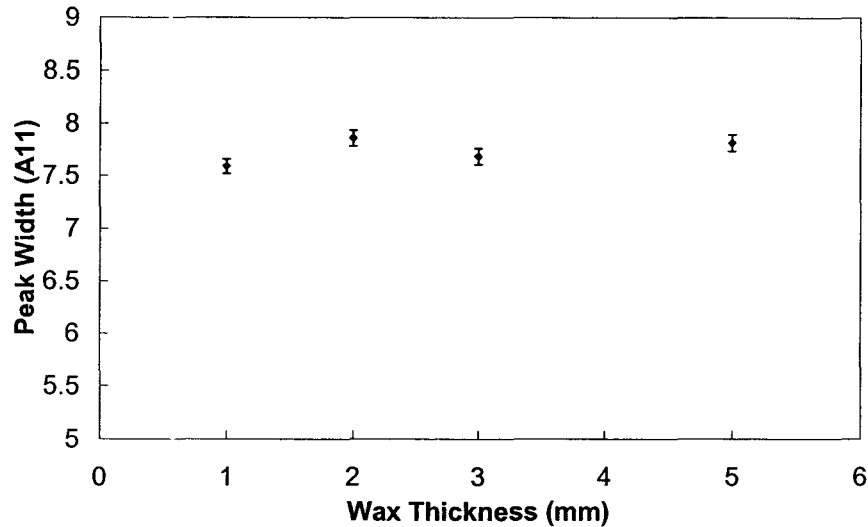


**Figure 4.15: Thickness variation. The results showed little dependence on overlaying phantom tissue.**

Figure 4.15 shows the peak width variation with the wax thickness. However, figure 4.15 does not appear to exhibit any significant variation to claim that the peak width was varying with the increase in wax overlay. Thus, an inverse variance weighted mean of the widths given by the analysis of the different concentration phantom spectra was used for the fixed value for all subsequent analysis.

Therefore the fitting equation became

$$\begin{aligned}
 y(x) = & A_1 e^{-\left(\frac{x-A_{10}}{w}\right)^2} + k_1 A_1 e^{-\left(\frac{x-A_{10}-k_2}{w}\right)^2} + A_2 e^{-\left(\frac{x-A_{10}-k_3}{w}\right)^2} + k_4 A_2 e^{-\left(\frac{x-A_{10}-k_5}{w}\right)^2} + A_3 e^{-\left(\frac{x-A_{10}+k_6}{w}\right)^2} + \\
 & k_7 A_3 e^{-\left(\frac{x-A_{10}+k_8}{w}\right)^2} + k_9 A_2 e^{-\left(\frac{x-A_{10}+k_{10}}{w}\right)^2} + k_{11} k_9 A_2 e^{-\left(\frac{x-A_{10}+k_{12}}{w}\right)^2} + A_4 e^{-\left(\frac{x-A_{10}+k_{13}}{w}\right)^2} + \\
 & k_{14} A_4 e^{-\left(\frac{x-A_{10}-k_{15}}{w}\right)^2} + k_{16} A_4 e^{-\left(\frac{x-A_{10}-k_{17}}{w}\right)^2} + A_5 e^{-\left(\frac{x-A_{10}-k_{18}}{w}\right)^2} + k_{19} A_5 e^{-\left(\frac{x-A_{10}+k_{20}}{w}\right)^2} + \\
 & A_6 e^{A_7 x} + A_8 e^{A_9 x}
 \end{aligned} \tag{4.5}$$

where the parametric variables are the same as stated in equation 4.4.

while  $A_1$  is the amplitude of the cadmium alpha peak,

$A_2$  is the amplitude of the silver alpha peak,

$A_3$  is the amplitude of the indium alpha peak,

$A_4$  is the amplitude of the cadmium beta peak,

$A_5$  is the amplitude of the indium beta peak,

$A_6$  and  $A_7$  are constants for the first exponential background,

$A_8$  and  $A_9$  are constants for the second exponential background,

$A_{10}$  is the cadmium alpha peak position.

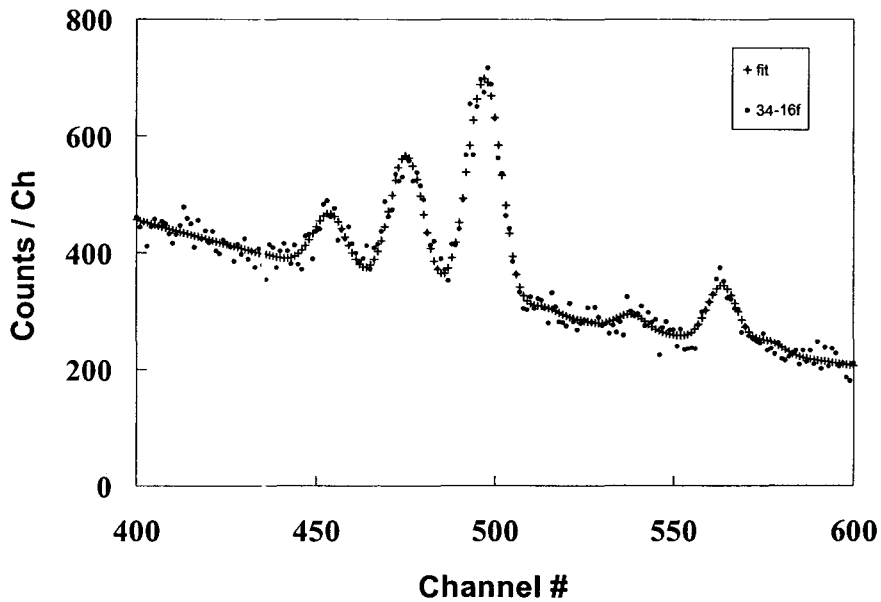


**Figure 4.16: 10-parameter Marquardt fit to spectral data (34 ppm plaster of Paris phantom) using a 1.6 mm external copper filter.**

Figure 4.16 shows the rigor of this 10-parameter fit. This fit illustrates that the modelled program was definitely appropriate as the difference between the fit and spectral data was minimal. This fit was similar, but different than the 11-parameter fit, since the floating peak width was now fixed at a nominal value of 5.898. Fitting the spectral data with the 10-parameter fit allowed for more precision. The improvement in the precision can be seen in table 4.3. For each set of measurement analysis with this fit, the resulting mean reduced chi-square was within one standard deviation of unity indicating that the modelling program was adequate. ( $p < 0.5$ ) was obtained for 190 degrees of freedom for the given chi squares.

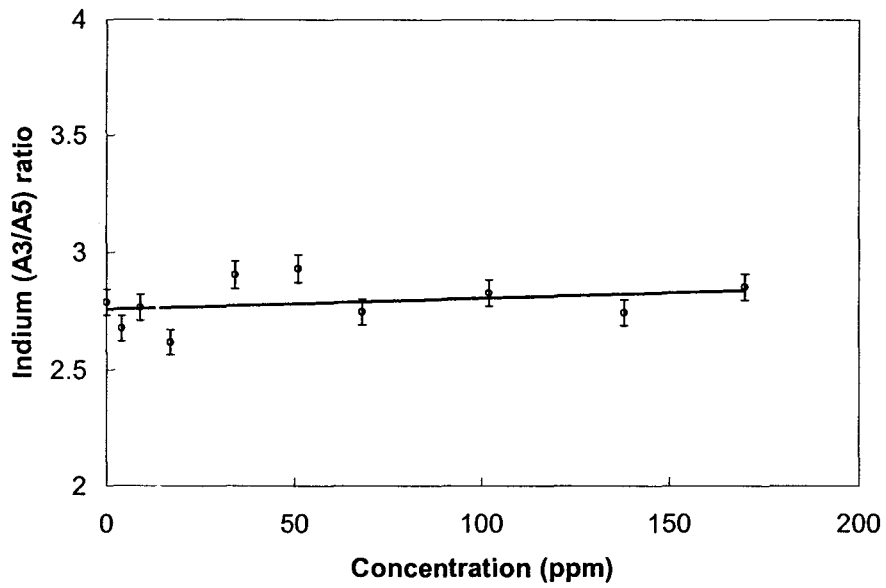


Figure 4.17: Indium ratio for the plaster of Paris line in 5 mm wax.

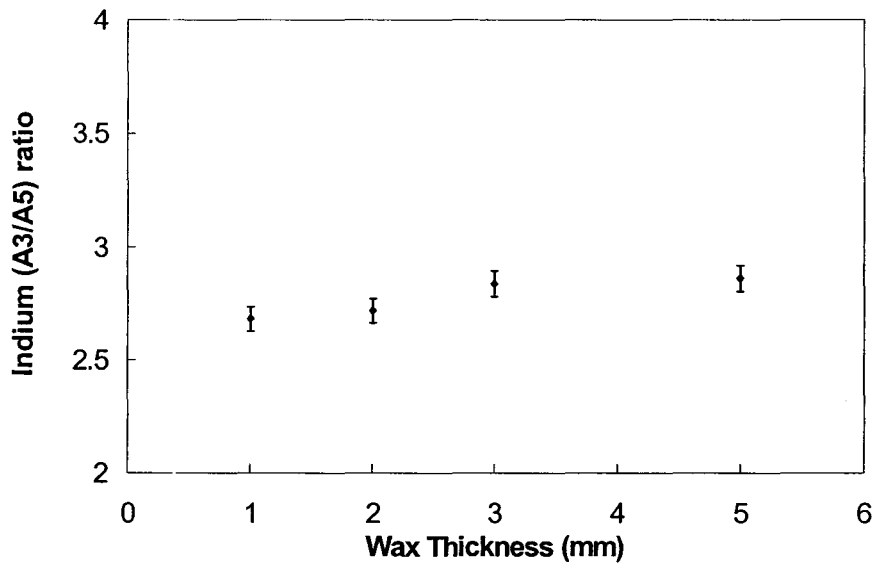


Figure 4.18: Indium ratio for different wax thickness.

For further reduction of these parameters, the indium alpha to beta peak ratio was studied. This ratio is seen in figure 4.17. From this figure, it is evident that there existed little fluctuation in the indium ratio, as the concentration is increased. Thus, this supported the idea of tying the alpha peak to the beta peak. However, before this was implemented, the effect of tissue overlay was investigated. Consequently, the addition of wax overlay resulted in no overwhelming deviations. The indium ratio varied little, less than 10%, although it was slightly increasing with increasing concentration, therefore the indium alpha and beta peaks were tied.

As done previously with the peak width parameter, an inverse variance weighted mean of the indium ratios was also determined and used for all subsequent 9-parameter fits. Thus, the final 9-parameter equation selected for fitting the cadmium peak was

$$\begin{aligned}
 y(x) = & A_1 e^{-\left(\frac{x-A_5}{w}\right)^2} + k_1 A_1 e^{-\left(\frac{x-A_5-k_2}{w}\right)^2} + A_2 e^{-\left(\frac{x-A_5-k_3}{w}\right)^2} + k_4 A_2 e^{-\left(\frac{x-A_5-k_5}{w}\right)^2} + A_3 e^{-\left(\frac{x-A_5+k_6}{w}\right)^2} + \\
 & k_7 A_3 e^{-\left(\frac{x-A_5+k_8}{w}\right)^2} + k_9 A_2 e^{-\left(\frac{x-A_5+k_{10}}{w}\right)^2} + k_{11} k_9 A_2 e^{-\left(\frac{x-A_5+k_{12}}{w}\right)^2} + A_4 e^{-\left(\frac{x-A_5+k_{13}}{w}\right)^2} + \\
 & k_{14} A_4 e^{-\left(\frac{x-A_5+k_{15}}{w}\right)^2} + k_{16} A_4 e^{-\left(\frac{x-A_5+k_{17}}{w}\right)^2} + k_{18} A_3 e^{-\left(\frac{x-A_5+k_{19}}{w}\right)^2} + k_{20} k_{18} A_3 e^{-\left(\frac{x-A_5+k_{21}}{w}\right)^2} + \\
 & A_6 e^{A_7 x} + A_8 e^{A_9 x}
 \end{aligned} \tag{4.6}$$

where the  $k$ 's are constant parameters provided to the program as

$$k_1 = 0.532, k_2 = 4.03191, k_3 = 21.5038, k_4 = 0.53, k_5 = 25.1766, k_6 = 22.04468,$$

$$k_7 = 0.533, k_8 = 7.62553, k_9 = 0.21111, k_{10} = 37.37021, k_{11} = 0.1831502,$$

$$k_{12} = 48.64681, k_{13} = 62.15745, k_{14} = 0.2575, k_{15} = 73.8383, k_{16} = 0.51865,$$

$$k_{17} = 61.41277, k_{18} = 0.325760, k_{19} = 87.15745, k_{20} = 0.1942446, k_{21} = 99.71064,$$

$$w = 5.898296$$

where the parameters determined by using Marquardt algorithm were

$A_1$  is the amplitude of the cadmium alpha peak,

$A_2$  is the amplitude of the silver alpha peak,

$A_3$  is the amplitude of the indium alpha peak,

$A_4$  is the amplitude of the cadmium beta peak,

$A_5$  is the cadmium alpha peak position.

$A_6$  and  $A_7$  are constants for the first exponential background,

$A_8$  and  $A_9$  are constants for the second exponential background.

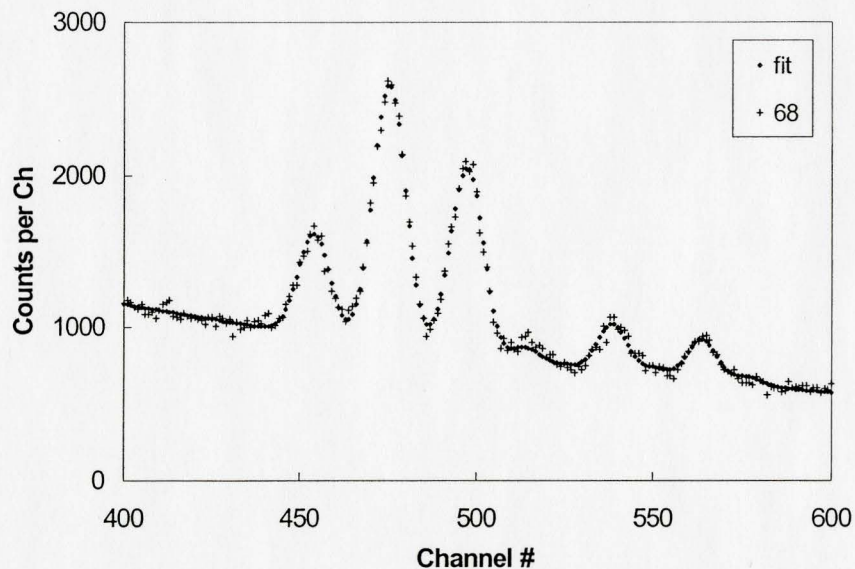


Figure 4.19: 9-parameter Marquardt fit to spectral data (68 ppm plaster of Paris) using the 1.2 mm filter.

As with the 10-parameter fit, the standard deviations of the reduced chi-squares were one standard deviation from unity. Comparison of the different fits, using the source based system to excite the cadmium phantom with 2 mm wax overlay implied that there was distinct improvement in precision when using the 10-parameter or 9-parameter fit as opposed to the 11-parameter model. The precision,  $P$ , was determined using the relationship

$$P = \left( \frac{\sigma_A}{A} \right) \times 100 \quad (4.7)$$

$$A = h_p \times w_p \quad (4.8)$$

where  $A$  is the area of the peak with associated uncertainty  $\sigma_A$ ,  $h_p$  is the height of the peak and  $w_p$  is the width of the peak.

Thus, an improvement in the precision occurs when the uncertainty in the area is reduced.

Similar findings were ascertained for all the cadmium XRF investigations.

**Table 4.3: Determination of Precision for the different fitting programs**

<b>Precision Improvement Determination 2 mm</b>										
<b>Conc<sup>n</sup></b>	<b>0</b>	<b>4</b>	<b>9</b>	<b>17</b>	<b>34</b>	<b>51</b>	<b>68</b>	<b>102</b>	<b>138</b>	<b>170</b>
<b>11</b>	14.51	12.41	7.48	5.94	4.15	3.43	2.85	2.28	1.99	1.71
<b>10</b>	15.28	12.20	7.41	5.79	3.96	3.18	2.57	1.94	1.63	1.36
<b>9</b>	14.76	12.17	7.37	5.76	3.95	3.23	2.56	1.94	1.61	1.35

Further indium peak ratio investigations gave evidence to suggest that the 9-parameter fitting model may have some limitations. It was noted that when the highly concentrated phantoms were used, there was a definite increase in the indium alpha to beta peak ratio as the cadmium concentration increased. This trend was clearly evident.

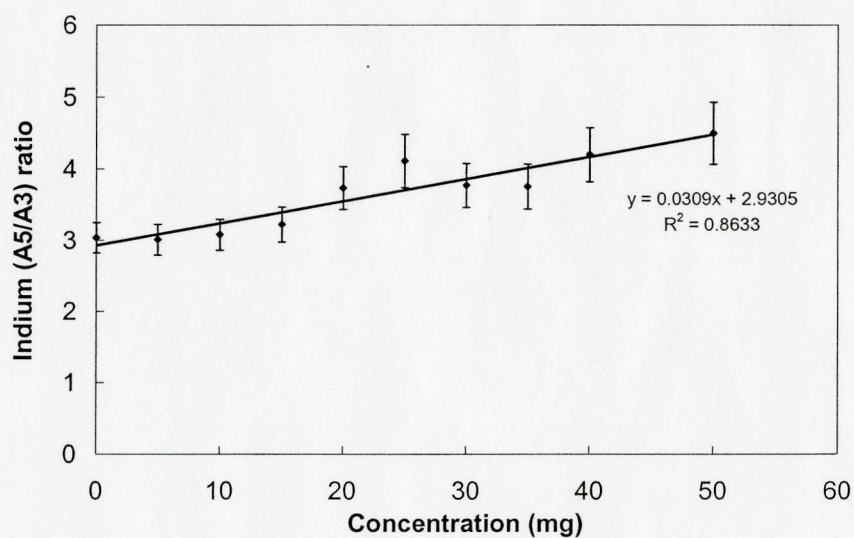


**Figure 4.20: Indium beta to alpha ratio for the more concentrated phantoms**

## Chapter 5

### Calibration Curves and Minimum Detectable Limits

#### 5.1 Introduction

##### 5.1.1 Determination of optimal fitting parameters

This chapter will look at and compare the detection limits for the different system configurations in order to determine which system configuration would lend itself to the best operable result. Ultimately, this chapter should enable us to identify a satisfactory and practical method for measuring cadmium *in vivo*. The quantity that facilitates this analytical reasoning is referred to as the Minimum Detectable Limit (MDL) and in this thesis it is measured in units of parts per million (ppm). Thus, the feasibility of each system's arrangement and configurations are essentially dependent on the projected nominal MDL values.

Regrettably, information on cadmium in bone is extremely limited as little is known of how sex, geographical location and race would affect bone cadmium retention. What is known is that there is an increase in *in vivo* cadmium, as age increases. Work at McMaster University has shown from the analysis of human bone samples, using NAA, that cadmium contamination of  $1.50 \pm 0.35$  ppm can be obtained (McNeill, 2001). Illustrating the necessity to have a system that can readily measure cadmium concentrations in that range. Ideally, if more information were currently available, then a

corresponding amount of bone cadmium could be related to an *in vivo* kidney cadmium concentration level.

Once the research on the optimal system design was completed, definitive measurements were studied. From chapter 4, the best background fitting model was obtained when a double exponential was used. For most of these measurements the  $\gamma$ -ray spectrum was acquired for 2000 seconds using the GL2020R detector with a 20.4 cm<sup>2</sup> entrance window. Note all MDL data were acquired using this HPGe detector for consistency. By the use of the common definition of lower limit of detection defined by Chettle *et al.*, 1991, the MDL based on each X-ray calibration line can be calculated as

$$MDL = \frac{2\sigma_{\text{zero concentration phantom}}}{\text{slope of calibration}} \quad (5.1)$$

where  $\sigma$  is the uncertainty in the X-ray peak counts.

More explicitly, this is the concentration that gives rise to a X-ray peak intensity (usually normalised to the coherent for high Z elemental analysis *e.g.* uranium (O'Meara *et al.*, (1998)), that is, twice the standard deviation in the measured concentration, in the limit of low phantom concentration. Therefore fitting models can be compared by the comparison of their calculated MDLs. Table 5.1 illustrates the comparison of two extreme fitting models using tied betas.

**Table 5.1: Determination of alpha and beta MDLs for the linear and exponential background fitting models, using the plaster of Paris phantoms. Results are given in ppm.**

<b>Linear Model</b>									
<b>Conc<sup>n</sup></b>	<b>0</b>	<b>4</b>	<b>9</b>	<b>17</b>	<b>34</b>	<b>68</b>	<b>102</b>	<b>138</b>	<b>170</b>
<b>α-MDL</b>	12.124	7.772	7.473	3.529	3.353	3.712	3.960	4.141	4.327
<b>β-MDL</b>	64.579	68.615	56.989	33.491	30.872	22.575	19.947	19.170	19.241
<b>Double Exponential Model</b>									
<b>Conc<sup>n</sup></b>	<b>0</b>	<b>4</b>	<b>9</b>	<b>17</b>	<b>34</b>	<b>68</b>	<b>102</b>	<b>138</b>	<b>170</b>
<b>α-MDL</b>	3.321	3.448	3.493	3.452	3.526	3.656	3.747	3.845	3.970
<b>β-MDL</b>	16.499	16.509	16.796	16.374	16.362	16.643	16.669	16.598	17.220

Note that results were obtained from the tied beta model.

Clearly, it can be seen from table 5.1 how the detection limit varies with concentration. In the linear model the background is modelled with a function of the form:

$$f(x) = Ax + B \quad (5.2)$$

Where  $x$  is the variable, and  $A$  and  $B$  are constants which represent the rate at which the background is increasing and the initial underlying background respectively. Whereas in the double exponential model, the background is modelled with a function of the form

$$f(x) = Ae^{Bx} + Ce^{-Dx} \quad (5.3)$$

When these models were studied in more depth, it appeared that the linear fit could of failed simply because this fit represented a strictly monotonic background which was definitely not the case, as the regions of interest for the acquired spectra fell in the crater of the valley. More appropriately, the double exponential fit that modelled both rises of the valley gave a superior fit in terms of estimates for the calculated MDL.

Based on the source based plaster of Paris measurements, the alpha and beta MDL for the exponential fit were found to be  $3.321 \pm 0.188$  ppm and  $16.499 \pm 0.536$  ppm respectively. Hence, the uncertainties in the X-ray peaks for the blank phantom spectrum predicted a combined inverse variance weighted MDL of 3.256 ppm.

### **5.1.2 Determination of the MDL for the Cadmium doped Plaster of Paris phantom.**

From figure 5.1, it is evident that there is a mildly increasing slope of  $0.00331 \pm 0.00024$  ppm with a corresponding  $R^2$  value of 0.966, indicating that the obtained information is fairly representative. Figure 5.1 implies that the minimum detection limit would occur when the concentration of the cadmium doped phantom is reduced.

Detection limits obtained for the water, the bare plaster of Paris, and the plaster of Paris (0 mm) wax overlay phantoms were studied and compared. Results indicated that the MDL increased, as the atomic number of the medium is increased.

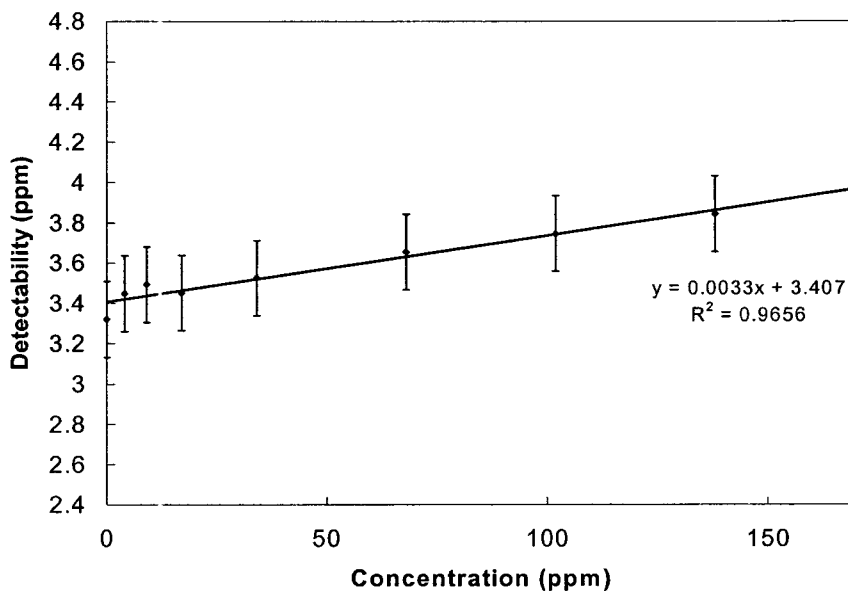


Figure 5.1: Detection level analysis for the cadmium plaster of Paris alpha peak using the exponential background fitting.

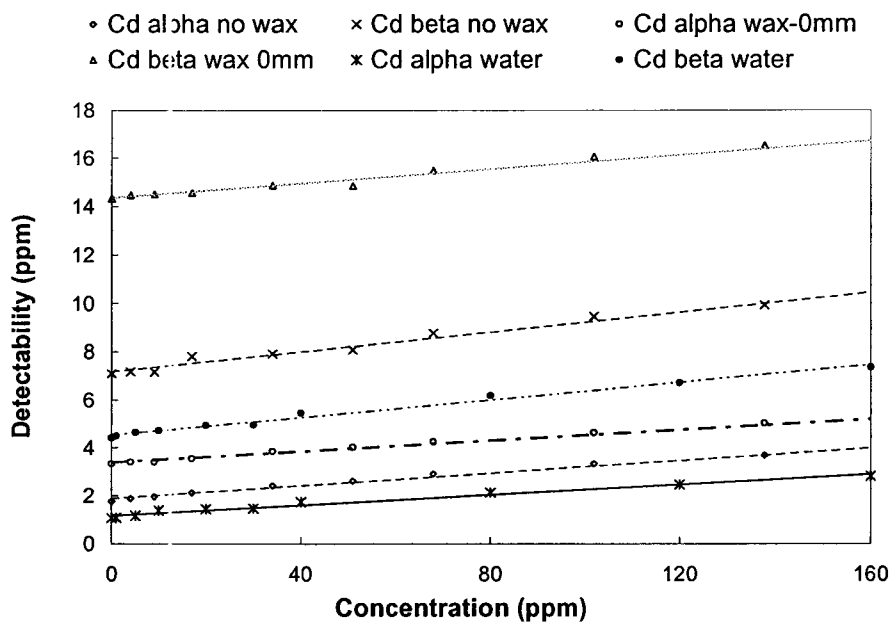


Figure 5.2: Variation in detectability for various target medium using the source-based collimator 8.75 mm for the water, plaster of Paris, plaster of Paris with wax 0 mm phantoms.

Figure 5.2 and table 5.2 predicts smaller MDL values for the water phantoms, as the atomic number of water is 7.2. When this is compared to plaster of Paris (atomic number 11.4 g/mol), there is a distinct increase in MDL. Theoretically, higher Z materials have higher attenuation coefficients; hence larger photon attenuation occurs inside the medium resulting in reduced photon fluence, less fluence implies fewer photons entering the detector. Therefore, fewer photons are collected in each channel, which results in lower alpha and beta peak counts, hence smaller calibration slope, thus higher calculated MDL. The final combined MDL can be calculated by taking the inverse weighted mean of the alpha and beta MDLs.

When the MDL values given in table 5.2 are analysed, a 66 % increase in MDL is noticed when the material is changed from water to calcium sulphate (plaster of Paris). Unfortunately, when the plaster of Paris phantom is subjected to surrounding wax tissue, the MDL is further increased. The estimated MDL approximately doubles the bare plaster of Paris. This increased MDL was too high for the successful measuring of bone cadmium. So further analysis was considered.

From a quick visual inspection of table 5.2, it is clear that better MDLs are obtained with smaller number of parameters. Note that the 7-parameter MDL estimates for the plaster of Paris (wax 0 mm) were unavailable, as the program was unable to model the acquired spectra.

**Table 5.2: Summary of the MDL analysis for the water, the plaster of Paris and the plaster of Paris with wax 0 mm phantom for the 7, 9, 10 and 11 parameter fits wherever possible using the source based measuring technique.**

<b>Water</b>											
<b>Cd<sub>α</sub></b>	<b>Conc<sup>n</sup></b>	<b>0</b>	<b>1</b>	<b>5</b>	<b>10</b>	<b>20</b>	<b>30</b>	<b>40</b>	<b>80</b>	<b>120</b>	<b>160</b>
11	MDL	1.146	1.136	1.253	1.479	1.566	1.603	1.939	2.460	2.962	3.415
10	MDL	1.136	1.129	1.225	1.416	1.484	1.508	1.753	2.147	2.477	2.817
9	MDL	1.065	1.067	1.163	1.370	1.431	1.463	1.719	2.116	2.462	2.806
7	MDL	1.058	1.063	1.157	1.361	1.421	1.453	1.709	2.105	2.448	2.789
<b>Cd<sub>β</sub></b>											
11	MDL	4.853	4.882	5.069	5.072	5.292	5.192	5.706	6.349	6.896	7.573
10	MDL	4.711	4.769	4.929	5.018	5.237	5.232	5.716	6.439	6.933	7.590
9	MDL	4.420	4.498	4.645	4.724	4.939	4.957	5.454	6.186	6.705	7.345
7	MDL	4.384	4.453	4.604	4.705	4.919	4.937	5.425	6.146	6.668	7.316
<b>Bare plaster of Paris</b>											
<b>Cd<sub>α</sub></b>	<b>Conc<sup>n</sup></b>	<b>0</b>	<b>4</b>	<b>9</b>	<b>17</b>	<b>34</b>	<b>51</b>	<b>68</b>	<b>102</b>	<b>138</b>	<b>170</b>
11	MDL	1.833	1.961	2.041	2.202	2.563	2.813	3.166	3.737	4.260	4.625
10	MDL	1.843	1.977	2.050	2.197	2.501	2.682	2.994	3.403	3.777	4.062
9	MDL	1.739	1.870	1.950	2.103	2.409	2.607	2.906	3.323	3.693	3.992
7	MDL	1.742	1.873	1.948	2.107	2.413	2.611	2.911	3.321	3.695	3.995
<b>Cd<sub>β</sub></b>											
11	MDL	7.453	7.508	7.550	8.167	8.333	8.412	9.020	9.800	10.278	10.795
10	MDL	7.349	7.429	7.443	8.067	8.181	8.323	9.029	9.753	10.210	10.791
9	MDL	7.079	7.162	7.155	7.798	7.908	8.077	8.763	9.452	9.923	10.514
7	MDL	7.089	7.172	7.192	7.811	7.922	8.095	8.779	9.510	9.973	10.567
<b>Plaster of Paris (wax 0 mm)</b>											
<b>Cd<sub>α</sub></b>	<b>Conc<sup>n</sup></b>	<b>0</b>	<b>4</b>	<b>9</b>	<b>17</b>	<b>34</b>	<b>51</b>	<b>68</b>	<b>102</b>	<b>138</b>	<b>170</b>
11	MDL	3.306	3.434	3.424	3.550	3.894	4.085	4.370	4.820	5.381	5.512
10	MDL	3.335	3.411	3.406	3.559	3.851	4.025	4.265	4.641	5.037	5.151
9	MDL	3.328	3.406	3.401	3.553	3.847	4.020	4.260	4.636	5.032	5.146
<b>Cd<sub>β</sub></b>											
11	MDL	14.586	14.995	14.991	14.892	15.284	15.177	15.836	16.174	16.716	16.784
10	MDL	14.617	14.754	14.773	14.853	15.149	15.138	15.764	16.337	16.791	16.922
9	MDL	14.323	14.459	14.491	14.556	14.860	14.850	15.478	16.052	16.516	16.641

Note that the results were obtained by using the separated beta peak model.

## 5.2 Source based analysis

For the source-based technique, a distance of 2 cm was chosen rather than a shorter one. This distance gave the best fluence rate in terms of the throughput and dead time. Actually, the count rate, hence the dead time of the system would be too high to irradiate the whole phantom, if it were placed closer. Also, this distance allowed sufficient space for the variation of overlying wax thickness.

### 5.2.1 Determination of the MDL for the Cadmium doped Water phantom

The calibration curve was obtained by plotting the cadmium alpha peak versus concentration. The regression line was determined from the graph. A positive intercept indicated that there might be some trace of cadmium contamination in these phantoms, however this intercept was relatively small when compared to the total peak counts, hence the amount of cadmium contamination was considered negligible.

Graphically, from figure 5.4, the alpha and beta MDL can be estimated from the intercept as 1.163 ppm and 4.539 ppm, which compared reasonably well to the calculated values of  $1.065 \pm 0.086$  ppm and  $4.420 \pm 0.370$  ppm respectively. Therefore, for the water-based phantom with no tissue overlay, the combined MDL was 1.035 ppm of cadmium. Since MDLs of the order of 1.00 ppm are definitely measurable with the water phantoms, the application for an *in vivo* XRF analysis of blood cadmium can be considered.

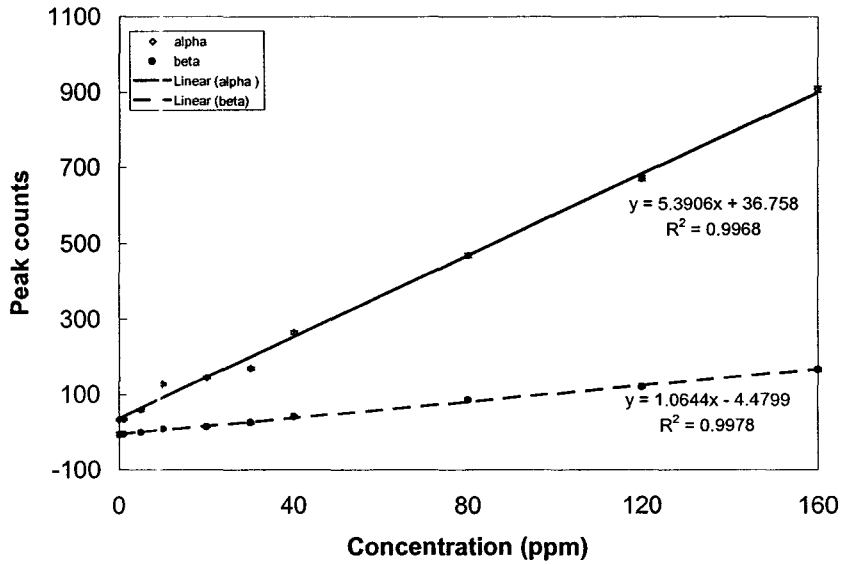


Figure 5.3: Variation of the fitted peak amplitudes for the cadmium peaks for the cylindrical set of phantoms placed 2 cm away from source, using the 8.75 mm collimator.

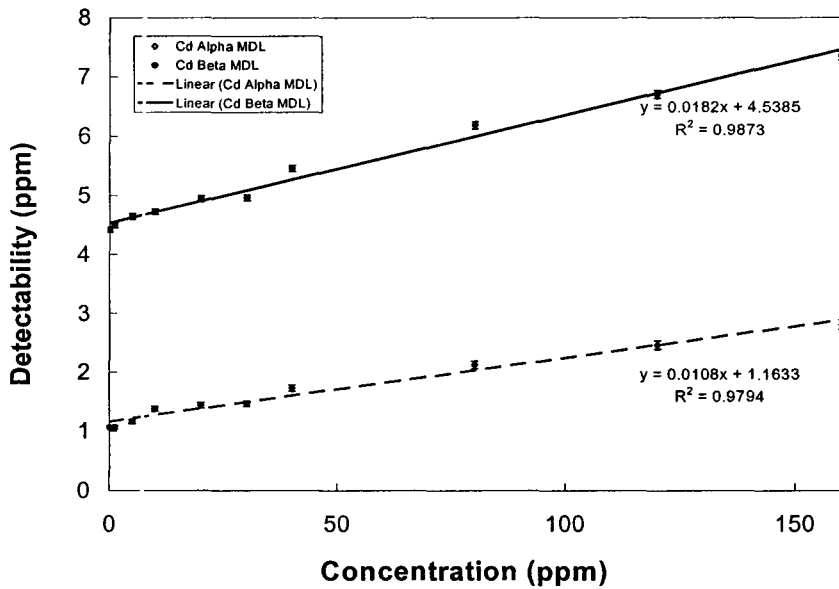


Figure 5.4: Variation in detectability for the various water phantom concentrations using the 9-parameter fit with the 8.75 mm collimator. In general, the detectability increases, as concentration increases.

**Table 5.3: Summary of regression analysis of 2 calibration lines for the cadmium bone system.**

X-ray	Slope $\pm \sigma(\text{slope})$ [ppm <sup>-1</sup> ]	Intercept $\pm \sigma(\text{intercept})$	R <sup>2</sup> value
K <sub>α</sub>	5.391 $\pm$ 0.109	36.758 $\pm$ 7.648	0.997
K <sub>β</sub>	1.064 $\pm$ 0.018	-4.480 $\pm$ 1.233	0.998

Table 5.3 contains the results of the regression analysis for the calibration lines shown in figure 5.3. Calibration lines were established with the cadmium doped water phantom. The slope and intercept of each line were used to determine the cadmium concentration from an *in vivo* measurement.

### **5.2.2 Determination of the MDL for the cadmium doped plaster of Paris phantom in wax.**

There is a large difference in the MDL estimates for the water and the plaster of Paris phantoms as seen in table 5.2. This increased MDL could be accounted for by realising that the background near the region of interest was bigger because of the presence of an enhanced indium peak. Interestingly, the indium peak in the spectrum increased substantially with increase in tissue overlay as compared to the cadmium peak. This observation can be explained explicitly; the cadmium and indium X-rays are of similar energy, hence these X-rays would have a similar probability for attenuation in the overlying tissue. In this respect, the differential attenuation of the scattered  $\gamma$ -ray is approximately same. However, as the overlying soft tissue (wax) depth increases, the uncollided photon flux at the bone decreases. This results in a corresponding decrease in the cadmium X-ray production due to the attenuation of the uncollided beam, but there is no decrease in the production of the indium X-rays as they are inherent to the detector

(not in the phantom). Thus, the ratio of the cadmium X-ray intensity to the indium X-ray intensity would decrease with increasing overlying soft tissue. The overall MDL performance for this detection system as wax thickness is increased, are summarised in table 5.4.

**Table 5.4: Summary of the determined MDL using the 9-parameter fitting model for the plaster of Paris phantoms with increasing wax tissue overlay.**

Conc <sup>a</sup>	0	4	9	17	34	51	68	102	138	170
<b>wax-1MM</b>										
$\alpha$ -MDL	3.354	3.447	3.499	3.660	3.829	4.092	4.259	4.691	4.993	5.249
$\beta$ -MDL	14.670	14.495	14.732	14.873	15.020	15.247	15.571	16.240	16.698	16.939
<b>wax-2MM</b>										
$\alpha$ -MDL	3.318	3.334	3.445	3.567	3.793	3.937	4.165	4.537	4.837	5.254
$\beta$ -MDL	14.479	14.413	14.762	14.827	15.132	15.319	15.545	16.009	16.615	17.275
<b>wax-3MM</b>										
$\alpha$ -MDL	3.551	3.642	3.691	3.763	4.015	4.152	4.362	4.761	5.087	5.600
$\beta$ -MDL	15.608	15.893	15.981	16.068	16.484	16.398	16.780	17.387	17.860	19.036
<b>wax-5MM</b>										
$\alpha$ -MDL	3.997	4.051	4.133	4.227	4.470	4.661	4.883	5.246	5.607	5.791
$\beta$ -MDL	18.959	19.060	19.070	19.055	19.419	19.442	20.152	20.707	21.034	21.629
<b>wax-8MM</b>										
$\alpha$ -MDL	5.039	5.181	5.169	5.293	5.551	5.777	5.863	6.328	6.653	6.879
$\beta$ -MDL	18.293	18.222	18.015	18.401	18.596	18.721	18.749	19.321	19.762	20.436

For a wax thickness overlay of 3 mm the results from this source based cadmium work predict alpha and beta MDLs of  $3.551 \pm 0.180$  ppm and  $15.608 \pm 0.512$  ppm respectively. Estimating a combined MDL of 3.46 ppm with a corresponding dose of  $3.06 \pm 0.06$   $\mu$ Sv at 20 mm, using a 8 75 mm collimator. Moreover, it is clear that the MDL increases as the wax thickness increases. This phenomenon is illustrated in figure 5.5. Note that the dose associated with such a measurement is considerably small in comparison to the dose obtained by NAA. Pejović-Milić *et al.*, 2000 reported doses of 1.5–2.5 mSv in 180 seconds for bone aluminium measurements.

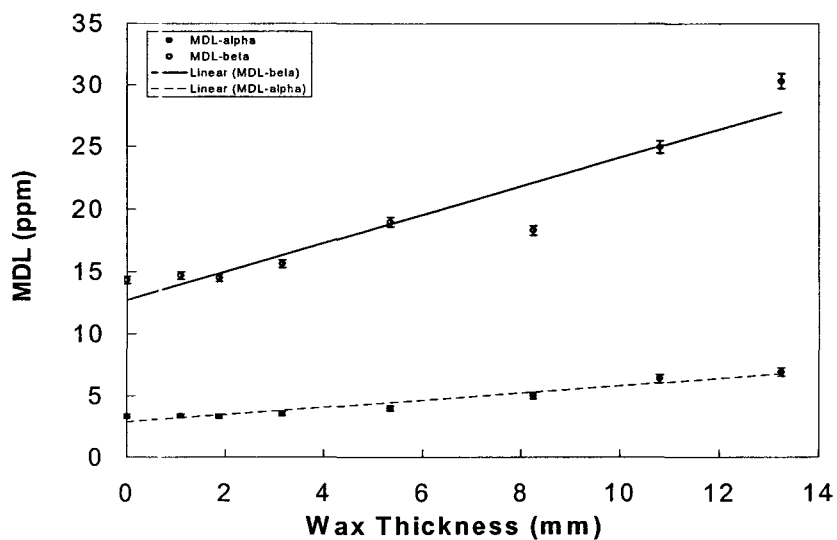


Figure 5.5: MDL versus wax thickness variation for the 8.75 mm collimator.

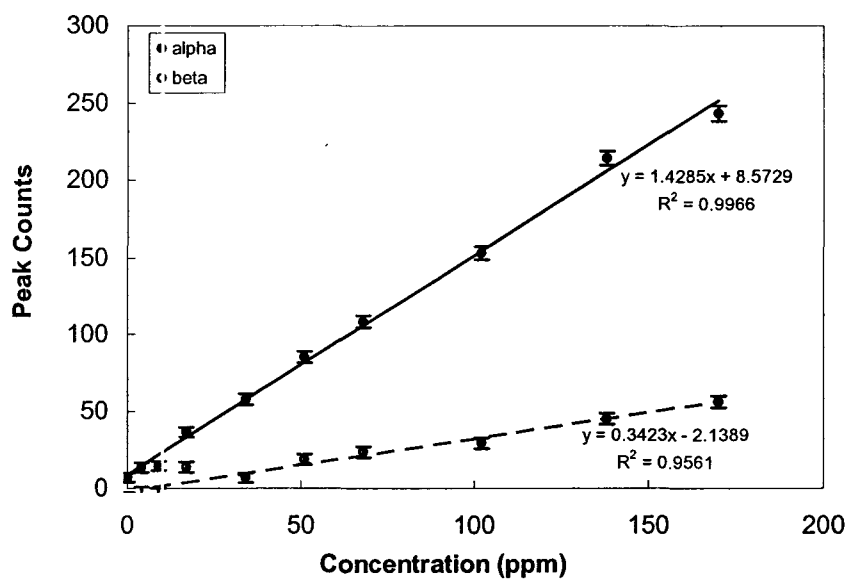


Figure 5.6: Alpha and beta calibration curve using 10.75 mm collimator.

### 5.3 Collimator considerations

A size difference between the phantom and the detector's surface led to the conclusion that a loss of radiation would be significant for a precise measurement. So for this source-based work, the effect of collimator length on MDL was investigated. The length of the collimator was changed steadily starting with a length of 12.75 mm. Then, by removing 2 mm of the tungsten collimator each time, comparisons of 12.75 mm, 10.75 mm, and 8.75 mm were made. The latter, the same as the original collimator length.

Theoretically, the longer the collimator, the less the photon fluence, since only the highly forward directed photons would reach the phantom, whilst the other scattered photons would be more attenuated, hence a smaller background due to Compton scatter. Since there is a reduction in the photon fluence, there is a reduction in the dose deposited as well. Figure 5.3 and figure 5.6 show the peak counts obtained when the 8.75 mm and 10.75 mm collimators are used. It is evident that these results support the theory, as fewer counts are attained when the collimator length is increased.

Initially, by looking at the first result, as seen from the graph shown in figure 5.7, it would seem as though the MDL actually worsens. This was somewhat unexpected! If however, we consider the dose normalised MDL, then it is realised that the use of a longer collimator is comparable; actually better than the use of a shorter collimator. Table 5.5(a, b and c) show the effect of collimator length on the normalised MDL for a 2000 seconds live time measurement.

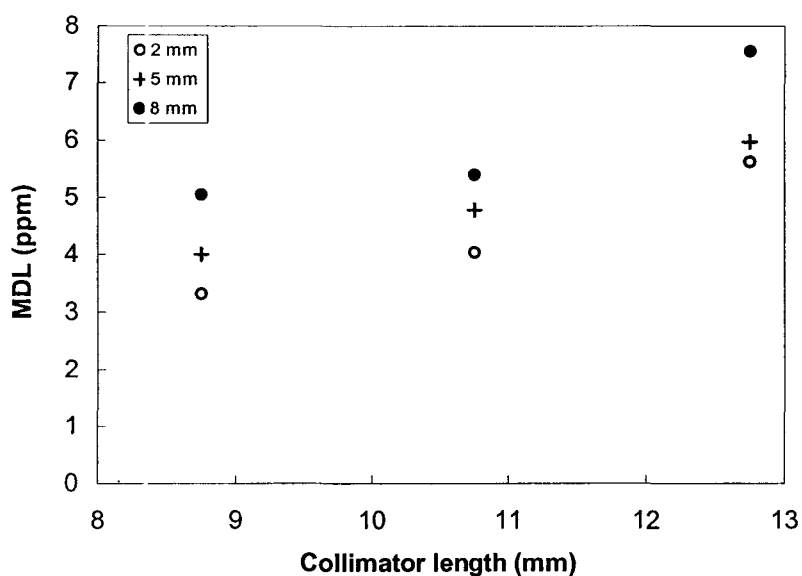


Figure 5.7: MDL versus collimator variation for the 2 mm, 5 mm and 8 mm wax overlay.

Table 5.5a: Collimator variation for wax thickness 2 mm

Collimator length (mm)	8.75	10.75	12.75
MDL (ppm)	3.234	3.931	5.446
Dose (mrad)	0.31	0.2	0.08
Normalised MDL(ppm.mrad <sup>1/2</sup> )	1.801	1.758	1.540

Table 5.5b: Collimator variation for wax thickness 5 mm

Collimator length (mm)	8.75	10.75	12.75
MDL (ppm)	3.911	4.654	5.811
Dose (mrad)	0.31	0.2	0.08
Normalised MDL(ppm.mrad <sup>1/2</sup> )	2.178	2.081	1.644

Table 5.5c: Collimator variation for wax thickness 8 mm

Collimator length (mm)	8.75	10.75	12.75
MDL (ppm)	4.904	5.278	7.343
Dose (mrad)	0.31	0.2	0.08
Normalised MDL(ppm.mrad <sup>1/2</sup> )	2.730	2.360	2.077

## 5.4 Polarised XRF analysis

### 5.4.1 MDL determination of optimal filter thickness

Since the source based technique, though promising gave a MDL of  $\sim 3.5$  ppm in wax it was above acceptable. So a different approach was investigated. By using the polarised technique with no filter and no wax, a MDL of 0.555 ppm was recorded for the plaster of Paris phantoms. This estimated MDL looked extremely promising. However, this MDL estimate could be somewhat misleading, as the effect of the wax thickness overlay or the dose associated with this measurement was not considered.

**Table 5.6: MDL versus filter thickness. The analysis was obtained by using the bare plaster of Paris phantom with no wax overlay**

Filter thickness (mm)	0	0.2	0.4	0.6	0.8	1.1	1.2	1.3	1.4	1.5	1.6	1.7
MDL $\alpha$	0.570	0.921	1.217	1.101	1.716	2.118	1.962	2.425	2.103	2.841	2.654	4.385
MDL $\beta$	2.429	3.620	4.544	4.507	7.246	7.230	6.994	8.544	8.375	10.311	9.520	15.408
$\beta/\alpha$ ratio	4.231	3.932	3.732	4.095	4.222	3.414	3.565	3.524	3.982	3.629	3.587	3.514
MDL <sub>total</sub>	0.555	0.892	1.176	1.069	1.670	2.032	1.889	2.332	2.040	2.739	2.556	4.218

Again, as with the source-based collimation, one must consider normalising these values to dose to make a fair comparative comment. Clearly, if dose is not a crucial factor then this method can be considered to produce the required MDL. Subsequently, after the polarised MDLs were normalised, it was realised that the source based technique resulted in superior normalised MDLs.

Importantly, the reason for such a XRF study hinges on the fact XRF doses are marginal when compared with NAA doses. Also, problems in identifying the correct location of

the kidney seem to render NAA difficult. Therefore, although the dose produced from this polarised XRF technique maybe higher than the source based, it is clearly less than NAA, making this technique feasible if necessary.

Before making use of the polarised system (obviously, a more complex system than source based), the dead time associated for each filter thickness was considered. Based on the results as shown in figure 5.8, the 1.2 mm filter was smallest filter below the allowable dead-time limit, thereby rendering this filter the preferred choice. However, from figure 5.9 it was clear that MDL varied as the amount of filtration increased. More succinctly, the MDL increased as the filter thickness increased; hence some trade-off was required. Further investigations showed that probably a better estimate for MDL might be predicted if a 0.6 mm filter was used instead. This prediction was justified in figure 5.10 when filter thickness was plotted against the normalised MDL.

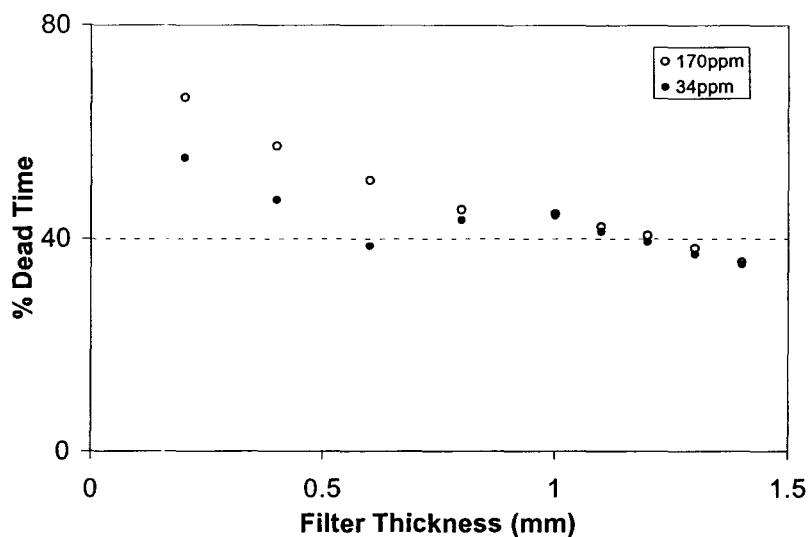


**Figure 5.8: Dead time versus filter thickness for the polarised XRF measurement.**

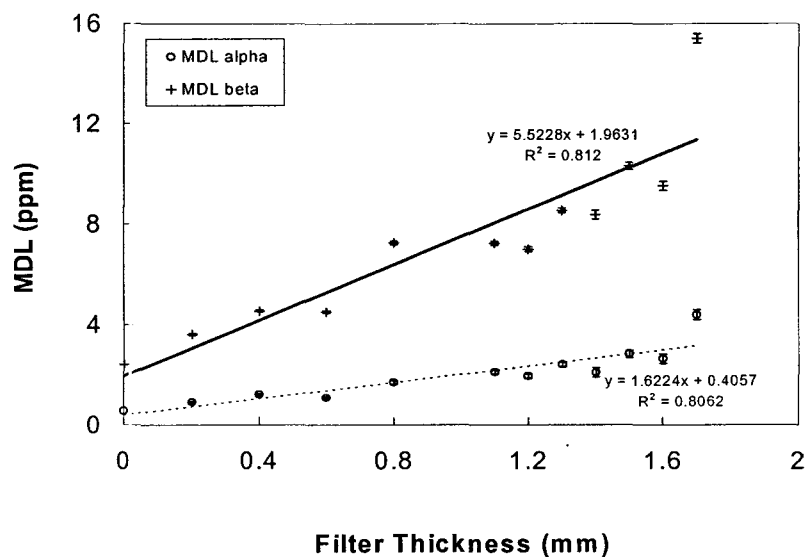


**Figure 5.9: MDL filter thickness variation for the polarised system using voltage of 175 kV with a current of 12.5 mA.**

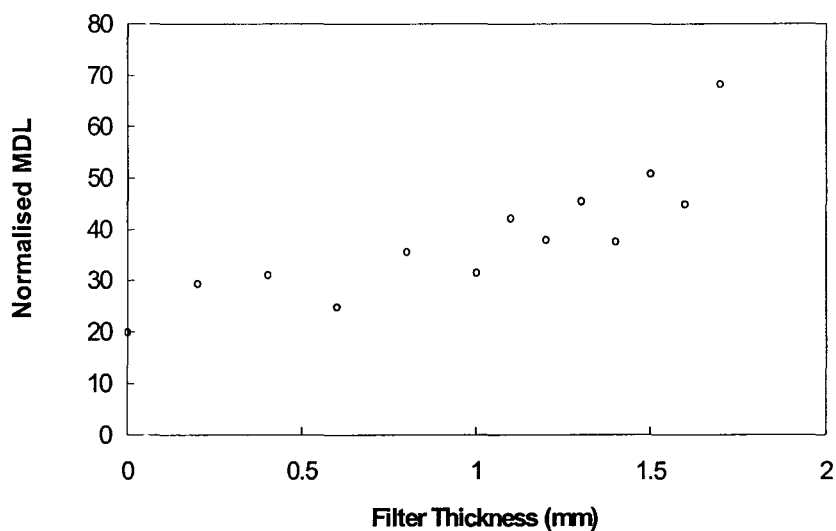


**Figure 5.10: Dose normalised MDL versus filter thickness for the polarised XRF measurement.**

#### 5.4.2 MDL determination using a 1.2 mm filter

Using the standard experimental procedure for phantom irradiation, 10 plaster of Paris phantoms ranging from 0 to 170 ppm were irradiated and the spectrum analysed to determine the cadmium MDL. The region of interest was fitted with an exponential background, as was the case with the source-based analysis. Then the alpha and beta intensities were plotted against concentration as shown in figure 5.11 and figure 5.12. The results of regression analysis of these calibration lines are shown on the graph. It should be noted that the X-ray intensities were not normalised to any intensity, as there was no evidence of ratio consistency *e.g.* cadmium to indium ratio was not constant.

Recall the slope of the calibration line may be used as a characteristic of the overall properties set during the procedure such as irradiation parameters, counting system, geometry, and fitting routine. As before, the MDL based on each X-ray calibration line was then calculated. Comparing the slopes of the calibration curves obtained for alpha and beta peaks, it was interesting to note that the alpha slope is much greater than the beta slope resulting in less uncertainty, thus better MDLs. This was clearly illustrated in table 5.7. These calculated MDL values were comparable with the results obtained using the source-based technique shown previously in table 5.4. These MDL values increased two fold with the addition of surrounding wax tissue. This was seen as the MDL prior to the surrounding wax overlay gave a combined MDL of 1.89 ppm as opposed to 3.05 ppm, after the addition of the surrounding wax, for the blank phantom spectra. Both of the MDL values quoted are for live time measurements of 2000 seconds using the polarised

system with the 1.2 mm filter. These combined MDL values should not be compared directly with the source-excited system, as this would not be a fair comparison. However, from table 5.2, the combined determined MDL obtained for the source-excited experiment, in 2000 seconds live time measurement was 1.69 ppm and 3.24 ppm respectively.

**Table 5.7: Summarising the MDL Variation with wax thickness using a 1.2 mm external copper filter**

Wax thickness	Slope	Uncertainty	MDL	Uncertainty
Alpha				
0 mm	6.245 ± 0.123		3.124 ± 0.606	
2 mm	5.696 ± 0.327		3.337 ± 0.966	
3 mm	5.186 ± 0.166		3.469 ± 1.435	
8 mm	4.722 ± 0.063		4.219 ± 2.007	
Beta				
0 mm	1.395 ± 0.064		13.654 ± 0.492	
2 mm	1.301 ± 0.073		14.116 ± 0.360	
3 mm	1.189 ± 0.064		14.335 ± 0.211	
8 mm	1.108 ± 0.053		17.211 ± 0.246	

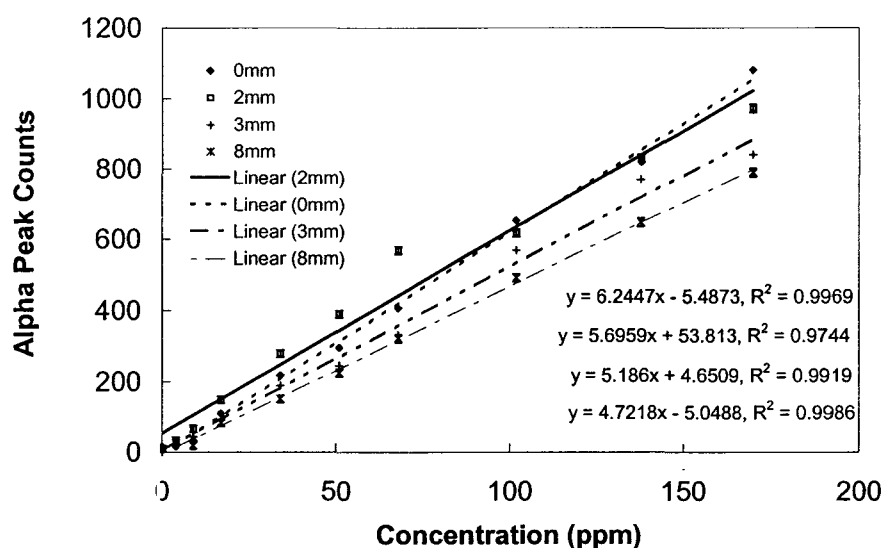


**Figure 5.11: Cadmium alpha calibration curve for the 1.2 mm filter, tubular set of plaster of Paris phantoms measured using a HPGe detector. Irradiation in a 90° geometry, 20 mm sample to detector distance.**

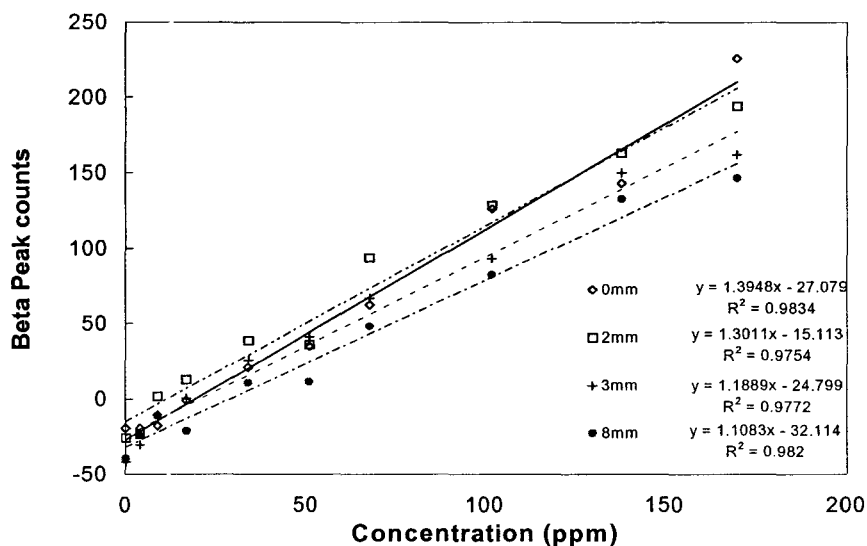


Figure 5.12: Cadmium beta calibration curve for 1.2 mm filter, the tubular set of plaster of Paris phantoms measured using a HPGe detector. Irradiation in a 90° geometry, 20 mm sample to detector distance.

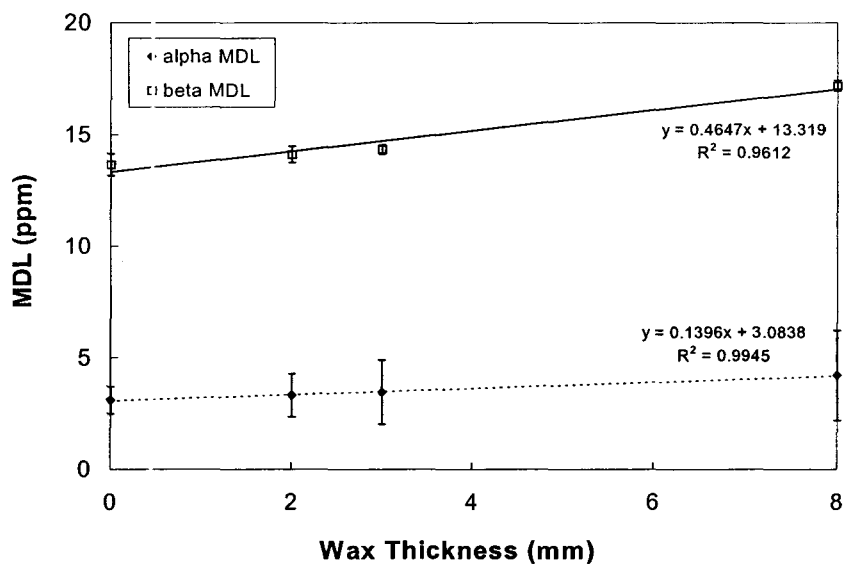


Figure 5.13: MDL wax thickness for the polarised system using a 1.2 mm external copper filter.

Hence, similar trends have been noticed with the polarised and source based techniques. In both techniques there is an increase in the MDL with increasing overlying thickness. In figure 5.13 there exist a more significant MDL variation for the beta as oppose to the alphas. With the beta to alpha MDL slope ratio being 3.329. Additional analysis showed that this ratio should increase, as the tissue thickness increased. Thus a ratio of the betas to alphas could be used for tissue thickness determination.

This finding maybe explained mathematically, by noting that the detection limit is proportional to the square root of the background,  $b$ , and inversely proportional to the signal,  $s$ , therefore:

$$MDL = A \cdot \frac{\sqrt{b}}{s} \quad (5.4)$$

where  $A$  is a numerical constant

For similar spectral background, the signal of the alpha peak is greater than the beta peak signal resulting in a lower estimate for the alpha MDL. Also since the  $K_{\beta}$  X-rays are more penetrating than the  $K_{\alpha}$  X-rays, there are less affected by tissue thickness attenuation. Hence there is a variation in the beta to alpha MDL ratio.

## 5.5 Dosimetry

One of the most important factors for determining the feasibility of any *in vivo* measurement system is the amount of dose that will be delivered to the subject. By correcting the lead system dose for  $\gamma$ -ray energy and source intensity, an estimate of the effective dose can be readily made. The validity of this effective dose estimate for the cadmium source based system was sound because of the marked similarities with the bone lead system. The equivalent dose to the skin surface above bone from a typical lead exam has been accurately determined to be 0.035  $\mu\text{Sv}$  (Todd *et al.*, 1992) and 0.030  $\mu\text{Sv}$  (McNeill, 1998) each for a 30 minute measurement. However, by using NAA, Arnold (2001) reported dose estimates of the order of 66  $\mu\text{Sv}$ , for 10 minute manganese measurements.

Todd *et al.* used a 2.2 GBq  $^{109}\text{Cd}$  source, compared to the 0.37 GBq  $^{109}\text{Cd}$  source used here, so the photon fluence rate was almost 6 times higher for the lead system. Also, these bone cadmium measurements took 2000 seconds compared to the 1800 seconds used for bone lead analysis. Hence combining these factors an effective dose of 6.5 nSv could be predicted for a bone cadmium assessment for a 2000 second measurement providing the geometry used was the same. When the dose was calculated by using the results as obtained by the dose monitor, a dose of  $3.1 \pm 0.1 \mu\text{Sv}$  was predicted. This discrepancy could be due to the shape of source used and also the distance at which the measurements were taken. However, this delivered dose was still definitely below the annual effective background dose limit of 3 mSv/yr (ICRP 30, 1979).

Importantly, this average dose value depends on the field in which the monitor was calibrated. The dosimeter (Nuclear Enterprises Model # 0500) used was pre-calibrated by the McMaster University Department Of Risk Management Services. Thus, the dose to the bone phantom reported in this study was calculated using this dosimeter. The dose quoted for a 20 minute interval is an overestimation, since when the dose was collected for a longer time interval the average dose was found to be less. This discrepancy could be due to the variability of the background, although this varying background factor was monitored. A brief description of the dose measuring procedure will be discussed later in this section. Therefore, a conservative approach was preferred, thus avoiding an underestimating of the delivered dose. These doses were ultimately used to determine the normalised MDL ( $\text{MDL} \times \sqrt{\text{bone dose}}$ ) values.

In general, the MDL is influenced by change in the irradiation settings. If the dose were to be increased by a factor of 9, then the MDL obtained for the cadmium phantoms measured by the germanium detectors would decrease by approximately 3. This would make the MDL comparable to the observed cadmium level in a 50 year old reference man ( $1.5 \pm 0.35$  ppm). Therefore the dose may be increased to improve the MDL. An increase in dose can be achieved in different ways, by either increasing the irradiation time, the source to sample distance or incident photon flux. Thus, these factors can be manipulated to obtain an acceptable MDL. This increase in the dose delivered to the bone, although in contrast with the ALARA principle is still very minimal and well below the annual

background exposure to radiation as this effective delivered dose is a couple of decades less than annual background.

Experimentally, in assessing the variability of the background accumulation for a fixed time period, several preliminary dosimeter readings were done. Fundamentally, dosimeters can accumulate significant background readings due to continuous exposure to background radiation. In order to determine the exposure due to the irradiation procedure accurately, it is necessary to ensure that the background exposure is reasonably constant over a given time period, so comparisons between readings from the irradiation were made. This was done by the use of 2 dosimeters. One measuring background, the other measuring the dose emitted from the source. If the background reading varied to an unacceptable degree then it was considered unrepresentative and was thus rejected. Hence several readings were discarded.

Both dosimeters were zeroed in order to clear residual background exposure. Then the dose from the  $^{109}\text{Cd}$  source was measured using the NRB dosimeter, which was actually an ionisation chamber. Usually, measurements should be corrected for atmospheric pressure and temperature since the chamber contains vented air, and therefore the volume of irradiated gas depends on these factors. However, these factors were assumed to be constant over the measurement period, as changes in the room temperature and the atmospheric pressure were negligible.

Alternatively, the absorbed dose,  $D_m$ , can be determined from the exposure rate,  $X$ , through the standard expression:

$$D_m = 34 \cdot \frac{\left(\frac{\mu}{\rho}\right)_m}{\left(\frac{\mu}{\rho}\right)_{air}} \cdot X \quad (5.5)$$

where  $(\mu/\rho)_m$  and  $(\mu/\rho)_{air}$  are the mass energy absorption coefficients of the two media. However, these mass energy absorption coefficients are also a function of photon energy, so the weighted average ratio of these coefficients should be used to convert exposure to dose.

From looking and comparing the estimated normalised MDLs for the different system configurations, it is obvious that the source-based system is superior to the polarised technique, and thus should be the preferred choice. By simple comparison of the 2 mm wax thickness overlay, the polarise technique predicts a normalised MDL of 5.988 ppm.mrad<sup>1/2</sup> compared to 1.771 ppm.mrad<sup>1/2</sup> for the source based technique which could be further reduced to 1.540 ppm.mrad<sup>1/2</sup> by the use of a 12.75 mm collimator. Similar trends are also noted for other wax thickness.

**Table 5.8: Normalised (MDLs) and doses delivered to the cylindrical set of phantoms during a 2000 seconds cadmium measurement. Source based distance (20 mm)**

Wax thickness (mm)	NRB Dose (mrad)	MDL (ppm)	Normalised MDL (ppm.mrad <sup>1/2</sup> )
No wax	0.3	1.739	0.952
0	0.3	3.241	1.775
1	0.3	3.270	1.791
2	0.3	3.234	1.771
3	0.3	3.463	1.897
5	0.3	3.911	2.142
8	0.3	4.858	2.661
11	0.3	6.193	3.392

**Table 5.9: Normalised (MDLs) and doses delivered to the cylindrical set of phantoms during a 1000 seconds cadmium measurement. Varying filter thicknesses. Bare plaster of Paris phantoms.**

Filter thickness (mm)	NRB Dose (mrad)	MDL (ppm)	Normalised MDL (ppm.mrad <sup>1/2</sup> )
0	5.5	0.555	1.302
0.2	4.6	0.892	1.913
0.4	2.95	1.176	2.020
0.6	2.3	1.069	1.621
0.8	1.95	1.670	2.332
1	1.9	1.546	2.131
1.1	1.8	2.032	2.726
1.2	1.7	1.889	2.463
1.3	1.6	2.332	2.950
1.4	1.45	2.040	2.456
1.5	1.45	2.739	3.298
1.6	1.3	2.556	2.914
1.7	1.1	4.218	4.424

**Table 5.10: Normalised (MDLs) and doses delivered to the cylindrical set of phantoms during a 2000 seconds cadmium measurement. Filter thickness (1.2 mm)**

Wax thickness (mm)	NRB Dose (mrad)	MDL (ppm)	Normalised MDL (ppm.mrad <sup>1/2</sup> )
No wax	3.4	1.336	2.463
0	3.4	3.045	5.615
2	3.4	3.247	5.988
3	3.4	3.372	6.217
8	3.4	4.098	7.556

## 5.6 Clinical Implications

When the clinical prospects are considered for the two types of systems, it is interesting to note that for the polarised system the sensitivity is better, hence the MDL estimate is somewhat lower or even better. However, the dose released is more than ten times larger than the source base system. In an effort to reduce dose, the polarised beam can be filtered, but the filtration of the polarised beam decreases both dose and system sensitivity. Coupled with this larger dose is the mobilisation difficulty of the polarised system, it is not easily transportable. Therefore, since the polarised system used here does not produce significant benefits over the source-based technique, the source-based technique would be preferred in the future if XRF *in vivo* measurements are to be incorporated into the clinical environment.

## Chapter 6

### Conclusions and Future Work

#### 6.1 Evidence for Cadmium *In Vivo* XRF Measurement

In this chapter the potential for measuring cadmium *in vivo* will be discussed as the present XRF technique has major limitations. Currently, XRF cannot be used successfully for the measurement of large joints or deep-seated tissues. Hence further improvements in this technique must be adopted for routine occupational monitoring. Thus, presenting the opportunity for several ideas to be considered in the future.

Presently, despite the limited available data of bone-cadmium concentrations in both occupational and non-occupational groups, two studies have shown that cadmium levels in excess of 1 ppm can be measured. It has been reported that in 1975, the bone-cadmium of a nickel-cadmium battery factory worker, using NAA, was 15 ppm in the hip joint. This concentration is definitely not the expected concentration to be found in most individuals as this concentration represented an upper bound. Recent work suggests that 1 ppm bone-cadmium could be common in the 50+ population who were exposed to a cadmium contaminated environment (McNeill, 2001). Cases of interest are in the countries of Japan and Belgium, where there has been significant evidence for concern. Blood cadmium levels of 1.2  $\mu\text{g/l}$  have been reported (Lauwerys *et al.*, 1990). To date,

there is no feasible system that can readily measure an afflicted cohort of workers in order to identify excessive levels of cadmium contamination.

Thus, it is imperative that a system be available to measure such concentrations. Hence steps must be taken towards developing a facility for the measuring of cadmium *in vivo*. Even with pertinent information from this research, the fact still remains that the attainable MDL must be lowered to allow for the complete monitoring of bone-cadmium. Implying that some enhanced technique is needed, thereby improving the MDL without compromising the subject's dose. Therefore, with further improvements, the bone-cadmium content could be measured and consequently correlated to the number of years worked or exposed to such a toxin.

Fortunately, toxic manifestations of cadmium do not present themselves until kidney-cadmium concentrations of 200  $\mu\text{g/g}$  wet weight are noticeable (Nordberg *et al.*, 1971). Albeit kidney-cadmium levels of 4 ppm and liver cadmium levels of 2 ppm have been observed for the average standard man in the U.S, U.K and Sweden (Vartsky *et al.*, 1977). However, there have been little or no autopsy data for bone-cadmium levels. Thus with more available information, the kinetics of this toxic element could be more readily understood. Moreover, there has been no evidence to suggest that cadmium affects our cognitive or neurological abilities. Thus, there are no visible or mental preliminary symptoms.

Since conventional electronics and germanium detectors were used in this study, the present XRF system used can be made more sensitive with additional modifications. It is postulated that digital electronics would serve to lower the MDL considerably (Fleming,

1998, Bateman *et al.*, 2000). In addition, a more appropriate detector can be used for these cadmium X-ray energies for example; a lithium drifted silicon detector should further reduce the MDL (Nilsson *et al.*, 1990). Implying that there is a great possibility these improvements would make this system sufficiently precise for the particular application of measuring cadmium *in vivo*. Actually, an overall improvement in the detection limit by a factor of 2 is a realistic possibility.

## 6.2 Comparison of Photon sources

Recall from chapter 5, that similar MDL values were determined for the cadmium-109 source-excited system and the polarised system. From table 5.8 and 5.10, MDL values of  $3.5 \pm 0.2$  ppm and  $3.5 \pm 1.4$  ppm in 3mm wax tissue equivalent overlay were obtained for the source-excited system and the polarised system respectively. These findings are promising and thus there is great motivation to continue this research at this time, especially since the equipment used for this research could definitely be optimised. However, it is unclear whether such a technique would lead to clinical action in the foreseeable future. Notwithstanding, the MDL values can be reduced considerably by use of more appropriate systems. Therefore, there are many avenues to investigate in order to improve the quantitative potential of cadmium *in vivo* XRF.

For the source-based system, factors such as price, availability, radioisotopic half-life, photoelectric cross-section, and energy of the principle gamma ray and emissions of other non-contributing gamma rays are to be considered when comparing the different desirable photon sources. The most obvious alternative sources are iodine-125 and

americium-241. The latter was briefly investigated in this study. The set up was made similar to the cadmium-109 source, hence standardising the geometrical factors.

From the spectra presented in figure 6.1 and figure 6.2, many differences were realised. First the throughput of the americium source is higher. This was expected, as both the source strength and the photoelectric cross section for the cadmium K X-rays are higher for the americium.

Secondly, there was an apparent increase in the resolution. With these observed enhanced features, it is predicted that the use of an americium source should result in better sensitivity and MDL.

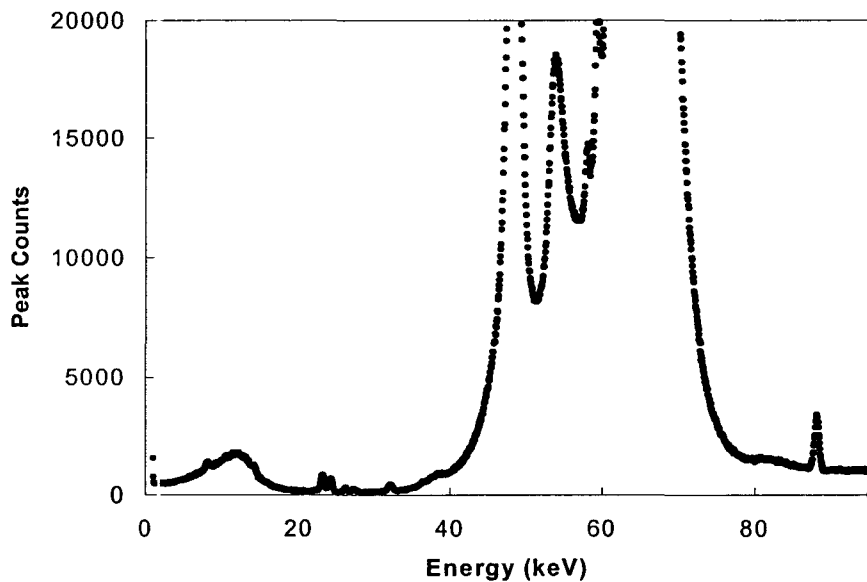


**Figure 6.1:** Spectrum detected during a 2000s (live time) measurement of the 170 ppm cadmium-doped plaster of Paris phantom (no wax overlay) using the  $^{109}\text{Cd}$  source in a backscatter geometry sample to detector distance, 2 cm. Note the coherent peak at 88.035 keV.

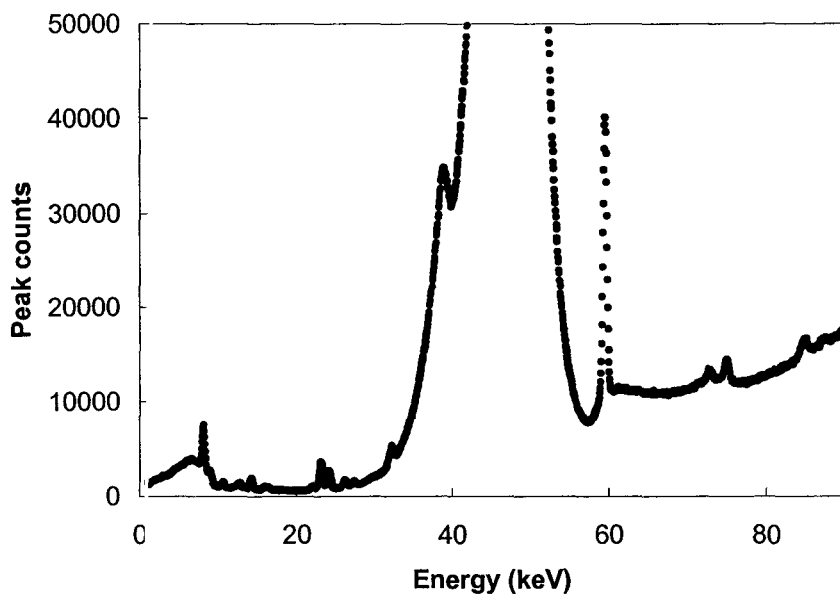


**Figure 6-2:** Spectrum detected during a 2000s (live time) measurement of the 170 ppm cadmium-doped plaster of Paris phantom (no wax overlay) using the  $^{241}\text{Am}$  source in a backscatter geometry sample to detector distance, 2 cm. Note the coherent peak at 59.5 keV

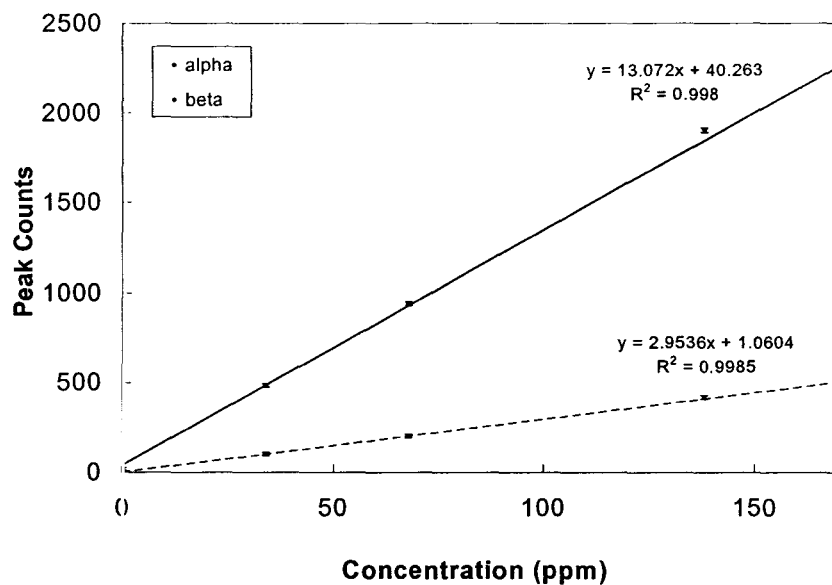


**Figure 6.3:** Variation of the fitted peak amplitudes for the americium peaks for the cylindrical set of phantoms placed 2 cm away from source.

From this americium calibration graph, the slope is steeper than the corresponding cadmium-109 source; hence a better MDL is noticed. For the bare plaster of Paris phantom measurements, the alpha and beta MDL were found to be  $1.081 \pm 0.326$  ppm and  $5.493 \pm 2.048$  ppm respectively. Hence, the uncertainties in the X-ray for the blank phantom spectrum predicted a combined MDL of 1.061 ppm compared to 1.689 ppm for the cadmium source based technique. This represented a 33% reduction in the determined MDL when an americium source was used. Interestingly, the dose emitted from the americium source was 3 mrad, which represented a dose that was 10 times the dose emitted from the cadmium source. Thus when the MDL was normalised to dose, it was found that the normalised MDL was approximately 2 times that of the cadmium source.

From the preliminary analysis of the americium source, it was evident that the use of this as an alternative to cadmium should enhance the signal, but whether or not a better estimated MDL is obtained is questionable. Actually, this source has been used earlier, for kidney-cadmium studies (Ahlgren and Mattsson, 1981; Christoffersson *et al.*, 1987; Nilsson *et al.*, 1990 and more recently MacKenzie, 1997) with several different geometries.

There is also the potential for the use of iodine as a source because it has a very large photoelectric cross-section for the cadmium K X-rays. However, its availability is questionable as it is a very volatile liquid, making transportation and storage a problem. Its half-life is short compared to cadmium; hence replacement cost must be considered. Thus, rendering this source less favourable.

For the polarised system, mono-energetic polarised photon beams can be generated through the use of synchrotron radiation, since synchrotrons can produce intense photon beams by accelerating electrons contained in a storage ring. Principally, when the electrons undergo centripetal acceleration, they emit electromagnetic radiation as they are deflected around the ring by bending magnets. Until recently, the use of synchrotron was not a feasible option, as the energy was too low for the excitation of K shell X-rays from the toxic heavy metals. Fortunately, there are now facilities that have energetically feasible beamlines. Thus, a synchrotron can offer an interesting alternative, as a means of exciting the characteristic X-rays for *in vivo* XRF. Note that because beams emitted from a synchrotron are intense, well collimated, and highly linearly polarised, they may provide a better MDL estimate (O'Meara, 1999).

Alternatively, the use of direct tube output, appropriately filtered, may yield improved sensitivity. The gain in sensitivity may be achieved since the  $90^\circ$  geometric constraints would not apply here, hence the unacceptable high background under the X-rays of concern could be reduced by a change in geometric orientation. Swedish researchers (Nilsson *et al.*, 2000, Borjesson *et al.*, 2000) are currently investigating this technique, where the Fluorex system has been adopted.

### 6.3 New detection systems

While system sensitivity may be improved through the use of alternative photon sources, research into new detection systems may also enhance performance.

MacKenzie, (1997) showed that it is possible to effect a greater background reduction by replacing the conventional planar germanium detector with a large volume detector (the Loax from EG&G). This approach resulted in a very large gain in the peak to background ratio as desired.

Calorimetric research pursued by Silver *et al.* (1996) reported another advance in detection systems. Silver *et al.* demonstrated that a resolution of 7 eV over the energy range of 0.2 to 20 keV with 95% efficiency at 6 keV could be obtained by the use a microcalorimeter detector made of tin operated at 80 mK. Compared to the standard hyper-pure germanium crystal used for high-resolution photon detection, this represented a 20-fold increase in resolution. This technique was unavailable before, as calorimetric measurements were limited to intense radiation fields, since the temperature rise associated with ionising radiation was too small to be measured. It should be noted that miniature samples of material must be maintained at very low temperatures, if the sensitivity of such calorimetric methods is to be significantly improved (Knoll, 2000). But the operation of the system at these low temperatures results in poor efficiency. So to overcome this dilemma, superconducting materials that have high interaction cross sections at these energies should be used.

O' Meara, (1999) demonstrated that by replacing the tin samples investigated by Silver *et al.* with pure lead samples, microcalorimeters could be considered for radiation detection at higher photon energies of the order of 100 keV.

New systems involving the use of digital electronics replace the amplifier and analogue to digital converter (ADC) in the conventional approach since the ideal pulse should comprise of an exponentially rising edge, followed by a short duration peak, and finishing with an exponentially falling edge (Knoll, 2000). Theoretically, the typical output of an analogue amplifier is a Gaussian-shaped pulse, which does not model the peaks adequately, however these pulses can be modelled quite easily with digital electronics.

In 1998, Fleming. proposed that digital spectroscopy systems could be used to improve sensitivity, since the system has better energy resolution, and higher throughput rates. Fleming used 5 different combinations digital shaping parameters, and found that shaping parameters of 2.4  $\mu\text{s}$  and 1.2  $\mu\text{s}$  were optimal. This conclusion was based on the throughput and energy resolution considerations. The results of these findings are shown in table 6.1.

**Table 6.1: Relative peak uncertainty and resolution for coherent peak adapted from Fleming and Forbes, 2001.**

Rise time / flat top( $\mu\text{s}$ )	Tibia		Phantom	
	Relative peak uncertainty (%)	Resolution (eV)	Relative peak uncertainty (%)	Resolution (eV)
5.6/0.8	0.48	550	0.36	550
2.8/0.6	0.46	620	0.31	620
2.4/1.2	0.40	634	0.28	634
2.0/0.8	0.39	666	0.28	666
2.8/1.2	0.44	618	0.32	618

When these shaping parameters were used, there was a much more significant improvement in performance of the digital system compared to the analogue version. In addition, smaller relative uncertainties of the coherent peak were achieved by using digital electronics, hence better predicted MDLs. A 15% reduction in uncertainty was observed. This implied that the cadmium-109 backscatter lead system, which had an MDL of  $\sim 8 \mu\text{g/g}$  could be reduced by  $1 \mu\text{g/g}$  to  $7 \mu\text{g/g}$  for non-occupationally exposed group of males.

More recently, Bateman *et al.* (2000) studied the effect of different digital systems and found that the lead MDL could be further reduced. Bateman used systems such as the DSA, DSPEC, and DSPEC plus from EG&G Ortec (Oak Ridge, TN). It was demonstrated from this study that both digital systems represented an improvement. However, the performance of the DSA 2000 was superior to the DSPEC<sup>plus</sup> for bone-lead measurements resulting in greater reduction in MDL for that system. In practice, an improvement of 25 % can be achieved resulting in a reduction in the calculated MDL. Therefore these tests indicate that the use of digital spectroscopy units could have profound improvement in the precision of measuring cadmium in bone.

Currently work is in progress at McMaster where the configuration of multi-detection systems is being examined. It is proposed that by the use of Monte Carlo simulation, 4 hyper-pure germanium detectors arranged in a  $2\pi$  geometry should lead to a much improved system. From this arrangement, it can be demonstrated that the system is capable of detecting 4 times the number of photons with excellent efficiency. Furthermore, the resolution improves from 700 eV to 550 eV over the energy range of

50–200 keV. This represented an overall prediction that the MDL may decrease by a factor of  $\sim 3$  (Nie, 2001).

Improved methods of calibration as well as correction methods for phantom impurities may also offer better estimates for MDL. Work by Todd, (2000) has shown that contamination can cause an underestimation in the *in vivo* concentrations by small amounts under normal operating conditions. Thus this could lead to inaccurate MDL determination hence by use of certain warranted refinements, these unforeseen errors could be circumvented.

#### **6.4 Computer Modeling Techniques**

Several authors have used the Monte Carlo method to model the source-excited XRF for heavy elements (Todd *et al.*, 1991; He *et al.*, 1993; Tartari *et al.*, 1993; Wallace, 1994; Ao *et al.*, 1997; O'Meara *et al.*, 1998). Objective in development of such a model was to optimise the system parameters for *in vivo* measurement of trace heavy elements using XRF. System parameters, which were optimised through the use of such codes, include the selection of excitation source, source phantom distance keeping with particular organ/tissue under consideration, detector size etc. Such codes facilitate the development of an optimised system without practical implementation, thus saving the costs and time. For example, the code developed by O'Meara *et al.* (1998) was modified to model the detectors in  $2\pi$  geometry instead of using a single detector. Although the modelled geometry assumed an "integral cryostat" for four detectors, the practicality for such an arrangement is questionable. The two greatest concerns being patient positioning and

system cost. These codes generally assume the ideal geometry for both the detector and the phantom or organ. Especially after the availability of VIP-MAN, the use of cylindrical or rectangular geometry to represent man in codes is also questionable. The use of a bare detector model is also an important source of error as it is particularly emphasised in literature that bare detector response differs significantly from the experimentally observed response at lower energies. In particular, where such sort of uncertainty is tolerable, detector response may either be calculated by some analytical expression or experimentally obtained response function, thus making the code faster. The literature has demonstrated that achieving the same response function as obtained from experiment is difficult because of the design limitations associated with the construction of such arrangements, as governed by the manufacturer proprietary rights. The time required for the central processing unit (CPU) to run such codes is also a concern. Most of the time, such codes do not incorporate variance reduction techniques, which makes running CPU time a bit higher. However, these codes may be preferred over the professional Monte Carlo codes like MCNP, EGS, GEANT, CYLTRAN since such codes were specifically developed for a particular phenomenon. However, comparisons with professional codes are required because these codes have more enhanced features like variance reduction techniques, proper geometry modelling etc. The adaptation of such codes for this particular application in *in vivo* XRF will not only make it simpler to model the geometry but a reduction in CPU running time may be also achieved. Though the benefit of using such dependent application codes is that input preparation is rather simpler in comparison to professional codes.

Most of these application codes preferentially model the radiation transport phenomenon starting from the source to the phantom and consequently the detector. There are models available which can simulate the electronic part of the system. As these models become more readily available, the development of an overall model that can incorporate the whole phenomenon starting from the source to the electronic part of the system, which can contribute to system optimisation, does not seem unfeasible. Thus, should be considered.

## **6.5 Final remarks**

MDL estimates from this research were of the order of 3.5 ppm for a bone cadmium measurement with approximately 2-5 mm soft tissue matrix. However, with further investigations as mentioned in this chapter, a five fold reduction in MDL could be accomplished for a fully optimised system. Thus, these improvements could serve to enhance the initial irradiation modality that exists in this pilot study and hence establish a comfortable environment for human subjects to be measured. Therefore, the future prospects of XRF being adopted as a clinical cadmium measurement tool are excellent.

## References

- Ahlgren L, Haeger-Aronsen B, Mattsson S, Schütz A, *In Vivo Determination of Lead in the Skeleton after Occupational Exposure to Lead*, Br. J. Ind. Med. **37** 109-113 (1980).
- Ahlgren L, Mattsson S, *Cadmium in Man Measured In Vivo by X-Ray Fluorescence Analysis*, Physics in Medicine and Biology. **26(1)** 19-26 (1981).
- Ao Q, Lee S. H, and Gardner R. P, *Optimization of In Vivo X-ray Fluorescence Analysis Methods for Bone Lead by Simulation with the Monte Carlo Code CEARXRF*, Appl. Radiat. Isot. **48** 1413-1423 (1997).
- Arnold M. L, *Development of an Accelerator Based System for In Vivo Neutron Activation Analysis Measurements of Manganese in Humans*, PhD Thesis, McMaster University, (2001).
- Barkla C. G, *Polarised Röntgen Radiation*, Phil. Trans. Roy. Soc. **A204** 467-479 (1905).
- Bateman S. N, *Using Digital Spectroscopy in the X-Ray Fluorescence Measurement of Lead and Mercury*, MSc Thesis, McMaster University, (2000).
- Bateman S. N, Pejovic-Milic A, Stronach I. M, McNeill F. E, Chettle D. R, *Performance Appraisals of Digital Spectroscopy Systems for the Measurement of Bone Lead*, Appl Radiat Isot. **53(4-5)** 647-650 (2000).
- Berger M, *XCOM: Photon Cross Sections on a Personal Computer*, Version 1.2 (1987).  
[http://dental.senzoku.showau.ac.jp/dent/radiol/Prometheus/Berger&Hubbell/B&H\\_xcom\\_text.html](http://dental.senzoku.showau.ac.jp/dent/radiol/Prometheus/Berger&Hubbell/B&H_xcom_text.html).
- Bevington P. R, *Data Reduction and Error Analysis for the Physical Sciences*, 2<sup>nd</sup> Ed. Imprint New York: McGraw-Hill, (1992).
- Börjesson J, *Studies of Cadmium, Mercury, and Lead in Man: The Value of X-Ray Fluorescence Measurements In Vivo*, Ph.D. Thesis, Lund University, Sweden, (1996).
- Börjesson J, Olsson M, Mattsson S, *Feasibility of a Fluorescent X-Ray Source for In Vivo X-Ray Fluorescence Measurements of Kidney and Liver Cadmium*, Ann N Y Acad Sci. **904** 255-258 (2000).

- Börjesson J, Mattsson S, *Toxicology, In Vivo X-Ray Fluorescence for the Assessment of Heavy Metal Concentrations in Man*, Appl Radiat Isot. **46(6-7)** 571-576 (1995).
- Buchet J, Lauwerys R, Roels H, Bernard A, Bruaux P, Claeys F, Ducoffre G, de Plaen P, Staessen J, Amery A, *Renal Effects of Cadmium Body Burden of the General Population*, Lancet. **22, 336(8717)** 699-702 (1990).
- Canberra, *Germanium Detectors: User's Manual*. Canberra Industries Inc, Meriden CT (1991).
- Chettle D. R, Scott M. C, Somervaille L. J, *Lead in Bone: Sampling and Quantitation using K X-Rays Excited By <sup>109</sup>Cd*, Environ Health Perspect. **91** 49-55 (1991).
- Chettle D. R, and Fremlin J. H, *Techniques of In Vivo Neutron Activation Analysis*, Physics in Medicine and Biology. **29** 1011-1143 (1984).
- Christoffersson J, Mattsson S, *Polarized X-Rays in X-Ray Fluorescence Analysis for Improved In Vivo Detectability of Cadmium in Man*, Physics in Medicine and Biology. **23** 1135-1144 (1983).
- Christoffersson J, Welinder H, Spang G, Mattsson S, Skerfving S, *Cadmium Concentration in the Kidney Cortex of Occupationally Exposed Workers Measured in Vivo using X-Ray Fluorescence Analysis*, Environ Res. **42(2)** 489-499 (1987)
- Czauderna M, Rochalska M, *Effect of Cd on Tissue Levels of Se, Zn, Fe, Co and Rb*, Int J Rad Appl Instrum [A], **40(2)** 177-181 (1989).
- Ellis K, Morgan W, Yasumura S, Vartsky D, Zani I, Cohn S, *In Vivo Measurement of Cadmium in an Occupationally Exposed Population*, Am J Ind Med. **22(1)** 117-124 (1977).
- Firestone R, Bagling C, Frank-Chu S, *Table of Isotopes*, 8<sup>th</sup> Ed. John Wiley and Sons, (1996).
- Fleming D, *Human Lead Metabolism: Chronic Exposure, Bone Lead and Physiological Models*. Ph.D. Thesis, McMaster University (1998).
- Fleming D, *Lead Speciation and Occupational Exposure*, Environ Health Perspect. **106(9)** 531 (1998).
- Fleming D, Forbes T, *Calibration and Characterisation of a Digital X-Ray Fluorescence Bone Lead System*, Appl. Radiat. Isot. **55** 527-532 (2001).

- Friberg L, Piscator M, Nordberg G, Kjellstrom T, *Cadmium in the Environment*, 2<sup>nd</sup> Ed. Boca Raton: CRC Press, (1974).
- Franklin D, Armstrong R, Chettle D, Scott M, *An Improved In Vivo Neutron Activation System for Measuring Kidney Cadmium*, *Physics in Medicine and Biology*. **35(10)** 1397-1408 (1990).
- Gompertz D, Chettle D, Fletcher J, Mason H, Perkins J, Scott M, Smith N, Topping M, Blindt M, *Renal Dysfunction in Cadmium Smelters: Relation to In Vivo Liver and Kidney Cadmium Concentrations*, *Lancet*. **28; 1(8335)** 1185-1187 (1983).
- He T, Gardner R, and Verghese K, *The Monte-Carlo Library Least-Squares Approach for Energy Dispersive X-Ray Fluorescence Analysis*, *Appl. Radiat. Isot.* **44** 1381-1388 (1993).
- ICRP Publication 30, Part 1, *Annals of the ICRP*, Vol 2, Nos. 3 & 4. *Limits for Intakes of Radionuclides by Workers*, Pergamon Press, Oxford, U.K (1979).
- Kaufman L. and Camp D, *Polarised Radiation for X-Ray Fluorescence Analysis*. *Adv. X-ray Anal*, **18**, 247-258 (1974).
- Kaufman L, *Techniques for In Vitro Fluorescent Excitation Analysis of Stable Traces*. In *Medical Applications of Fluorescent Excitation Analysis*, CRC Press 91-113 (1979).
- Kjellstrom T, Nordberg G, *A Kinetic Model of Cadmium Metabolism in the Human Being*, *Environ Res.* **6(1-3)** 248-269 (1978).
- Knoll G, *Radiation Detection and Measurement*, 2<sup>nd</sup> Ed. John Wiley & Sons Inc: New York (2000).
- Laird E. E, *Factors Affecting In Vivo x-Ray Fluorescence Measurements of Lead in Bone*, Ph.D. Thesis, University of Birmingham, Birmingham, U.K. (1983).
- Lauwerys R, Amery A, Bernard A, Bruaux P, Buchet J, Claeys F, De Plaen P, Ducoffre, Fagard R, Lijnen P, *Health Effects of Environmental Exposure to Cadmium: Objectives, Design and Organization of the Cadmibel Study: A Cross-Sectional Morbidity Study Carried Out in Belgium from 1985 to 1989*. *Environ Health Perspect.* **87** 283-289 (1990).
- Lauwerys R, Bernard A, Buchet J, Roels H, Bruaux P, Claeys F, Ducoffre G, De Plaen P, Staessen J, Amery A, *Does Environmental Exposure to Cadmium Represent A Health Risk? Conclusions from the Cadmibel Study*, *Acta Clin Belg* **46(4)** 219-225 (1991)

- Lederer C. M, Shirley V. S, *Table of Isotopes*, 7<sup>th</sup> Ed. John Wiley & Sons Inc, New York (1978).
- Mackenzie I. K, *A Simple System for XRF of Cadmium in Kidneys* University of Guelph, Guelph, Canada (1997).
- Mattsson S, Scott M, *In Vivo Elemental Analysis using X-Ray Fluorescence Techniques and Applications* (1990). 2<sup>nd</sup> International Workshop XRF and PIXE in Life Sciences, Capri, June 1989.
- McLellan J, Thomas B, Fremlin J, Harvey T, *Cadmium-Its In Vivo Detection in Man*, *Physics in Medicine and Biology*. **20(1)** 88-95 (1975).
- McNeill F. E, *The In Vivo Measurement of Trace Toxic Elements*, CCPM, London, Ontario, (1998).
- McNeill F, Stokes L, Chettle D, Kaye W, *Factors Affecting In Vivo Measurement Precision and Accuracy of <sup>109</sup>Cd K X-Ray Fluorescence Measurements*, *Physics in Medicine and Biology*. **44(9)** 2263-2273 (1999).
- McNeill F. E, *Personal Communication*, Medical Physics & Applied Radiation Sciences Unit. Department of Physics and Astronomy, McMaster University, (2001).
- Nie L, *The Improvement of the In Vivo XRF Lead Measurement System*, MSc Thesis, McMaster University, (In preparation, 2001).
- Nilsson U, Ahlgren L, Christoffersson J, Mattsson S, *Further Improvements of XRF Analysis of Cadmium In Vivo*, *Basic Life Sci*. **55** 297-301 (1990).
- Nilsson U, Schutz A, Bensryd I, Nilsson A, Skerfving S, Mattsson S, *Cadmium Levels in Kidney Cortex in Swedish Farmers*, *Environ Res*. **82(1)** 53-59 (2000).
- Nordberg G, Piscator M, Nordberg M, *On the Distribution of Cadmium in Blood*, *Acta Pharmacol Toxicol* (Copenh). **30(3)** 289-295 (1971).
- O'Meara J. M, *Measuring Lead, Mercury, and Uranium by In Vivo X-Ray Fluorescence*, PhD Thesis, McMaster University, (1999).
- O'Meara J. M, Chettle D. R, McNeill F. E, Prestwich W. V, and Svensson C. E, *Monte Carlo Simulation of Source-Excited In Vivo X-Ray Fluorescence Measurements of Heavy Metals*, *Physics in Medicine and Biology*. **43** 1413-1428 (1998a).
- O'Meara J. M, Chettle D. R, McNeill F. E, and Webber C. E, *The Feasibility of Measuring Bone Uranium Concentrations In Vivo using Source Excited K X-Ray Fluorescence*. *Physics in Medicine and Biology*. **42** 1109-1120 (1997).

- Pejovic-Milic A, *An Accelerator Based In Vivo Measurement of Aluminium in Human Bone by Neutron Activation Analysis*, MSc Thesis, McMaster University, (1998).
- Pejovic-Milic A, Arnold M, McNeill F, and Chettle D, *Monte Carlo Design Study for In Vivo Bone Aluminium Measurement using a Low Energy Accelerator Beam*, Appl. Radiat. Isot. **53** 657-664 (2000).
- Piscator M, *Proteinuria in Chronic Cadmium Poisoning. IV. Gel Filtration and Ion Exchange Chromatography of Urinary Proteins from Cadmium Workers*. Arch Environ Health, **2(3)** 345-359 (1966).
- Roels H, Lauwerys R, Buchet J, Bernard A, Vos A, Oversteyns M, *Health Significance of Cadmium Induced Renal Dysfunction: A Five Year Follow Up*, Br J Ind Med. **46(11)** 755-764 (1989).
- Sartor F, Rondia D, Claeys F, Staessen J, Lauwerys R, Bernard A, Buchet J, Roels H, Bruaux P, Ducoffre G, *Impact of Environmental Cadmium Pollution on Cadmium Exposure and Body Burden*, Arch Environ Health. **47(5)** 347-353 (1992).
- Silver E, LeGros M, Madden N, Beeman J, and Haller E, *High-Resolution, Broad-Band Microcalorimeters for X-Ray Microanalysis*, X-Ray Spectrom, **25** 115-122 (1996).
- Somervaille L. J, Chettle D. R, and Scott M. C, *In Vivo Measurement of Lead in Bone using X-Ray Fluorescence*, Physics in Medicine and Biology, **30** 929-943 (1985).
- Staessen J, Amery A, Bernard A, Bruaux P, Buchet J, Claeys F, De Plaen P, Ducoffre G, Fagard R, Lauwerys R, *Effects of Exposure to Cadmium on Calcium Metabolism: A Population Study*, Br J Ind Med. **48(10)** 710-714 (1991).
- Tartari A, Fernandez J, Casnati E, Baraldi C, Felsteiner J, *Edxrs Modelling for In Vivo Trace Element Analysis by using the Shape Code*. X-Ray Spectrom, **22** 323-327 (1993).
- Todd A. C, *Coherent Scattering and Matrix Correction in Bone-Lead Measurements*, Physics in Medicine and Biology. **45(7)** 1953-1963 (2000).
- Todd A. C, Chettle D. R, Scott M. C. and Somervaille L. J, *Monte Carlo Modelling of In Vivo X-Ray Fluorescence of Lead in the Kidney*, Physics in Medicine and Biology. **36** 439-448 (1991).

- Todd A. C, McNeill F. E, Palethorpe J. E, Peach D. E, Chettle D. R, Tobin M. J, Strosko S. J, Rosen J. C, *In Vivo X-Ray Fluorescence of Lead in Bone using K X-Ray Excitation with <sup>109</sup>Cd Sources: Radiation Dosimetry Studies*, Environ Res. **57(2)** 117-132 (1992).
- Vartsky D, Ellis KJ, Chen NS, Cohn SH, *A Facility for In Vivo Measurement of Kidney and Liver Cadmium by Neutron Capture Prompt Gamma Ray Analysis*, Physics in Medicine and Biology. **22(6)** 1085-1096 (1977).
- Wallace J. D, *The Monte Carlo Modelling of In Vivo X-Ray Fluorescence Measurement of Lead in Tissue*, Physics in Medicine and Biology. **39** 1745-1756 (1994).
- Webb M, *Cadmium*, Br Med Bull, **31(3)** 246-250 (1975).

## Appendix

- Program used for the 9 parameter fitting

```

INCLUDE 'FGRAPH.FI'
CHARACTER*20 FNAM
CHARACTER*35 OUT1,OUT2,OUT3,SPECTRA(20)
DIMENSION PA1(15),AC1(15),AB1(15),ADEV(15),CDEV(15),
1 BDEV(15),KNAM(8),NAMES(100,3),IH(2),NMFUL(8),NMRES(8)
DATA AA1/15*0./
DATA AC1/15*0./
DATA AB1/15*0./
DATA KNAM(1),KNAM(2),KNAM(6),KNAM(7)/2HLD,2HO:,2H.D,2HAT/
DATA NMFUL(1),NMFUL(2),NMFUL(6),NMFUL(7)/2HLD,2HO:,2H.F,2HUL/
DATA NMRES(1),NMRES(2),NMRES(6),NMRES(7)/2HLD,2HO:,2H.R,2HES/
KNAM(8)=0
NMFUL(8)=0
NMRES(8)=0

C
C      THIS IS AN ADAPTATION OF THE PROGRAM JJFIT WRITTEN
C      BY J.JOWETT FOR THE HP COMPUTER IN THE RADIATION CENTRE
C
C      IT IS A GENERALISED PROGRAM TO FIT UP TO 9 INDEPENDENT
C      PARAMETERS TO UP TO 100 DATA POINTS
C
C      THE FUNCTION IS DEFINED IN ROUTINES 'FUNCT' AND 'FDERV'
C      THESE SHOULD BE SET BY THE USER
C
C      THE PROGRAM CAN TAKE DATA FROM EITHER A FILE OR THE VDU
C
C      MODIFICATION RECORD:
C      ORIGINAL PROGRAM (JJFIT):           JJ
C      GENERALISATION TO DISTRIBUTED SYSTEM: JGO
C      CALC. OF COVARIANCE MATRIX:        DRW
C      ADAPTED FOR PDP11/23:              JSP
C
$DEBUG
CONTINUE
2036  FORMAT(1X,'for floating width CADMIUM analysis')
      WRITE(6,2036)
2038  FORMAT(1X,'State the # of parameters to be fitted (<15)')
      WRITE(6,2036)
      READ(5,*)NTA
      WRITE(6,2042)
2042  FORMAT(1X,'Peak AMPLITUDES and their ERRORS will be written to
',/,
1 'DISC. However, if you want the more complete output to go to
',/,

```

```

1 'the disc type "1", otherwise, output will go to the PRINTER')
  READ(5,*)LUTEST
  IF(LUTEST.EQ.1)GO TO 2047
2047 LU=2
  WRITE(*,2049)
2049 FORMAT(1X,'All the results from this analysis program will be
w',/,
1 'ritten to the DISK.')
  WRITE(*,2052)
2052 FORMAT(' Please ENTER the name of the output FILE (including
th',/,
1 'e path), which is to include the Peak AMPLITUDES, their
E',/,
1 'RRORS and the CADMIUM concentrations.
1 eg. C:\CdXRF.res')
  WRITE(*,2056)
2056 FORMAT(1X,'nb: The name of the file can have 35 characters
(inc',/,
1 'luding the path).',/,
1 ' This file MUST NOT already exist.')
  READ(5,'(A)') OUT1
  WRITE(*,*)
  WRITE(*,2061)
2061 FORMAT(1X,'Please ENTER the name of the output FILE (including
',/,
1 'the path), which is to contain the more complete output.
',/,
1 'ie. The final PARAMETERS of the FIT.
1 eg. C:\CDXRF.ful')
  READ(5,'(A)') OUT2
  WRITE(*,*)
  WRITE(*,*)
  WRITE(*,2068)
2068 FORMAT(' Please ENTER the name of the output FILE (including
th',/,
1 'e path), which is to include ONLY the CADMIUM
concentrati',/,
1 'ons, and their ERRORS.
1 eg. C:\CdXRF.dat')
  READ(5,'(A)') OUT3
  WRITE(*,*)

! Open OUT1 as unit #3, OUT2 as unit #7, and OUT3 as unit #8
!
OPEN(UNIT=3, FILE=OUT1, STATUS='NEW')
OPEN(UNIT=7, FILE=OUT2, STATUS='NEW')
OPEN(UNIT=8, FILE=OUT3, STATUS='NEW')
!
! Write name of output files to top of OUT1, and OUT2:

WRITE(3,2082) OUT1
WRITE(7,2082) OUT2
2082 FORMAT(1X,'Output Filename:',A35,/)

```

```

2085 WRITE(6,2086)
2086 FORMAT(/' First GUESS at A(I) ')
C
C A=FIRST GUESS TO PARAMETERS
C
WRITE(6,2036)
2089 DO 2093 I=1,NTA
WRITE(6,2091) I
2091 FORMAT(' A(',I2,')?')
READ(5,*) AA1(I)
2093 CONTINUE
WRITE(6,2095)
2095 FORMAT(1X,'Enter the # of CHANNELS and START CHANNEL')
READ(5,*) NPTSA,NSTA
2098 FORMAT(132('*'))
WRITE(7,2100)
2100 FORMAT(' Non-Linear Least Squares Fit (using Marquardt method')
WRITE(7,2102)
2102 FORMAT(1X,'CADMIUM analysis')
WRITE(7,2104) NPTSA,NSTA
2104 FORMAT(1X,I3,'Channels STARTING in channel',I3)
NTOPA=NPTSA+NSTA-1
DO 2108 I=1,NTA
ADEV(I)=0.
2108 CONTINUE
WRITE(6,2110)
2110 FORMAT(1X,'How many PARAMETERS do you want fitted over a
restr',/,
1 ' icted RANGE?')
WRITE(6,2036)
READ(5,*) NRA
IF(NRA.EQ.0) GO TO 2131
WRITE(6,2116)
2116 FORMAT(1X,'A(I)+/-DEV(I)', ' eg. 1 5,')
DO 2123 I=1,NRA
WRITE(6,2119)
2119 FORMAT(1X,'Enter I, DEV(I)')
READ(5,*) IRES,ADEV(IRES)
WRITE(7,2122) IRES,AA1(IRES),ADEV(IRES)
2122 FORMAT(1X,'A(',I2,') = ',G12.5,'+/-',G12.5)
2123 CONTINUE

WRITE(6,2126)
2126 FORMAT(1X,'Enter 2 Random Numbers')
READ(5,*) IH(1),IH(2)
WRITE(7,2129) IH(1),IH(2)
2129 FORMAT(1X,'Random number entry points.',I5,1X,I5)
2130 WRITE(7,2098)
2131 WRITE(6,2132)
2132 FORMAT(1X,'Do you want to plot out fit to each REGION?',
1 ' If YES, type "1";', ' If NO, type "0".')
READ(5,*) ITEST
WRITE(6,2135)

```

```

2135  FORMAT(1X,'State how many spectra are to be ANALYSED?')
      READ(5,*)NNAM
      DO 2147 NM=1,NNAM
      WRITE(6,2139)
2139  FORMAT(1X,'Enter the spectra FILE NAME, eg. 170ppm.txt')
      READ(5,'(A)') SPECTRA(NM)
      WRITE(6,2142)
2142  FORMAT(1X,'Enter CHANNEL OFFSET for Cd Peak in spectra')
      READ(5,*)AFSET
      WRITE(6,2145)
2145  FORMAT(1X,'Enter the GAIN used')
      READ(5,*)G
2147  CONTINUE
      DO 2162 NM=1,NNAM
      DO 2152 I=1,3
      K=I+2
      KNAM(K)=NAMES(NM,I)
2152  CONTINUE
      IFLAG=1
      NK=NM
      SPTEST=0.0
      CALL FIT(NTA,NPTSA,NSTA,NTOPA,NRA,AA1,ADEV,IH,ITEST,IFLAG,
1      KNAM,CAMP,CPOS,LU,NK,NNAM,SPTEST,SPECTRA,AFSET,G)
      IFLAG=2
      CAMP = 0.0
      CPOS = 0.0
      SPTEST=1.0
2162  CONTINUE
      WRITE(6,2164)
2164  FORMAT(1X,'TYPE 0 To stop'/6X,'1 For same FIT to NEW spectra
DA',/,
1  'TA'/6X, 2 For NEW FIT (new parameter values)')
      READ(5,*)NTEST
      IF(NTEST-1) 2168,2131,2085
2168  CLOSE(UNIT=3,STATUS='KEEP')
      CLOSE(UNIT=7,STATUS='KEEP')
      CLOSE(UNIT=8,STATUS='KEEP')
      END

      SUBROUTINE MATIN(ARRAY,NORDER,DET)
      DOUBLE PRECISION ARRAY,AMAX,SAVE
      DIMENSION ARRAY(15,15),IK(15),JK(15)
2176  DET=1.
2177  DO 2225 K=1,NORDER
C
C      FIND LARGEST ELEMENT ARRAY(I,J) IN REST OF MATRIX
C
      AMAX=0.
2182  DO 2188 I=K,NORDER
      DO 2188 J=K,NORDER
2184  IF(DABS(AMAX)-DABS(ARRAY(I,J))) 2185,2185,2188
2185  AMAX=ARRAY(I,J)
      IK(K)=I

```

```

                JK(K)=J
2188      CONTINUE
C
C      INTERCHANGE ROWS AND COLUMNS TO PUT AMAX IN ARRAY(K,K)
C
2192      IF (AMAX) 2195,2193,2195
2193      DET=0.
                GOTO 2244
2195      I=IK(K)
                IF (I-K) 2182,2201,2197
2197      DO 2200 J=1,NORDER
                SAVE=ARRAY(K,J)
                ARRAY(K,J)=ARRAY(I,J)
2200      ARRAY(I,J)=-SAVE
2201      J=JK(K)
                IF (J-K) 2182,2210,2203
2203      DO 2206 I=1,NORDER
                SAVE=ARRAY(I,K)
                ARRAY(I,K)=ARRAY(I,J)
2206      ARRAY(I,J)=-SAVE
C
C      ACCUMULATE ELEMENTS OF INVERSE MATRIX
C
2210      DO 2213 J=1,NORDER
                IF (I-K) 2212,2213,2212
2212      ARRAY(I,K)=-ARRAY(I,K)/AMAX
2213      CONTINUE
2214      DO 2219 J=1,NORDER
                DO 2219 I=1,NORDER
                IF (I-K) 2217,2219,2217
2217      IF (J-K) 2218,2219,2218
2218      ARRAY(I,J)=ARRAY(I,J)+ARRAY(I,K)*ARRAY(K,J)
2219      CONTINUE
2220      DO 2223 I=1,NORDER
                IF (J-K) 2222,2223,2222
2222      ARRAY(K,I)=ARRAY(K,J)/AMAX
2223      CONTINUE
                ARRAY(K,K)=1./AMAX
2225      DET=DET*AMAX
C
C      RESTORE ORDERING OF MATRIX
C
2229      DO 2243 I=1,NORDER
                K=NORDER-L+1
                J=IK(K)
                IF (J-K) 2237,2237,2233
2233      DO 2236 I=1,NORDER
                SAVE=ARRAY(I,K)
                ARRAY(I,K)=-ARRAY(I,J)
2236      ARRAY(I,J)=SAVE
2237      I=JK(K)
                IF (I-K) 2243,2243,2239
2239      DO 2242 J=1,NORDER

```

```

        SAVE=ARRAY (K, J)
        ARRAY (K, J) = -ARRAY (I, J)
2242     ARRAY (I, J) = SAVE
2243     CONTINUE
2244     RETURN
        END

        REAL FUNCTION FCHIS (Y, NST, NTOP, NFREE, YFIT)
        DIMENSION Y (4097), YFIT (2300)
2249     CHISQ = 0.
C
C     ACCUMULATE CHI SQUARE
C
2253     DO 2188 I=NST, NTOP
2188     CHISQ=CHISQ+ABS ((Y (I) -YFIT (I)) * (Y (I) -YFIT (I)) /YFIT (I))
C
C     DIVIDE BY NUMBER OF DEGREES OF FREEDOM
C
2192     FREE=NFREE
2193     FCHIS=CHISQ/FREE
2260     RETURN
        END

        SUBROUTINE FIT (NTERMS, NPTS, NST, NTOP, NR, A1, DEV, IH, ITEST, IFLAG,
1     KNAM, CAMP, CPOS, LU, NM, NNAM, SPTEST, SPECTRA, OFFSET, G)
        CHARACTER*20 FNAM, SPECTRA (20)
        INTEGER*4 SPEC, CH, CHFT
        REAL*8 TEMPY
        DIMENSION SPEC (33, 75)
        DOUBLE PRECISION ARRAY
        DIMENSION X (900), Y (900), YFIT (900), WEIGHT (2300), A (15), A1 (15),
1     B (15), BETA (15), ALPHA (15, 15), ARRAY (15, 15), DERIV (15), DEV (15),
1     SIGMAA (15), KNAM (8), IH (2), NMRES (8), NMFUL (8), XE (2300)
        DO 2275 I=1, NTERMS
        A (I) =A1 (I)
2275     CONTINUE
        FNAM=SPECTRA (NM)
        OPEN (1, FILE=SPECTRA (NM))
C     READ (1, 330) (Y (I), I=1, 435)
        DO 2281 I=1, 600
        READ (1, *) X (I), XE (I), Y (I)
2281     CONTINUE
        CH=1

2284     CONTINUE
        CHFT=1
        DO 2290 I=OFFSET, 600
        TEMPY=Y (I)
        Y (CHFT) =TEMPY
        CHFT=CHFT+1
2290     CONTINUE
        CLOSE (UNIT=1, STATUS='KEEP')
        WRITE (7, 2293) FNAM

```

```

2293  FORMAT(///,1X,'DATA FILE:-',2X,A)
      WRITE(7,2295)
2295  FORMAT(/,1X,'alpha 1 + alpha 2')
2296  DO 2298 I=NST,NTOP
      X(I)=I
2298  CONTINUE
      FLAMDA=0.001
      WRITE(7,2301) (I,I=1,NTERMS)
2301  FORMAT(3X,'CHI SQ',3X,9(4X,'A(',I1,')',4X),3X,'A(',I2,')')
2302  NFREE=NPTS-NTERMS
      IF(NFREE) 2304,2304,2253
2304  CHISQR=0.
      GOTO 2437
2253  DO 2308 I=NST,NTOP
      YFIT(I)=FNA(X(I),A,G)
2308  CONTINUE
2309  CHISQ1=FCHIS(Y,NST,NTOP,NFREE,YFIT)
      WRITE(6,2311) (KNAM(I),I=3,5)
2311  FORMAT(1X,'analysing ',3A2)
      WRITE(6,2260) NM,NNAM
2260  FORMAT(1X,'number ',I3,' of ',I3,' files')
      WRITE(7,2315) CHISQ1, (A(I),I=1,NTERMS)
2315  FORMAT(11(1X,G11.4))
C
C      EVALUATE WEIGHTS
C
      DO 2188 I=NST,NTOP
2320  IF(Y(I)) 2323,2325,2184
2184  WEIGHT(I)=1./Y(I)
      GOTO 2188
2323  WEIGHT(I)=1./(-Y(I))
      GOTO 2188
2325  WEIGHT(I)=1.
      GOTO 2188
2188  CONTINUE
C
C      EVALUATE ALPHA AND BETA MATRICES
C
2192  DO 2334 J=1,NTERMS
      BETA(J)=0.
      DO 2334 K=1,J
2334  ALPHA(J,K)=0.
2195  DO 2200 I=NST,NTOP
      CALL FDA(X(I),A,DERIV,G)
      DO 2339 J=1,NTERMS
      BETA(J)=BETA(J)+WEIGHT(I)*(Y(I)-FNA(X(I),A,G))*DERIV(J)
2339  CONTINUE
      DO 2344 J=1,NTERMS
      DO 2343 K=1,J
      ALPHA(J,K)=ALPHA(J,K)+WEIGHT(I)*DERIV(J)*DERIV(K)
2343  CONTINUE
2344  CONTINUE
2200  CONTINUE

```

```

2201 DO 2203 J=1, NTERMS
      DO 2203 K=1, J
2203 ALPHA (K, J) =ALPHA (J, K)
C
C EVALUATE CHI SQUARE AT STARTING POINT
C
2210 DO 2354 I=NST, NTOP
      YFIT (I) =FNA (X (I) , A, G)
2354 CONTINUE
2212 CHISQ1=FCHIS (Y, NST, NTOP, NFREE, YFIT)
C
C INVERT MODIFIED CURVATURE MATRIX TO FIND NEW PARAMETERS
C
      WRITE (6, 2242) CHISQ1, (A (I) , I=1, NTERMS)
2242 FORMAT (1X, 'CHI SQ =', (1X, G12.5) ,/, (1X, G12.5) ,/, (1X, G12.5) ,/,
1 (1X, G12.5) ,/, (1X, G12.5) ,/, (1X, G12.5) ,/, (1X, G12.5) ,/, (1X, G12.5) ,/,
1 ,/, (1X, G12.5) ,/, (1X, G12.5) ,/, (1X, G12.5) )
2214 DO 2217 J=1, NTERMS
      DO 2363 K=1, NTERMS
2363 ARRAY (J, K) =DBLE (ALPHA (J, K) /DSQRT (ALPHA (J, J) ) /DSQRT (ALPHA (K, K) ) )
2217 ARRAY (J, J) =DBLE (1. +FLAMDA)
2219 CALL MATIN (ARRAY, NTERMS, DET)
2220 DO 2369 J=1, NTERMS
      B (J) =A (J)
      DO 2369 K=1, NTERMS
2369 B (J) =B (J) +BETA (K) *SNGL (ARRAY (J, K) ) /DSQRT (ALPHA (J, J) )
1 /DSQRT (ALPHA (K, K) )

      IF (NR.EQ.0) GO TO 2383
      DO 2379 J=1, NTERMS
      IF (DEV (J) .EQ.0) GO TO 2379
      IF (ABS (B (J) -A1 (J)) .LT.DEV (J)) GO TO 2379
      call seed (ih (1))
      CALL RANDOM (YFL)
      B (J) = (YFL-.5) *2.*DEV (J) +A1 (J)
2379 CONTINUE
C
C IF CHI SQUARE INCREASES, INCREASE FLAMDA AND TRY AGAIN
C
2383 DO 2385 I=NST, NTOP
      YFIT (I) =FNA (X (I) , B, G)
2385 CONTINUE
2386 CHISQR=FCHIS (Y, NST, NTOP, NFREE, YFIT)
      CHIDIF=CHISQ1-CHISQR
      IF (CHIDIF) 2389, 2229, 2229
2389 IF (ABS (CHIDIF) -1.E-03) 3400, 3400, 2390
2390 FLAMDA=10.*FLAMDA
      GOTO 2214
C
C EVALUATE PARAMETERS AND TEST FOR CONVERGENCE
C
2229 FLAMDA=FLAMDA/10.
      DO 2398 J=1, NTERMS

```

```

A(J) = B(J)
2398 CONTINUE
IF (CHIDIF - .001*CHISQR) 2401, 2192, 2192
3400 CHISQR=CHISQ1
2401 WRITE (7, 2315) CHISQR, (A(I), I=1, NTERMS)
CALL MATIN (ARRAY, NTERMS, DET)
FLAMDA = 0.001
DO 2406 J=1, NTERMS
ARRAY (J, J) = DBLE (1.+FLAMDA)
2406 CONTINUE
CALL MATIN (ARRAY, NTERMS, DET)
WRITE (3, 2420) (KNAM (I), I=3, 5)
WRITE (3, 2410) NNAM
2410 FORMAT (5X, I2)

WRITE (3, 2413) CHISQR
2413 FORMAT (1X, G12.5)
DO 2418 J=1, NTERMS
SIGMAA (J) = DSQRT (SNGL (ARRAY (J, J)) / ALPHA (J, J))
WRITE (7, 2243) J, A (J), SIGMAA (J)
IF (J.EQ.3) WRITE (8, 2419) A (J), SIGMAA (J)
2418 CONTINUE
2419 FORMAT (1X, G12.5, 1X, G12.5)
2420 FORMAT (3A2)
2423 FORMAT (5X, ' A (', I2, ') = ', G12.5, ' +- ', G12.5)
IF (ITEST.NE.1) GO TO 2176
READ (*, *)
2424 WRITE (6, 2425)
2425 FORMAT (1X, 'NEW X-SHIFT & Y SCALING FACTOR')
READ (5, *) SCALE, YSC
CALL GRAPHICSMODE ()
CALL DRAWLINES ()
CALL SPECTRUM (Y, YFIT, NST, NTOP, SPTEST, SCALE, YSC)
CALL ENDPROGRAM ()
WRITE (6, 2432)
2432 FORMAT (1X, 'CHANGE X & Y SCALE ? 1=Y, 0=N')
READ (5, *) SFLAG
IF (SFLAG.EQ.1) GO TO 2424
GO TO 2176

2437 WRITE (6, 2438)
2438 FORMAT (1X, '<=0 DEGREES OF FREEDOM', /)
GO TO 2443
2440 WRITE (6, 2442) KNAM
WRITE (7, 2442) KNAM
2442 FORMAT (1X, 'CANNOT FIND', 8A2)
2443 RETURN
END

```

C

C Subroutine to analyse Cd peak in Cd XRF analysis

C

C A(1) is the amplitude of the Cd alpha max peak

C A(2) is the amplitude of the Ag alpha max peak  
 C A(3) is the amplitude of the In alpha max peak  
 C A(4) is the amplitude of the Cd beta max peak  
 C A(5) is the Cd alpha max peak position  
 C A(6) are the exponential background  
 C A(7) are the exponential background  
 C A(8) are the exponential background  
 C A(9) are the exponential background  
 C 5.898296 is the alpha max peak width

REAL FUNCTION FNA(X,A,G)  
 DIMENSION A(9)

Z1=(X-A(5))/5.898296  
 Z2=(X-(A(5)-4.03191))/5.898296  
 Z4=(X-(A(5)-21.5038))/5.898296  
 Z5=(X-(A(5)-25.1766))/5.898296  
 Z6=(X-(A(5)+22.04468))/5.898296  
 Z7=(X-(A(5)+17.62553))/5.898296  
 Z8=(X-(A(5)+37.37021))/5.898296  
 Z9=(X-(A(5)+48.64681))/5.898296  
 Z10=(X-(A(5)+62.15745))/5.898296  
 Z14=(X-(A(5)+61.41277))/5.898296  
 Z11=(X-(A(5)+73.8383))/5.898296  
 Z12=(X-(A(5)+87.15745))/5.898296  
 Z13=(X-(A(5)+99.71064))/5.898296  
 ZZ1=0.0  
 ZZ2=0.0  
 ZZ4=0.0  
 ZZ5=0.0  
 ZZ6=0.0  
 ZZ7=0.0  
 ZZ8=0.0  
 ZZ9=0.0  
 ZZ10=0.0  
 ZZ11=0.0  
 ZZ12=0.0  
 ZZ13=0.0  
 ZZ14=0.0  
 IF (ABS(Z1) .LT. 5.) ZZ1=EXP(-Z1\*Z1)  
 IF (ABS(Z2) .LT. 5.) ZZ2=EXP(-Z2\*Z2)  
 IF (ABS(Z4) .LT. 5.) ZZ4=EXP(-Z4\*Z4)  
 IF (ABS(Z5) .LT. 5.) ZZ5=EXP(-Z5\*Z5)  
 IF (ABS(Z6) .LT. 5.) ZZ6=EXP(-Z6\*Z6)  
 IF (ABS(Z7) .LT. 5.) ZZ7=EXP(-Z7\*Z7)  
 IF (ABS(Z8) .LT. 5.) ZZ8=EXP(-Z8\*Z8)  
 IF (ABS(Z9) .LT. 5.) ZZ9=EXP(-Z9\*Z9)  
 IF (ABS(Z10) .LT. 5.) ZZ10=EXP(-Z10\*Z10)  
 IF (ABS(Z11) .LT. 5.) ZZ11=EXP(-Z11\*Z11)  
 IF (ABS(Z12) .LT. 5.) ZZ12=EXP(-Z12\*Z12)  
 IF (ABS(Z13) .LT. 5.) ZZ13=EXP(-Z13\*Z13)  
 IF (ABS(Z14) .LT. 5.) ZZ14=EXP(-Z14\*Z14)

```

FNA= A(1)*ZZ1 + .532*A(1)*ZZ2 + A(2)*ZZ4 + .53*A(2)*ZZ5
@ +A(3)*ZZ6+.533*A(3)*ZZ7+.21111*A(2)*ZZ8+.1831502*.21111*A(2)*ZZ9
@+A(4)*ZZ10+.2575*A(4)*ZZ11+.51865*A(4)*ZZ14+(0.325760)*A(3)*ZZ12
@+.1942446*(0.325760)*A(3)*ZZ13+A(6)*exp(A(7)*X)+A(8)*exp(A(9)*X)

C      FNA= A(1)*ZZ1 + .532*A(1)*ZZ2 + A(2)*ZZ4 + .53*A(2)*ZZ5
C      @ +A(3)*ZZ6+.533*A(3)*ZZ7+.21111*A(2)*ZZ8+.1831502*.21111*A(2)*ZZ9
C      @ +A(4)*ZZ10+.2575*A(4)*ZZ11+.51865*A(4)*ZZ14+A(5)*ZZ12
C      @ +.1942446*A(5)*ZZ13+ A(6)*exp(A(7)*X)+A(8)*exp(A(9)*X)

```

RETURN

END

SUBROUTINE FDA(X,A,DERIV,G)  
DIMENSION A(9),DERIV(9)

```

Z1=(X-A(5))/5.898296
Z2=(X-(A(5)-4.03191))/5.898296
Z4=(X-(A(5)-21.5038))/5.898296
Z5=(X-(A(5)-25.1766))/5.898296
Z6=(X-(A(5)+22.04468))/5.898296
Z7=(X-(A(5)+17.62553))/5.898296
Z8=(X-(A(5)+37.37021))/5.898296
Z9=(X-(A(5)+48.64681))/5.898296
Z10=(X-(A(5)+62.15745))/5.898296
Z14=(X-(A(5)+61.41277))/5.898296
Z11=(X-(A(5)+73.8383))/5.898296
Z12=(X-(A(5)+87.15745))/5.898296
Z13=(X-(A(5)+99.71064))/5.898296
ZZ1=0.0
ZZ2=0.0
ZZ4=0.0
ZZ5=0.0
ZZ6=0.0
ZZ7=0.0
ZZ8=0.0
ZZ9=0.0
ZZ10=0.0
ZZ11=0.0
ZZ12=0.0
ZZ13=0.0
ZZ14=0.0
IF (ABS(Z1).LT.5.) ZZ1=EXP(-Z1*Z1)
IF (ABS(Z2).LT.5.) ZZ2=EXP(-Z2*Z2)
IF (ABS(Z4).LT.5.) ZZ4=EXP(-Z4*Z4)
IF (ABS(Z5).LT.5.) ZZ5=EXP(-Z5*Z5)
IF (ABS(Z6).LT.5.) ZZ6=EXP(-Z6*Z6)
IF (ABS(Z7).LT.5.) ZZ7=EXP(-Z7*Z7)
IF (ABS(Z8).LT.5.) ZZ8=EXP(-Z8*Z8)
IF (ABS(Z9).LT.5.) ZZ9=EXP(-Z9*Z9)
IF (ABS(Z10).LT.5.) ZZ10=EXP(-Z10*Z10)

```

```

IF (ABS (Z11) .LT. 5.) ZZ11=EXP (-Z11*Z11)
IF (ABS (Z12) .LT. 5.) ZZ12=EXP (-Z12*Z12)
IF (ABS (Z13) .LT. 5.) ZZ13=EXP (-Z13*Z13)
IF (ABS (Z14) .LT. 5.) ZZ14=EXP (-Z14*Z14)

```

```

DERIV (1) = ZZ1 + .532*ZZ1

```

```

DERIV (2) = ZZ4 + .53*ZZ5+.21111*(ZZ8 + .1831502*ZZ9)

```

```

DERIV (3) = ZZ6 + .533*ZZ7+ (0.325760)*(ZZ12+ .1942446*ZZ13)

```

```

DERIV (4) = ZZ10+ .2575*ZZ11+.51865*ZZ14

```

```

DERIV (5) = 2/5.898296*(A (1) *ZZ1*Z1 + .532*A (1) *ZZ2*Z2+A (2) *ZZ4*Z4
@+.53*A (2) *ZZ5*Z5+A (3) *ZZ6*Z6+.533*A (3) *ZZ7*Z7+.21111*A (2) *ZZ8*Z8
@+.1831502*.21111*A (2) *ZZ9*Z9+A (4) *ZZ10*Z10+.2575*A (4) *ZZ11*Z11
@ +.51865*A (4) *ZZ14*Z14 + (0.325760)*A (3) *ZZ12*Z12
@ + .1942446*(0.325760)*A (3) *ZZ13*Z13)

```

```

DERIV (6) = exp (A (7) *X)

```

```

DERIV (7) = A (6) *X*exp (A (7) *X)

```

```

DERIV (8) = exp (A (9) *X)

```

```

DERIV (9) = A (8) *X*exp (A (9) *X)

```

```

RETURN
END

```